博士論文

Functionalized nanoparticles for sensing and separation of biomolecules

（機能性ナノ粒子の生体分子検出・分離への応用）

卜　同

Bu Tong

Table of contents

List of figures and tables

Chapter 1 General introduction

1.1 NANOPARTICLES AND SURFACE FUNCTIONALIZATION

1.1.1 Nanoparticles

Nanoparticle (NP) refers to ultrafine particle with a dimension ranging from 1 to 100 nm (Murthy, 2007). Despite being used for centuries in crafts such as stained glass, NPs are attracting more and more attention since 1990s when the term "nanoparticle" came into use. The number of different NP currently being studied is already beyond counting, that includes NPs synthesized from metals, noble metals, oxides, and semiconductors, along with many other non-traditional NPs like carbon allotropes, polymeric NPs, chemical NPs, and other assorted mateirals (Sapsford et al., 2013), Nanoparticles combine the properties of solids (for example, fluorescence in the case of quantum dots) with the ability to move (a property of molecules) (Stark, 2011). The small size of NPs, which is of the same order as the wavelength of the electron wave function, results in quantum confinement effects and consequently in the tunable optical and electronic properties by changing the size, shape, surface chemistry, or aggregation state. Furthermore, the small size of NPs creates large surface that can interact with outer environment. These special physical properties of NPs opens up numerous research directions for medicine and life sciences, including the use of NPs in drug delivery, cell imaging, and the NP-assisted gene therapy.

However, while some of the nanomaterial-based technologies have been developed in the last few decades; many nanotechnologies are still under experimental stage due to various drawbacks such as low detection sensitivity, lack of specificity, *et al*. Also, the impact of nanomaterials on the environment and on public health has received considerable concern in recent years.

1.1.2 Surface modification of NP for bio-applications

Applications of nanomaterials in biological field represent researches at the intersection of biology and nanomaterials. In most cases, surface of nanoparticles are functionalized with biomolecules that include proteins, peptides, nucleic acids (i.e., DNA/RNA/PNA/LNA as genes, oligomers, aptamers and ribozymes/DNAzymes), lipid, fatty acids, etc. The functionalization with these biological molecules offers binding, catalytic or therapeutic activities for NPs. The choice of NP surface functionalization strategy is dictated by a combination of factors including NP size, shape, surface chemistry, and structures, the nature of NP surface ligands and the utility desired in the final application (Sapsford et al., 2013).

Direct conjugation of a biomolecule to NP surface is usually driven by dative bonds. Au-thiol chemisorption is one of the most commonly used dative bonds, where the sulfur atom of a thiol contribute a lone pair of electrons to the empty orbitals of gold atoms at the interface, and this has formed the predominant basis of AuNP bioconjugation with thiolated proteins, peptides, and DNA (M.-C. Daniel & D. Astruc, 2004).

Non-covalent attachment of biomolecule to NP surface includes various types of interactions such as electrostatic attachment, hydrophilic interaction; *et al*. Electrostatic immobilization of biomolecules is very simple but widely used in NP bioconjugation approach, where oppositely charged species attract to each other. It was reported that the electrostatic effect are amplified, and factors such as ionic strength, the concentration of reagents, and the type and magnitude of charge are also in biomolecule immobilization (Khopade & Caruso, 2002; Schneider & Decher, 2004; Schoeler, Poptoshev, & Caruso, 2003; Zhao, Qian, An, & Du, 2009).

In other cases, alternatively, NPs surface might be modified with chemicals for surface coating/insulating or scaffolding. For example, some NPs have cores that are sensitive to outer environment, so that a surface coating is needed to protect the core to oxygen or humidity (Grass, Albrecht, Krumeich, & Stark, 2007). Sometimes, the synthesized NPs, semiconductor and carbon NPs are hydrophobic, so that chemical modification of their surface is needed to make them hydrophilic and biocompatible (Storm, Belliot, Daemen, & Lasic, 1995).

1.2 BIO-APPLICATION OF REPRESENTATIVE NPS

1.2.1 Application of AuNPs

Among various metal particles, AuNPs have attracted attention due to their advantageous properties involving stability, activity, conductivity, and surface chemistry. (Boisselier & Astruc, 2009; M. C. Daniel & D. Astruc, 2004; Dreaden, Alkilany, Huang, Murphy, & El-Sayed, 2012; Saha, Agasti, Kim, Li, & Rotello, 2012) In particular, assemblies of AuNPs provide optical and electrical properties that are distinct from individual particles. For example, aggregation of AuNPs accompanied by the surface plasmon shift can be recognized by a clear color change from red to purple, which enables potential applications in sensors for DNA, heavy metal ions and proteins. (M. C. Daniel & D. Astruc, 2004; S. Liu & Tang, 2009; Mirkin, Letsinger, Mucic, & Storhoff, 1996; Saha et al., 2012). Except for spherical AuNPs, various shapes of AuNPs such as plates, nanoshell structures, and star structures, were also prepared and demonstrate interesting optical properties (Hao, Nehl, Hafner, & Nordlander, 2007; Xia, Xiong, Lim, & Skrabalak, 2009).

The AuNP surface can be modified with seemingly limitless chemical functional groups like citrate, amine, oligonucleotides, peptide, antibodies, and so on. There are now many examples of highly sensitive and selective assays based upon gold conjugates. In recent years, attentions have been focused on therapeutic possibilities for these materials, such as in bio-detection and bio-diagnostics, imaging, drug delivery, and photoresponsive therapeutics (Giljohann et al., 2010).

Mirkin's group is pioneer in application of AuNP conjugates for diagnostics (Kim et al., 2010; J.-S. Lee, Ulmann, Han, & Mirkin, 2008; Lytton-Jean, Han, & Mirkin, 2007; Zheng, Daniel, & Mirkin, 2008). In a paper published in 1997, Mirkin and his colleagues reported a highly selective, colorimetric polynucleotide detection method based on mercaptoalkyloligonucleotide-modified AuNP probes. Addition of single-strand target oligonucleotide (30 bases) into a solution containing the appropriate probes resulted in the formation of a polymeric network of nanoparticles with a concomitant red-to-pink/purple color change. The unoptimized oligonucleotide detection system reached sensitivity as low as 10 femtomoles (Elghanian, Storhoff, Mucic, Letsinger, & Mirkin, 1997).

This method has been extended in a number of different directions. Jiang and colleagues have summarized recent advances in the development of AuNP-based colorimetric and fluorescent assays for ion including cations (such as Hg^{2+}, Cu^{2+}, As^{3+}, Ca^{2+}, Al^{3+}, *etc.*) and anions (such as NO_2^-, CN^-, PF_6^-, F^-, I^-, oxoanions), and small organic molecules (such as cysteine, homocysteine, trinitrotoluene, melamine and cocaine, ATP, glucose, dopamine and so forth) (D. Liu, Wang, & Jiang, 2011).

The high atomic number and electron density of Au leads to efficient absorption of X-ray irradiation, superior to conventional iodin-based contrast agents currently used in the clinic at higher X-ray tube voltages, such as 120 and 140 KV (Mieszawska,

Mulder, Fayad, & Cormode, 2013). Other advantages of AuNPs for imaging includes, long circulation times, targeting to specific cell types or other ligands and cell tracking (Arifin et al., 2011; Q.-Y. Cai et al., 2007; Cormode et al., 2008). These properties have resulted in the expoloration of AuNPs as contrast agents for X-ray based imaging techniques (Mieszawska et al., 2013).

Ashkenazi and colleagues are one of the earliest groups to apply AuNPs in bio-imaging. In a paper published in 2007, they developed a targeted AuNP as a contrast agent for high contrast photo-acoustic imaging. By changing the aspect ratio of the elongated "rod" shape of the AuNP, its plasmon peak absorption wavelength can be tuned to the near IR (700-900 nm) for an increased penetration depth into biological tissue (Agarwal et al., 2007). Emelianov and his group used AuNP as tracer to improve the efficacy of ultrasound-guided photo-acoustic imaging for monitor mesenchymal stem cells. This technique is capable of quantitative, longitudinal assessment of stem cell behaviors with high spatial resolution and sufficient penetration depth (Nam, Ricles, Suggs, & Emelianov, 2012).

AuNPs absorb light photon efficiently and converse it into thermal energy quickly. This enables the application of AuNPs in the photothermal therapies, especially for cancer applications. The irradiation of AuNPs with light of the correct wavelength induces localized temperature increases, which leads to the photothermal ablation of cells in the vicinity, as such temperature increases cause biomolecule denaturation and cell damages (Guo et al., 2010; Huang, El-Sayed, Qian, & El-Sayed, 2006; Kirui, Krishnan, Strickland, & Batt, 2011; Loo, Lowery, Halas, West, & Drezek, 2005).

Other therapeutic applications are as drug or gene delivery vehicles and in the case of AuNPs formed from Au-198, as radio therapeutics (Ramos, Huang, & Rege, 2013) are also in rapid progress.

1.2.2 Application of magnetic NPs

Besides all other interesting properties of NPs, magnetic NPs can be manipulated by an external magnetic field gradient according to Coulomb's law. This "action at a distance", combined with the intrinsic penetrability of magnetic fields into human tissue, opens up many applications involving the transport and/or immobilization of magnetic NPs (Q. A. Pankhurst, Connolly, Jones, & Dobson, 2003). In recent years, magnetic nanoparticles have played an increasing role in biomedical applications and have been the subject of extensive research investigations. Physical properties, including nanoparticle size, composition, and surface chemistry, vary widely and influence their biological and pharmacological properties and, ultimately, their clinical applications (Bárcena, Sra, & Gao, 2009).

The use of magnetic NPs for gene therapy was first demonstrated in last decade (Mah et al., 2002). Generally, NPs that carry the therapeutic genes are injected intravenously and strong, high-gradient external magnets are used to capture the particles as they flow through the blood-circulation. NPs target the tissue by application of magnetic field. Once located at the target tissue, therapeutic genes can be released by either via enzymatic cleavage of the cross-linking molecules, charge interactions, or degradation of the polymer matrix (Dobson, 2006). It was reported that the transfection efficiency has been improved by using magnetic NPs. Cai *et al*. have used carbon nanotubes to deliver genes. The so called nanotube spearing is nickel-embedded, magnetic nanotubes to which DNA is attached. In this study, the gene transfection ratio reached more than 90% (D. Cai et al., 2005).

Magnetic NPs have potential also in the delivery of drugs to targeting tumors. Many traditional anti-cancer agents are not able to penetrate into the hypoxic zones in tumor tissues. Magnetic NPs can be an ideal cargo for the delivery of drugs in these

hypoxic zones, where the movement of NPs can be controlled by an external magnetic field. Parihar and colleagues have reviewed the development of magnetic NP drug delivery system in details (Mody et al., 2014).

The use of magnetic NPs in human tissue imaging developed rapidly after the first paper reported by Gelich and colleagues in 2005 (Gleich & Weizenecker, 2005). The so-called magnetic particle imaging (MPI) takes advantages of the nonlinear magnetization curve of small magnetic particles to generate harmonic responses to time-varying fields that can be detected using standard lock-in methods to a high degree of precision, and with very little back ground signal to contend with (Q. Pankhurst, Thanh, Jones, & Dobson, 2009).

The application of strong, stable magnetic nanoparticles is also of particular interest in removing small concentrations of valuable compounds reliably from a liquid or living organism (Stark, 2011). The in vivo extraction of toxins or metabolite allows ultimately selective removal of a noxious or damaging component out of a tissue, which opened up novel concept for disease treatments (Herrmann et al., 2010; Q. Pankhurst et al., 2009).

Substantial progress in the size and shape control of magnetic NPs has been made by developing methods such as co-precipitation, thermal decomposition and/or reduction, micelle synthesis, and hydrothermal synthesis (A. H. Lu, E. e. L. Salabas, & F. Schüth, 2007a). The availability of stable magnetic NPs allows their new applications (Stark, 2011). For example, magnetic chelating agents have been suggested to enable removal of toxic metal ions directly from water or blood streams (Koehler et al., 2009). A major challenge still is protection against corrosion, and therefore suitable protection strategies should be emphasized in the future study (Lu et al., 2007a).

1.3 BRIEF INTRODUCTION OF EACH CHAPTER

In this dissertation, application-oriented study of functional NP was explored: microscopic method was employed to improve the sensitivity of gold nanoparticle (AuNP)-based DNA mutation detection; antibody-conjugated AuNPs was designed and synthesized for the detection of amyloid protein aggregation; and a ferromagnetic NP was used in the selective clearance of amyloid aggregates from monomers.

In the second chapter, dark field microscopy (DFM) was employed to visualize and quantify complementary DNA-induced gold nanoparticle aggregation at the single-particle level, with a detection limit of 100 fM DNA, which allows the highly sensitive detection of single nucleotide polymorphisms (SNPs). Results suggested that the aggregation process is consistent with the cluster–cluster model

In the third chapter, amyloid beta (Aβ) specific antibodies were immobilized on AuNPs and DFM was employed to visualize and quantify Aβ aggregates -induced AuNP aggregation at the single-particle level, with a detection limit to pM level of Aβ protein. This allows the fast and highly sensitive detection of Aβ aggregates in solution.

In the fourth chapter, selective recognition and separation of Aβ aggregates (i.e. oligomers and fibrils) from Aβ monomer using ferromagnetic nanoparticle poly[3-(methacryloyl amino)propyl] trimethylammonium chloride (PolyMAPTAC) Co/C (MC-NP) was reported. MC-NP is able to target Aβ oligomer and fibrils, followed by separation from monomers in solution by application of a magnet. The adsorption was characterized by dot blot and western blot assay. TEM was employed to confirm the adsorption directly. This study implies potential applications of MC-NPs in diagnosis and treatment of various brain diseases such as Alzheimer's disease.

FIGURES IN CHAPTER 1

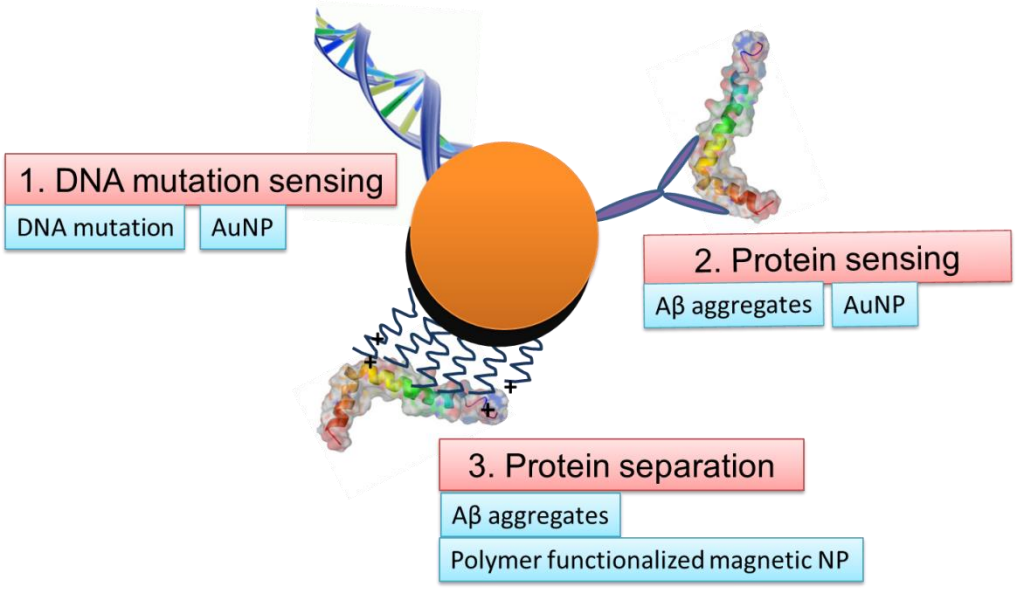

Fig 1.1 Overview of chapters in the dissertation

1) Detection of target DNA induced AuNP aggregation using DFM, 2) detection of Aβ protein assembly using DFM, and 3) separation of Aβ aggregates using magnetic nanoparticles.

Chapter 2 Detection of DNA induced gold nanoparticle aggregation with dark field imaging

2.1 SUMMARY

Several methods have been used for the detection of AuNPs aggregation, such as color change, UV-Vis spectra and dynamic light scattering (DLS). However, changes in color and UV-Vis spectra can only be detected when there is significant aggregation growth, resulting in low sensitivity. The inhomogeneity of size and shape of AuNPs aggregates influences the quality of the DLS result. Therefore, it is necessary to develop simple and direct detection methods for the analysis of AuNPs aggregation. In this chapter, single molecule approach using dark field microscopy (DFM) was applied to examine AuNPs aggregation, because DFM monitors scattering light that is extraordinarily efficient to size change of AuNPs. This method reached a detection limit of 100 fM DNA, which allows the highly sensitive detection of SNPs (Fig 2.1).

2.2 BACKGROUND AND INTRODUCTION

2.2.1 AuNP and its applications in bio-diagnosis

AuNPs have been successfully employed as a colorimetric probe for both chemical and biological detection, based on their size-dependent surface plasmon resonance (SPR) absorption(Rosi & Mirkin, 2005). Wang and coworkers reported an elegant approach for colorimetric detection of aptamers. Based on the observation that AuNPs preferably bind to single stranded (ss-)DNA rather than to double strand (ds-)DNA, they designed a aptamer-target binding readout (ATBR) strategy that translates an aptamer-target binding event to a duplex-to-aptamer dehybridization process, which can

be conveniently detected with unmodified AuNPs in a colorimetric approach with a detection limit of ~ 2 μM ATP (Wang et al., 2007).

2.2.2 Detection of AuNPs aggregation

Several methods have been used for the detection of AuNP aggregation, such as color change, UV-Vis spectroscopy and DLS. The aggregation of AuNPs results in dramatic changes in their absorption and scattering spectra because of strong plasmonic coupling and interference of scattered fields (N. Khlebtsov, Dykman, Krasnov, & Mel'nikov, 2000; Storhoff et al., 2000). When the inter particle separation approaches 0.1 of their diameter, the coupled plasmon band becomes significantly broadened and shifted from the single particle green resonance (~520 nm) to the red or near infrared (NIR) (B. Khlebtsov, Zharov, Melnikov, Tuchin, & Khlebtsov, 2006), leading to change in solution color from red to purple blue or gray.

Colorimetric methods, in particular, are extremely attractive because they can be easily read out with the naked eye, in some cases at the point of use. DNA-Au NPs have high extinction coefficients (3-5 orders of magnitude higher than those of organic dye molecules) (Yguerabide & Yguerabide, 1998) and unique distance-dependent optical properties that can be chemically programmed through the use of specific DNA interconnects, which allows one to detect targets of interest through colorimetric means (Elghanian et al., 1997; Kanayama, Takarada, & Maeda, 2011; Mirkin et al., 1996). Mirkin and his colleagues have present a highly selective and sensitive colorimetric detection method for Hg^{2+} that relies on thymidine-Hg^{2+}-thymidine coordination chemistry (Zubay & Doty, 1958) and complementary DNA-AuNPs with deliberately designed T-T mismatches (Fig 2.2) (J. S. Lee, Han, & Mirkin, 2007).

DLS is an analytical tool used routinely for measuring the hydrodynamic size of nanoparticles and colloids in a liquid environment (Berne & Pecora, 2000). AuNPs are extraordinary light scatters at or near their surface plasmon resonance wavelength (Yguerabide & Yguerabide, 1998). Jans and colleagues have demonstrated that DLS can be used as a very convenient and powerful tool for AuNPs bio-conjugation and bio-molecular binding studies. The specific interactions between protein A-conjugated AuNP and a target protein, human IgG, can be monitored *in situ* by measuring the averaged particle size change in solution (Jans, Liu, Austin, Maes, & Huo, 2009).

2.2.3 SNPs and its detection methods

Single nucleotide polymorphisms (SNPs) most commonly refer to single-base differences in DNA among individuals, which is by far the most prevalent of all DNA sequence variation (Kwok, 2003). Public efforts have so far identified over two million common human SNPs (Sachidanandam et al., 2001). SNPs are the markers of choice in complex disease mapping. Besides the obvious applications in human disease studies, SNPs are also extremely useful in genetic studies of all organisms, from model organisms to commercially important plants and animals (El-Omar et al., 2000).

The most reliable method for detection of SNPs is direct sequencing. Classic method like denaturing high performance liquid chromatography (dHPLC) is a fast and reliable technique for the DNA variation screening (Jones et al., 1999; Xiao & Oefner, 2001). It can detect in minutes with almost 100% sensitivity and specificity (Spiegelman, Mindrinos, & Oefner, 2000). However, these approach suffers from high cost and low throughput (Sato, Onoguchi, Sato, Hosokawa, & Maeda, 2006).

A variety of assay techniques that combined the allele-specific hybridization and fluorometric detection have been developed. Tyagi and coworkers have developed novel nucleic acid probes that recognize and report the presence of specific nuclei acids in homogeneous solutions. These probes undergo a spontaneous fluorogenic conformational change when hybridizing to targets. Only perfectly complementary targets induce this conformational change while hybridization does not occur when the target contains SNPs (Tyagi & Kramer, 1996).

A promising approach towards high-throughput genotyping of SNPs is to use arrays of immobilized oligonucleotides in miniaturized assays (Hacia, 1999) (Schena, Shalon, Davis, & Brown, 1995). Pastinen and coworkers have developed a microarray system based on mini sequencing single nucleotide primer extension that allows highly specific multiplex genotyping of SNPs (Pastinen, Kurg, Metspalu, Peltonen, & Syvänen, 1997). In the mini sequencing reaction a DNA-polymerase is used to extend detection primers that anneal immediately adjacent to the sites of SNPs with labeled nucleotide analogues that are complementary to the nucleotide at the SNP sites (Syvänen, Aalto-Setälä, Harju, Kontula, & Söderlund, 1990).

These techniques usually require bulky and expensive instruments for the fluorometric detection (Sato et al., 2006). To make good use of SNPs for finding genes related to disease and studying their function, better and cheaper technological methods are needed for discovering SNPs.

2.2.4 DNA induced non-cross-linking AuNP aggregation

Sato and coworkers reported aggregation phenomenon of DNA-functionalized AuNPs induced by hybridization of target DNA which does not cross-link the particles

(Sato, Hosokawa, & Maeda, 2003). In general, a probe DNA was immobilized on the surface of AuNPs with diameters of 5- 20 nm. In the presence of high salt concentration (1 M NaCl), with addition of DNA sample that is complementary to the probe DNA, aggregation of AuNP can be seen directly by naked-eyes. The color change from red to blue is the result of absorption peak shift toward to longer wavelength. (Bohren & Huffman, 1983). However, the mismatched DNA at the free end stabilize dramatically the AuNP dispersion, as long as the mismatched point is within 1 nm (around 3 nucleotide acids) from the free ending (Fig 2.3) (Kanayama, Takarada, Fujita, & Maeda, 2013; Kanayama et al., 2011).

The mechanism of the phenomena is not yet clear. It is possible that in this system the AuNP assembly is promoted by the reduction of the repulsive interactions between nanoparticles upon formation of duplex DNA on the surface of the nanoparticles. Specifically, the stiffening of the DNA upon formation of duplex raises the binding constant with counter ions, which can serve to better shield the negative charges as discussed below in 2.2.5.

This non-cross-linking (NCL) AuNP aggregation phenomena have been applied to the detection of SNPs in genomic DNA (Sato, Hosokawa, & Maeda, 2005). By optimizing the AuNP size and reaction time, a relatively low detection limit was achieved. It was found that larger AuNP (up to 40 nm) enables lower detection limits in NCL method. Detection limit of 1-2 nM can be achieved after 24 h's incubation.

The NCL aggregation of dsDNA-AuNP was also applied for detection of mercury ions by naked eye without any apparatus by choosing effective probe DNA. Kanayama and coworkers found that the position of a T-T mismatch embedded in the dsDNA layer was crucial for the detection. This easy detection can be finished within 1 min with a detection limit of 0.5 μM (Kanayama et al., 2011).

2.2.5 Mechanism of DNA induced NCL AuNP aggregation

To explain the mechanism of complementary ssDNA induced NCL AuNPs aggregation, the interfacial interaction between DNA-based soft interface and the outer liquid environment has to be considered. On the interface of solid/liquid, soft interface was formed by the ordered polymer and liquid medium with solutes. And the interaction between solid/liquid interfaces might be affected by various factors including hydrophobic effect, entropy effect, osmotic pressure as well as Coulomb force.

Up to now, there are several reports investigating in this mechanism though not a clear conclusion has been achieved. In our experiment, the DNA chain is short (15- 50 nucleotides) to be soft when it is single-strand, while it becomes a hard stick-like configuration in double helix model with a diameter of 2 nm (Kanayama & Maeda, 2014).

Effect of electrostatic force: Due to the negative charged sugar-phosphate backbone of nucleotide, the DNA carries negative charge on the interface. However, the salt concentration in the buffer is so high (1 M) that the surface charges are screened by high salt concentration. As a result the electrostatic force is not the possible force to drive the AuNP aggregation

Stacking interaction: or pi stacking (π-π stacking) refers to attractive, non-covalent interactions between two aromatic rings. Alignment of positive electrostatic potential on one ring with negative electrostatic potential on another ring forms an offset stack. As introduced ahead, the double helix DNA on AuNP surface that is hard stick like structure with one end immobilized on AuNP and the other end free in medium. The

existence of pi stacking between the nucleic bases at the free end of DNA double helix is possible that causes AuNP aggregation.

Van der Waals interaction: To understand the NCL aggregation, Fujita and coworkers performed a structural study on DNA-functionalized AuNP and its NCL aggregation using synchrotron radiation small-angle X-ray scattering (Fujita et al., 2012). They studied AuNP with different sizes (15 nm and 40 nm) with various DNA lengths (15-45 bp) immobilized on. The result showed that the surface distance between the AuNPs increased with increasing length of DNA duplex, although the increment of the distance per base pair was not constant and suggested the tendency to become small with increasing DNA length, meaning the inter-digitation of DNA layers. Furthermore, it was found that the relative increase DNA length to core size leads to the increase in colloidal stability. At last Fujita and coworkers concluded that van der Waals interaction between core particles between DNA duplexes is the dominant attractive interaction. The steric repulsion force arising from entropic loss of thermal fluctuation of DNA molecules might be a key factor to characterize the NCL aggregation.

If the aggregation is due to end-to-end stacking effect, debated in Fujita's paper, the distance between two nanoparticles should be twice as long as DNA length. However, Fujita's result showed that the distance between two AuNPs is slightly shorter that twice of DNA length. On the other hand, Kanayama pointed out that in certain condition, factors like the direction of DNA on AuNP surface can affect the detected DNA length and distance between AuNPs so that it is still too early to deny the end-to-end stacking interaction (Kanayama & Maeda, 2014).

Breathing effect: If seen in the micro view point, the stick-like double helix DNA on AuNP surface is not rigid but making micro Brownian motion and interacting with water molecules, followed by the open/closing of nucleotides at the end (breathing).

It is easier for water molecules to break into the mismatched DNA at the end rather than the fully complementary DNA double helix. In another word, the mismatched nucleotides generated entropic repulsion by the terminal 'breathing' (Kanayama & Maeda, 2014).

Kanayama and coworkers have proved that stability of AuNPs aggregates decreased dramatically if the breathing like effect of based pairs near the free end were inhibited. And the stability of DNA immobilized AuNP dispersion can be affected by mismatched DNA as long as the mismatched point is within 1 nm (around 3 nucleotide acids) from the free ending (Kanayama et al., 2013; Kanayama et al., 2011). This suggested the importance of 'breathing' effect in stabilizing AuNP colloid.

2.2.6 Dark field imaging

As described in 2.2.2, several conventional methods such as color change, UV-Vis spectroscopy and DLS have been used for the detection of AuNPs aggregation. However, changes in color and UV-Vis spectroscopy can only be detected when there is significant aggregation growth, resulting in low sensitivity. The inhomogeneity of size and shape of AuNPs aggregates influences the quality of the DLS result. Therefore, it is necessary to develop simple and direct detection methods for the analysis of AuNPs aggregation.

Optical studies of single metal particles have a long history in physical science dating back to Zsigmondy's work at the turn of the previous century. Zsigmondy and coworkers developed a dark-field immersion microscope that allowed them to observe and count single metal particles in a liquid (Fig 2. 4) (Hu et al., 2008; Zsigmondy, 1925).

It is known that AuNP suspensions scatter colored light when illuminated by a beam of white light and that the color depends on particle size (Bohren & Huffman,

2008). Yguerabide and coworkers have observed that light-scattering AuNP suspensions have the same appearance as fluorescent solutions: a 40-nm-diameter gold suspension, for example, produces a green emission under white light illumination. Moreover, it was reported that emission from a 40-nm AuNP suspensions down to particle concentrations of 10^{-14} M can be readily detect by eye using a very simple and low-cost illumination system (Yguerabide & Yguerabide, 1998). Jans and coworkers also explored the application of DFM in detecting AuNP clusters that were induced by increasing amount of NaCl concentration in the colloid. The DFM images confirmed that upon an increase in NaCl concentration, the particles tend to cluster in groups (Jans et al., 2009).

Also, it was found that the light scattering properties of gold, silver and other particles are not significantly altered by coating them with proteins, DNA and other polymers (Yguerabide & Yguerabide, 1998). Scattered light intensities of spots in the DFM images /videos can be quantified with a photodiode or photomultiplier tube and particle images can be recorded with a standard (not ultrasensitive) black and white or color CCD video camera. These observations have suggested that light-scattering property of AuNP can be used in tracer experiments or assays to achieve detection sensitivities and single particle detection in colloid.

2.3 MATERIALS AND METHODS

2.3.1 Materials

All the oligonucleotides were purchased from Operon Japan. The DNA sequences were shown as below. The concentration of each strand was estimated by measuring OD_{260}.

Probe DNA : HS-(C_6H_{12}) - 5'TACGCCACCAGCTCC 3'

Complementary DNA: 3'ATGCGGTGGTCGAGG 5'

Mismatched DNA : 3'ATGCGGTGGTCGAGT 5'

The gold colloid was purchased from British Biocell International. Concentration of 40 nm AuNPs was 9×10^{10} mL^{-1} (0.15 nM), with OD_{520}=1.0.

2.3.2 Functionalization of AuNPs with thiolated DNA

The functionalization follows the procedure described by Sato et al(Sato et al., 2005). Three nmol of probe DNA was incubated with 1 mL of the AuNP solution at 50℃ for 16 h. The solution was arranged to 0.1 M NaCl, 10 nM phosphate buffer (pH 7) by addition of corresponding salts. The colloid continued to be kept at 50℃ for 40 h. To remove unreacted probes, the solution was centrifuged at 15,000 rpm for 20 min, then the supernatant was replaced by 1 mL of the same buffer. After another centrifugation under the same condition described previously, the precipitate was redispersed into 0.3 mL of the same buffer to make a stock solution.

2.3.3 Estimation of the amount of the immobilized probe DNA

To release the immobilized probe DNA from AuNPs, 10 mM dithiothreitol (DTT) was added to the ssDNA-AuNP colloid. The solution was incubated at room temperature for 16 h. After centrifugation at 14,000 rpm for 25min, the concentration of released probe DNA in the supernatant was quantified using OliGreen ssDNA Quantitation Kit (Invitrogen).

2.3.4 DNA-induced AuNPs aggregation

Various concentrations (from 0 to 250 nM) of complementary ssDNA (target DNA) were added into the ssDNA-AuNP colloid (1.98×10^{10} mL^{-1} (=32 pM)) in the presence of 1 M NaCl, and incubated for 1 h at room temperature. Mismatched ssDNA (100 nM) was added as a negative control sample.

2.3.5 Dark field microscopy analysis

For the DFM analysis, 6 μL of the AuNPs samples were deposited onto glass slides (High Density Amine Coated Slides, Matsunami Glass Ind., Osaka, Japan) and covered with cover glass. DFM images were taken using BX53 microscope (Olympus, Tokyo, Japan) equipped with UDCW dark field condenser, UPlanFLN 60×objective lens (N.A. 0.65-1.25) and DP73 CCD camera (Olympus). AuNPs were identified as bright orange-colored spots in DFM images and the scattered light intensity of each spot was quantified.

Firstly, bared AuNP monomers with diameters of 20 nm, 40 nm, 60 nm and 100 nm were spotted onto amine coated slide glass. The DFM images were taken, and intensity histogram of scattered light was plotted.

For the DNA induced AuNP aggregation assay, the brighter spots that have intensities higher than 24 a.u. were defined as aggregates, since 95% of the dispersed negative control sample to which 100 nM of mismatched ssDNA was added showed an intensity lower than 24 a.u.. The ratio of aggregates at each target DNA concentration was estimated to calculate the LOD.

2.3.6 Calculation of limit of detection (LOD)

The LOD was evaluated by the 3σ criterion method, where σ denotes the standard deviation of zero-concentration background data (n=6). Average values from three histograms obtained by three different glass slides were shown in the figure. The data points of the calibration curve were fitted with a four-parameter logistic function (Arata, Komatsu, Hosokawa, & Maeda, 2012; Diamandis & Christopoulous, 1996):

$$y=d+(a-d)/[1+(x/c)^{b}],$$

where a, b, c and d are fitting parameters.

These parameters were optimized by nonlinear least-square regression weighted by the reciprocal of the square of standard deviation of each datum point. The LOD was calculated from the fitting equation as the concentration that gives higher value than 3σ line (=background (zero-concentration) + 3σ).

2.3.7 Determination of LOD by UV-Vis Spectrometer, DLS and color change

Conventional methods such as UV-Vis spectroscopy, DLS and color changes were used to estimate LOD for comparison. Cary 50 UV-Vis spectrometer (Varian, Palo Alto, USA) was employed to measure UV-Vis absorption spectrum. The ratio of absorbance values at 630 and 530 nm (A_{630}/A_{530}) at various concentrations of added target ssDNA was used for estimation of aggregation of the AuNPs solution. LOD was determined by the concentration of added ssDNA that gives higher A_{630}/A_{530} value than 3σ line. Sample with addition of 100 nM mismatched DNA was used as negative control. Average values from three different samples were shown (n=6 for zero-concentration).

The hydrodynamic diameters of the AuNPs under investigation were measured using a DLS system (Malvern, ZetasizerNano ZS90, Worcestershire, UK). A Zen 2112 cuvette was used as sample container. Malvern software (DTS ver. 5.10) was used to

analyze the data. The size of aggregates was obtained using a non-negative least squares (NNLS) analysis methods based on intensity average. LOD was determined by the concentration of added ssDNA that gives larger size of aggregates than 3σ line. Sample with the addition of 100 nM mismatched DNA was used as a negative control. The average values of three different samples were used (n=6 for zero-concentration). The photo-images of tubes were taken by a digital camera.

2.3.8 Time course assay

For time course-assay, 50 nM of complementary ssDNA was added to the 32 pM ssDNA-AuNP colloid in the presence of 1 M NaCl. At different incubation time (0 to 120 min), sizes of the aggregates were measured by DLS. Also, 10 μL of colloid solution was taken at each time-point and was deposited on glass slides for DFM imaging. The intensities of the each AuNP spot in the DFM image were determined, and the ratio of monomers (AuNP spots that have intensities less than 24) per all the spots at each time-point was estimated.

2.3.9 TEM assay of AuNP aggregation caused by addition of target DNA

Increasing amount of target DNA (from 0 to 5 nM) was added to ssDNA-AuNP colloid and incubated at room temperature for 1 h.

10 μL of nanoparticle solution was pipetted onto TEM grids and leaving for 1 min. The extra solution was absorbed by filter paper. TEM measurements were performed by JEOL-1230 instrument (JEOL Ltd., Tokyo, Japan).

The AuNPs on TEM images were classified into three types: monomer, oligomer and big aggregates, where oligomer was defined as AuNP aggregate that is made up of 2-

10 AuNPs. Number of AuNPs in all clusters was counted in each type to draw size distribution charts of AuNP aggregates.

2.4 RESULTS AND DISCUSSION

2.4.1 Immobilization of ssDNA on AuNP

With the addition of DTT, probe ssDNA immobilized on AuNP surface was released after incubation at room temperature for 16 h. By using Oligreen ssDNA quantitation Kit, the amount of released DNA was estimated and the amount of ssDNA on AuNPs was determined to be 580 ± 20 molecules per particle. This result is similar to the amount of ssDNA on each AuNP reported by previous papers (Sato et al., 2006). Sato and coworkers have reported that AuNP with size of 40 nm is more efficient in immobilizing probe DNA (15 bases) than that of 15 and 30 nm (166, 410 ssDNA per AuNP respectively.). While AuNP with size of 50 nm captures more DNA probes (1200 DNA per particle), the detection limit of added target DNA was worse than that using 40 nm AuNP. Thus, AuNP of 40 nm was chosen for the detection of complementary target DNA induced AuNP aggregation.

2.4.2 Target DNA-induced AuNP aggregation

To confirm the target ssDNA induced NCL AuNPs aggregation 500 nM complementary ssDNA was added to the ssDNA-AuNP colloid, while 500 nM mismatched ssDNA was added to ssDNA-AuNP colloid for negative control. The result turned out that the addition of complementary ssDNA induced the color change of AuNP colloid from red to blue with the absorption peak shift to longer wavelength (Fig 2. 6).

2.4.3 Size-dependent scattering intensity of AuNPs determined by DFM

Bared AuNPs of various diameters (20, 40, 100 nm) were spotted on amine functionalized glass. In the DFM images (Fig 2.7a), single AuNP on DFM image can be distinguished by naked eyes when the particle size is larger than 40 nm. With the size increases, more light were scattered from the AuNP surface, which were also shown in peak shift of the intensity histograms of 100 nm AuNP (Fig.2.7b).

Fig 2.8 showed two typical images of dispersed and aggregated AuNPs taken by DFM. The aggregated AuNP clusters showed bright yellowish color while the dispersed AuNPs are hardly visible by naked eyes, though the dispersed AuNPs can been seen after been enhanced using image software as shown in the inset images. The number of spots in images of aggregated AuNPs was smaller than that in the dispersed AuNPs images. The intensity histogram that derives from scattering light intensities was shown in Fig 2.8c. The aggregation of AuNP resulted in peak shift from left to right in the histogram, which means more light were scattered from bigger or aggregated AuNPs. This indicates the potential of DFM in detecting aggregation of AuNPs with high sensitivity.

2.4.4 Determination of the detection limit of target DNA using DFM

The size of AuNP aggregates was estimated by the intensity of each spots in DFM images. Fig 2.9 shows intensity histograms of dispersed and aggregated AuNPs induced by addition of various amount of target ssDNA, which indicate the size and number of each AuNP aggregates. As shown in the figure, larger aggregates were observed when an increased amount of DNA was added. The change in the intensity histograms was used to determine the detection limit of the target ssDNA and to investigate AuNP aggregation models.

To determine the detection limit of DFM, increasing concentrations of the target complementary ssDNA ranging from 0 to 250 nM were added to ssDNA-AuNP in the presence of 1 M NaCl. The spots on DFM images were used to obtain corresponding histograms. As shown in the Fig. 2.9, the addition of increasing concentrations of target ssDNA into the ssDNA-AuNP colloid resulted in particles with higher intensities. This indicates that the number of AuNPs per aggregates cluster increased following an increase of the added target ssDNA. Notably, small aggregates at low target ssDNA concentrations were detectable. It is worth noting that the peak of intensity histograms did not shift as much as that of size changes of bared AuNPs. The possible reason might be that being different from bared AuNPs dispersed in the colloid; there are spaces between particles in the AuNP aggregates that were induced by hybridization of DNA. The spaces reduce electron transportation efficiency between particles in clusters, then result in a reduction of sensitivity of scattered light intensity to AuNP aggregates size changes.

The detection limit of the target ssDNA concentration was estimated from the ratio of aggregates at each concentration as follow. The brighter spots that have intensities higher than 24 were defined as aggregates, since 95% of the dispersed negative control sample to which 100 nM of mismatched ssDNA was added showed an intensity lower than 24 a.u.. The ssDNA-AuNP sample without the target ssDNA showed a similar histogram to that with mismatched ssDNA. As shown in Fig 2.10, the ratio of aggregates increased at higher concentrations of the target ssDNA.

The LOD was evaluated by the 3σ criterion method as previously reported (Arata et al., 2012), where σ denotes the standard deviation of zero-concentration background data (n=6), and was determined to be as low as 100 fM (corresponding to 0.6 attomol in a 6 μL sample volume) by fitting using a four-parameter logistic function.

This result indicated that measurement of the scattering intensity from DFM imaging at the single-particle level enables visualization and quantification of AuNP aggregation with high sensitivity, and could be utilized in highly sensitive bio-analytical tools. DFM is suitable for observation of AuNPs since AuNPs exhibit light scattering at a visible light wavelength due to plasmon resonances (Jans et al., 2009) that are highly sensitive to nanoparticle size, shape and local environment (Jain, Lee, El-Sayed, & El-Sayed, 2006; Nehl et al., 2004).

2.4.5 Comparison of LOD of DFM with that of conventional methods: UV-Vis spectrometer, DLS and color change

The detection sensitivity of conventional methods such as UV-Vis spectroscopy, DLS and color changes strongly depends on various factors such as AuNP size (Sato et al., 2006), surface modification (Ma, Tian, Wang, & Wang, 2010; Pylaev et al., 2011), reaction time (Sato et al., 2006) and salt concentration (Sato et al., 2003). Thus, we compared the sensitivity of DFM with that of these conventional methods using the same conditions. Fig 2.11a shows the color of AuNP colloid solutions, Fig 2.11b & c, shows changes in the absorbance spectra, and Fig 2.12 shows the diameter obtained by DLS at different concentration of the added target ssDNA. The ratio of absorbance values at 630 and 530 nm (A_{630}/A_{530}) was used for estimation of aggregation in the AuNP colloid with a UV-Vis spectrophotometer as described (M. Sakono et al., 2010). An obvious change was observed when the added target ssDNA concentration was higher than 50 nM, whereas the addition of 100 nM of mismatched ssDNA (negative control) showed no significant difference in the A_{630}/A_{530} value compared to the dispersed AuNP colloid (Fig 2.11c). Similarly, the size of aggregated AuNPs measured by DLS increased after addition of more than 50 nM of target ssDNA, while the addition of 100 nM of

mismatched ssDNA did not cause any change in the size (Fig 2. 12). According to the 3σ criterion methods, the LODs of absorbance spectroscopy and DLS were estimated to be approximately 50 nM. The colors changed from red to blue when the concentration of the added target ssDNA was higher than 75 nM (Fig 2.11a). This is in agreement with a previous investigation conducted under similar conditions (Sato et al., 2006).

This sensitivity was 5 orders of magnitude lower than that of DFM. This might be explained as follow. When a small amount of target ssDNA is added, only a few AuNPs would form aggregates, and since UV-Vis spectroscopy and DLS were based on ensemble measurement, such a low amount of small aggregates would not be detected. In contrast, individual non-homogeneous AuNP aggregates can be observed by DFM, indicating that the DFM method has sensitivity greater than that of conventional methods.

2.4.6 Investigation of dsDNA-AuNP aggregation model

Taking advantage of DFM measurement, the dsDNA-AuNP aggregation model was investigated by studying the assembly dynamics using DFM. As stated above, the two NP aggregate growth models, namely, particle-cluster and cluster-cluster models (Fig 2.5), were proposed based on modelling of theoretical phenomena and computer simulations (Khan, Pierce, Sorensen, & Chakrabarti, 2009; Park, Lee, Georganopoulou, Mirkin, & Schatz, 2006). In cluster –cluster model, NPs of any size might combine and result in a larger aggregates, while only monomer could bind to other monomers or clusters in the particle-particle aggregation model. Although it was difficult to confirm the hypothesis experimentally due to the heterogeneity of NP aggregates, this problem can be overcome by studying the aggregate at the single-particle level. First, the aggregation time scale was roughly estimated by DLS (Fig 2. 13 open triangles). The size

of aggregates in the colloid solution started to increase 20 min after the addition of 50 nM target ssDNA, and the aggregation continued after 120 min, indicating that the aggregation process is still in progress after 1 h of incubation. The change in the ratio of monomer AuNP over time after the addition of 50 nM of target ssDNA was then estimated with DFM as described above (Fig 2.13 closed circles). Interestingly, the ratio of monomers decreased relatively quickly to 20% in the first 15 min, and to 2% of all particles after 60 min. If AuNPs form aggregates based on the particle-cluster model, the ratio of the monomer would decrease with a time scale similar to that observed by DLS. Therefore, the particle-cluster aggregation model is unlikely to account for our results, indirectly suggesting that cluster-cluster aggregation is the dominant model for ssDNA-induced AuNP aggregation in the early stage.

2.4.7 Study of target DNA-induced AuNP aggregation using TEM

The AuNP aggregation caused by addition of target DNA was also studied using transmission electron microscope (TEM). In TEM, a thin specimen is irradiated with an electron beam of uniform current density. Electrons are emitted in the electron gun by thermionic, Schottky, or field emission. The latter are used when high gun brightness and coherence are needed. A three- or four-stage condenser-lens system permits variation of the illumination aperture and the area of the specimen illuminated. The electron-intensity distribution behind the specimen is imaged with a lens system, composed of three to eight lenses, onto a fluorescent screen. The image can be recorded by direct exposure of a photographic emulsion or an image plate in the vacuum, or digitally via a fluorescent screen coupled by a fiber-optic plate to a CCD camera (Reimer & Kohl, 2008).

Increasing amount of target DNA was added to AuNP colloid, incubated for 1 h. The image of the sample on grid was taken on TEM. The spots on TEM images were classified into monomer, oligomer and large aggregates, where oligomer was defined as clusters that contain AuNP number from 2 to 10. The number of AuNPs in all clusters was counted and the size distribution of AuNP clusters in each condition was calculated to make charts as shown in Fig 2.14b.

As shown in Fig 2.14b, with the addition of increasing amount of target DNA, the number of monomer deceased continuously. Large aggregates appeared when the concentration of added target DNA is higher than 5 pM, and their proportion tended to increase with addition of more target DNA. Small oligomers exist even in the DNA-AuNP only colloid without addition of target DNA. Distribution charts reflected the ratio of small oligomers increased when the added target DNA amount is higher than 5 pM.

DFM histogram result showed similar trend of size distribution changes resulting from addition of different target DNA amount into DNA-AuNP. Fig 2.14c showed some representative histograms to illustrate the size changes. In agreement with TEM results, the amount of monomers decreased constantly when the added target DNA concentrations were increased. Big aggregates appeared at relatively high concentration of target DNA (more than 10 pM). Oligomers appeared when small amount of target DNA was added.

TEM is an impressive instrument with a number of advantages. For example, TEMs offer powerful magnification with high-quality and detailed images. The magnification can potentially be over 1 million times or more. TEMs that are able to offer information of surface features, shape, size and structures can be applied in a variety different field.

However, TEM suffers from various drawbacks that include (1) TEMs are large that require special housing and maintenance, (2) the equipment and its maintenance are expensive, and (3) the TEM samples require laborious preparation.

Compared to TEM, DFM requires only a conventional microscope equipped with a light condenser, which is relatively inexpensive. The normal white light source satisfies the DFM measurement without usage of high voltage required by TEM. The samples are spotted onto glass slides, which is a simple process. What's more, the samples can be measured in wet conditions without being dried. This avoids the possible change of conditions (like local salt concentration) during the sample preparation.

2.4.8 Comparison between DFM and DLS

In DLS, also known as quasi-elastic light scattering (QELS), the Brownian motion of sub-micron particles is measured as a function of time. A laser beam is scattered by particles in suspension. The diffusion of particles causes rapid fluctuations in scattering intensity around a mean value at a certain angle. From the scattered light intensity signal, the information about the Brownian motion of the particles and subsequently sizes are retrieved by Photon Correlation Spectroscopy (PCS) or the Frequency Power Spectrum (FPS).

DLS measurement requires only a tiny amount of sample, and the analysis process is fast and simple, which enables it a convenient tool in the laboratory.

However, as an ensemble analysis method, DLS suffers from low resolution; particles much differ in size by 50% or more for DLS to reliably detect two peaks. What's more, a small quantity of small size particles can easily be "hidden" in a much

larger quantity of large size particles. In addition, the samples have to be transparent for DLS measurement.

Compared to DLS, DFM determines scattered light from each particle/cluster, so that neither small particles nor larger particles will be ignored or hidden. Also, DFM requires even less amount of samples (<10 μL).

2.5 CONCLUSION

In this chapter, the author has demonstrated that DFM can be utilized for the highly sensitive detection of DNA-induced AuNP aggregation at the single-particle level. The sensitivity was much better than that obtained with conventional methods such as color change, UV-Vis spectroscopy and DLS.

The DFM results also suggest that the aggregation process in the early stage follows the cluster-cluster aggregation model. These insights should open opportunities for the use of DFM in various analytical methods using NP assembly.

FIGURES IN CHAPTER 2

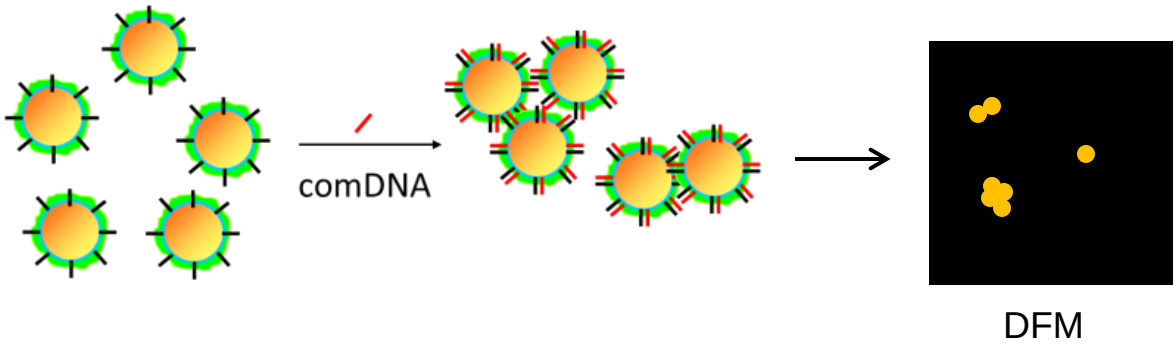

Fig 2.1 Schematic representation of detection of target DNA induced AuNP aggregation using DFM

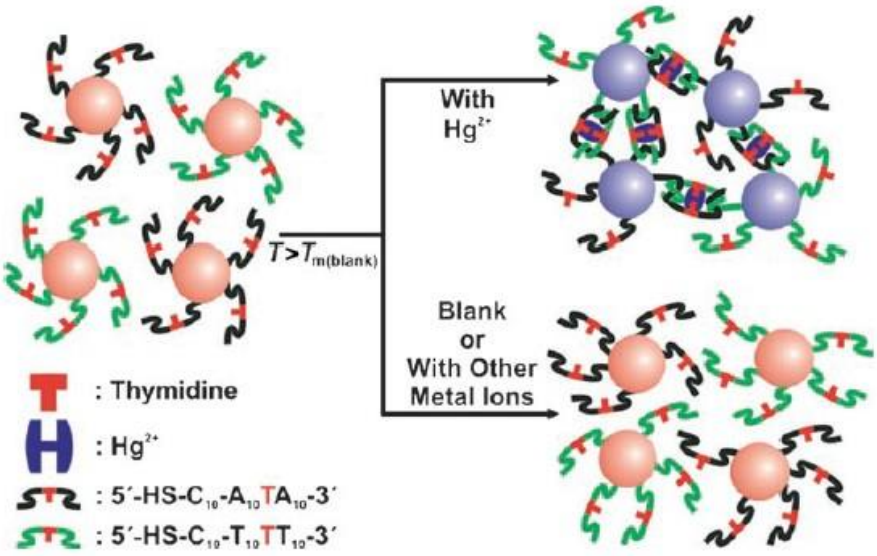

Fig 2.2 Colorimetric detection of mercuric ion (Hg^{2+}) using DNA‑AuNPs.

Figure is taken from ref. (J. S. Lee et al., 2007)

	Sequence	Result	
Target DNA	1. 5′ GGA GCT GGT GGC GTA 3′	Aggregated	Complementary DNA
	2. 5′ GGA GCT GGT GGC G 3′	Aggregated	
	3. 5′ AGGA GCT GGT GGC GTA 3′	Dispersed	Mismatched DNA
	4. 5′ GA GCT GGT GGC GTA 3′	Dispersed	
	5. 5′ CGA GCT GGT GGC GTA 3′	Dispersed	
	6. 5′ TGA GCT GGT GGC GTA 3′	Dispersed	
	7. 5′ AGA GCT GGT GGC GTA 3′	Dispersed	
	8. 5′ GAA GCT GGT GGC GTA 3′	Dispersed	
	9. 5′ GGT GCT GGT GGC GTA 3′	Aggregated	
	10. 5′ GGA GCT AGT GGC GTA 3′	Aggregated	
Probe DNA	3′ CCT CGA CCA CCG CAT 5′ – $(CH_2)_6$ – SH- Au		

Red letters are mismatched nucleotides. 1 M NaCl 20 ℃

Fig 2.3 Aggregation state of Probe-AuNP with addition of complementary DNA or mismatched DNA with SNPs at different sites

(Sato.K; Hosokawa, K; Maeda, M. Unpublished data)

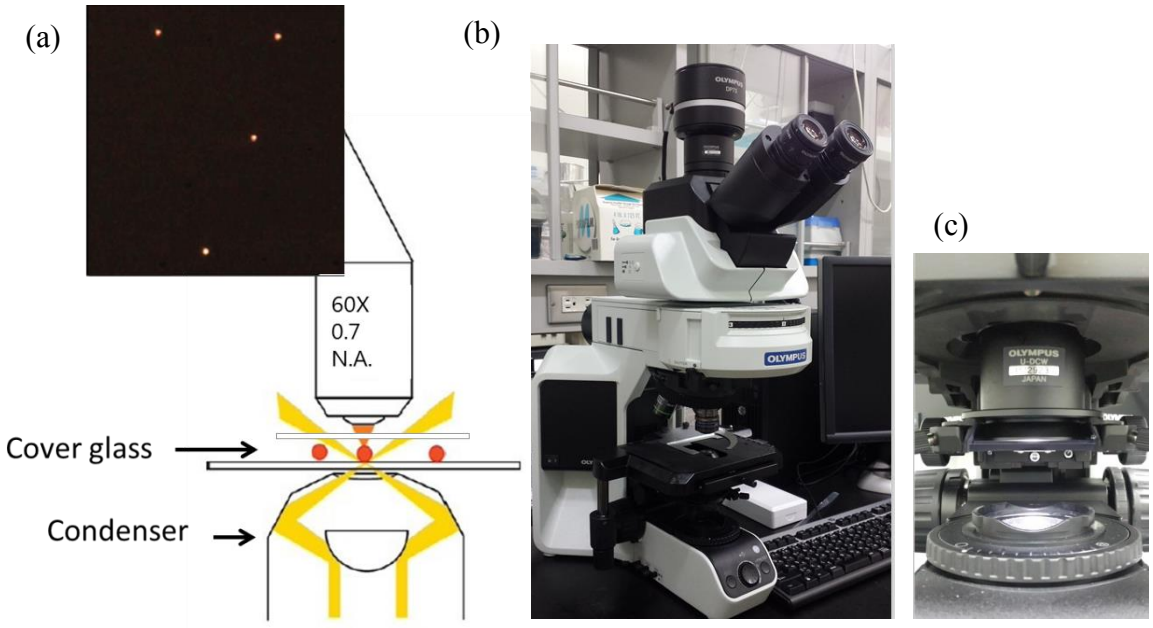

Fig 2.4 Schematic diagram and photo of dark-field microscope used for AuNP aggregation study

(a) Schematic illustration of DFM setup for AuNP study, (b) photo of dark field microscope used in this study, (c) photo of light condenser in the light path.

Figure is taken from ref. (Hu et al., 2008)

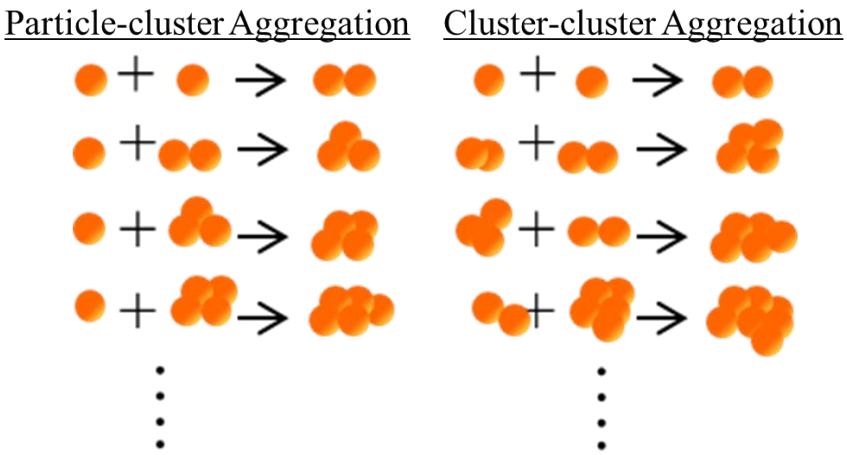

Fig 2.5 Hypothesis of target DNA caused AuNPs aggregation models: particle-cluster and cluster-cluster aggregation.

Figure is adapted from ref. (Hemker & Frank, 1990)

(a)

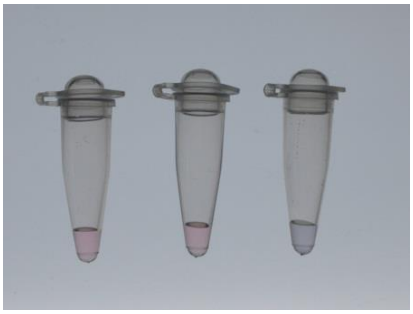

(b)

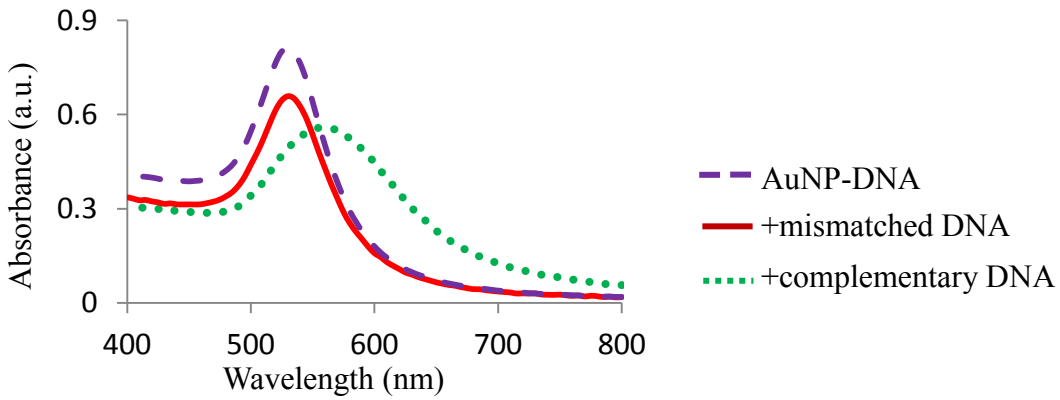

Fig 2.6 Color change and absorption spectrum peak-shift caused by target ssDNA induced AuNPs aggregation.

(a): From left to right: ssDNA-AuNP only; ssDNA-AuNP with addition of 500 nM mismatched DNA; and aggregated ssDNA-AuNP caused by addition of 500 nM target ssDNA (b) Peak-shift of absorption spectrum caused by addition of 500 nM mismatched ssDNA and 500 nM complementary DNA.

(a)

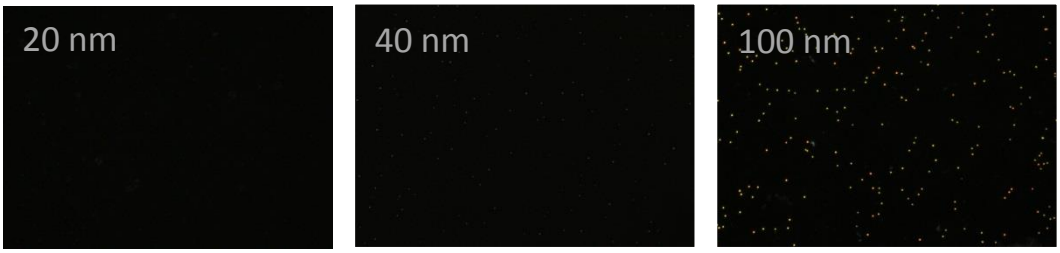

(b)

No signal

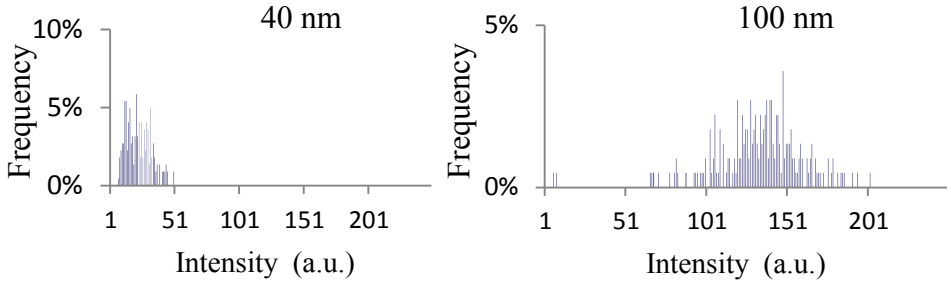

Fig 2.7 DFM images and scattered light intensity histograms of bared AuNP with parameters of 20, 40, and 100 nm.

.)

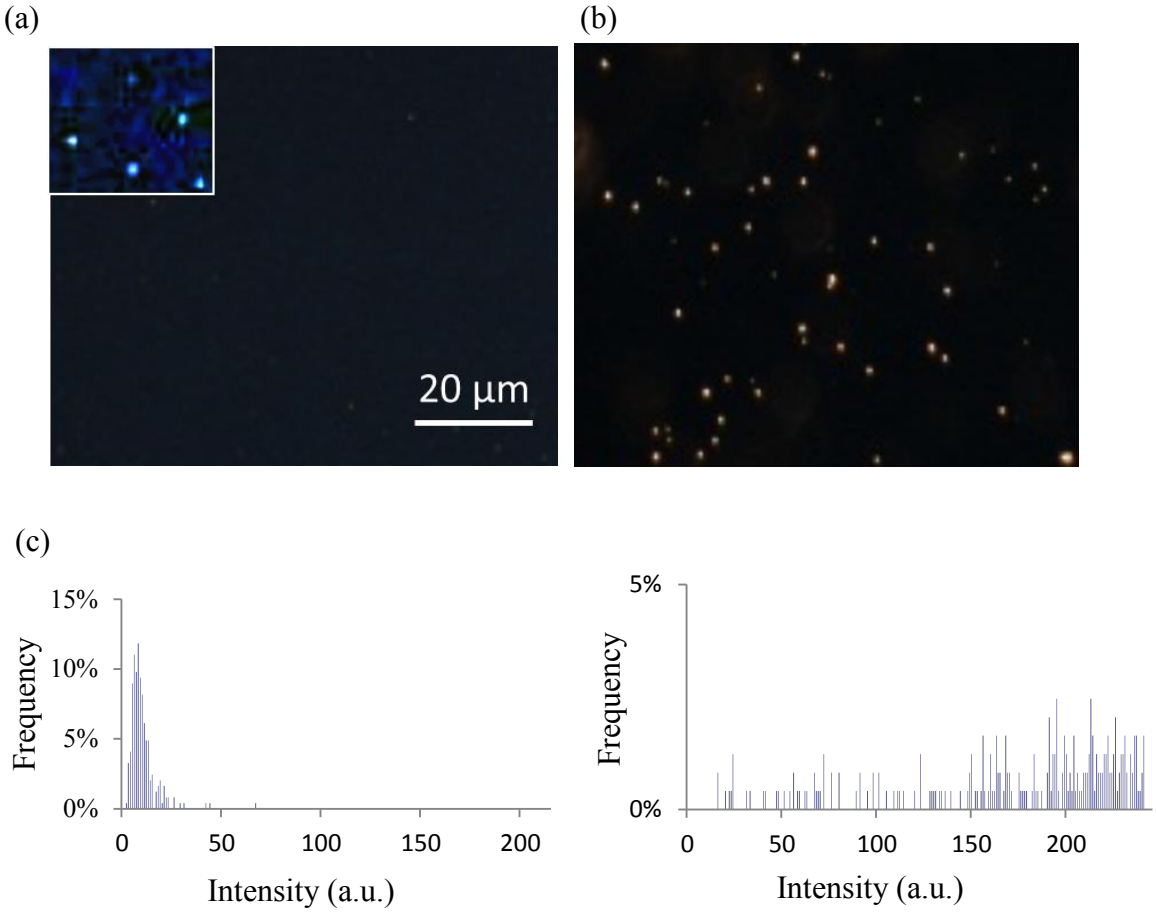

Fig 2.8 DFM images of dispersed AuNP and aggregated AuNPs

(a) Dispersed AuNP without addition of target ssDNA (inset is an enlarged partial image with enhanced intensity) (b) Aggregated AuNPs by addition of target complementary ssDNA (100 nM). The scale bar = 20 µm (c) Histograms drawn from the scattering light intensities of AuNPs in image (a) and (b).

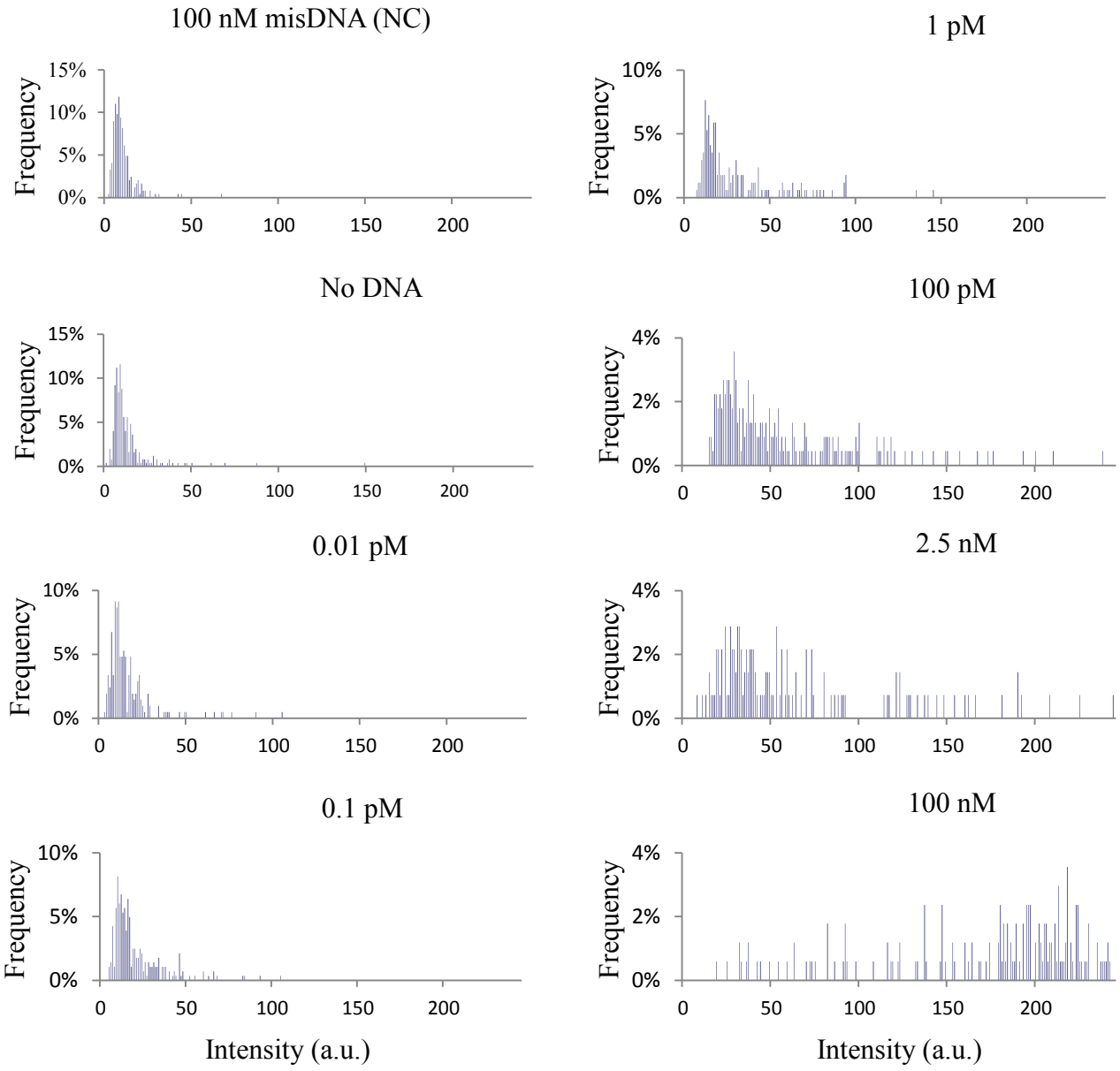

Fig 2.9 Scattering light intensity histograms of AuNPs aggregates observed by DFM

AuNPs aggregation was caused by adding different concentration of the target complementary DNA ranging from 0 to 100 nM (number of spots > 200). Mismatched ssDNA (100 nM) was added as a negative control (NC).

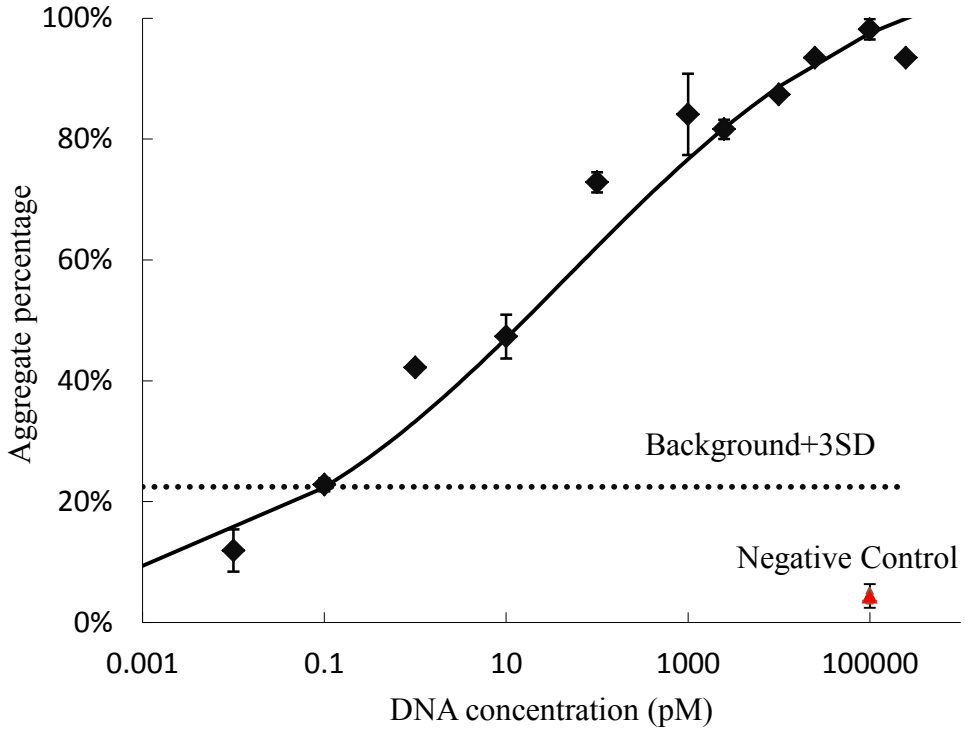

Fig 2.10 Ratio of aggregated AuNPs at various target DNA concentrations.

Mismatched ssDNA (100 nM) was added as a negative control (triangle). The error bars represent standard deviations (SD) of three different histograms. The " 3σ line", indicating background (zeto-concentration, aggregate ratio = 0.11 ± 0.040, n = 6) + 3SD, was used for calculation of the LOD.

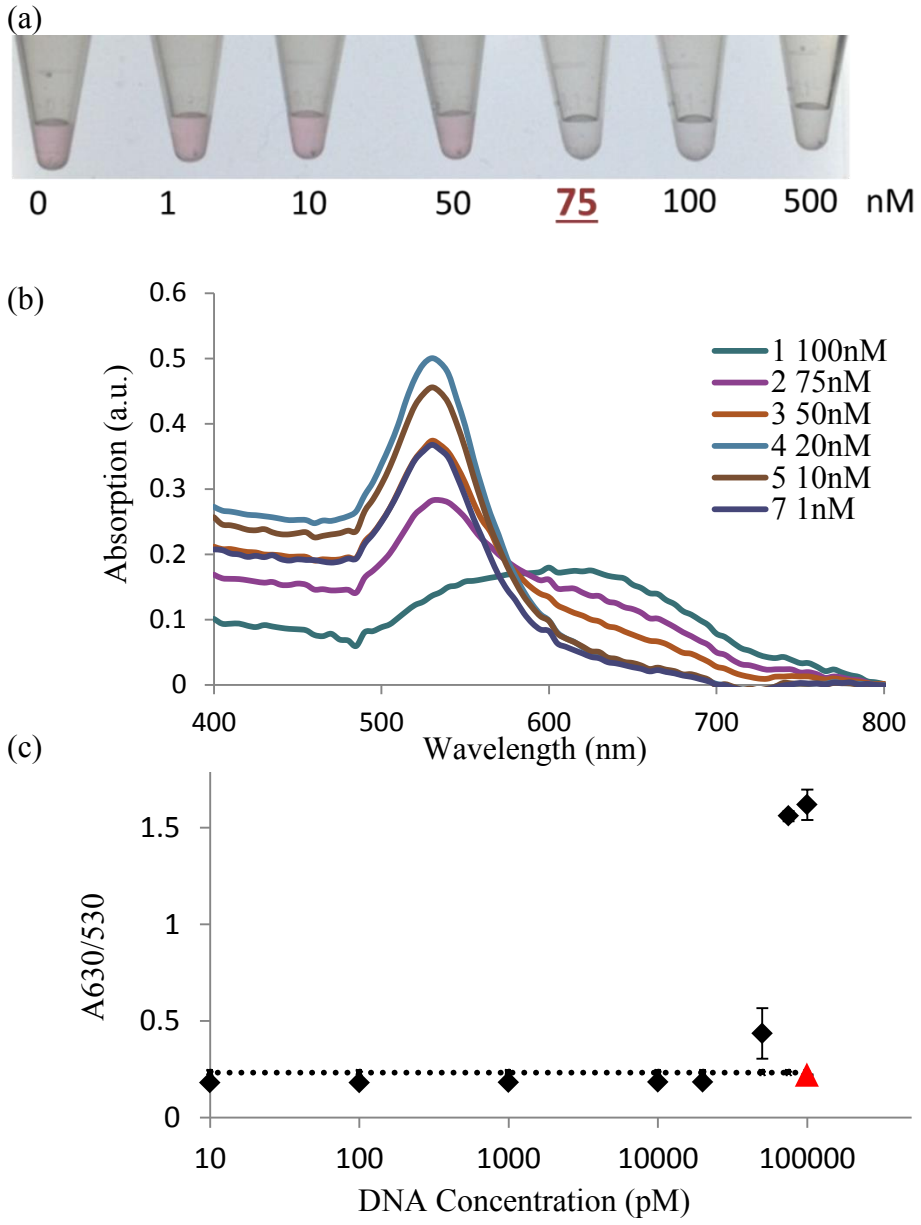

Fig 2.11 Detection limit of AuNPs aggregation by observing color changes and UV-Vis spectroscopy

AuNPs aggregation was caused by addition of increasing amount of target DNA. (a) color changes, (b) UV-Vis spectroscopy, (c) change of absorption ratio (A630/530) in UV-Vis spectroscopy result.

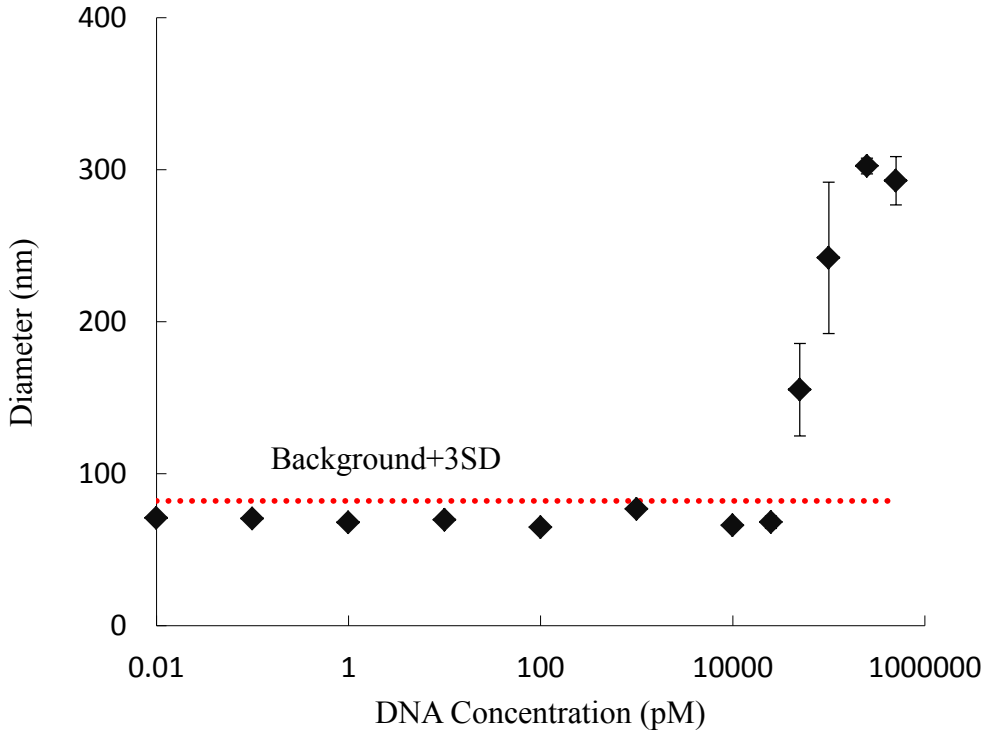

Fig 2.12 Detection limit of AuNPs aggregation caused by addition of increasing amount of target DNA by measuring averaged AuNP particle/ clusters size using DLS

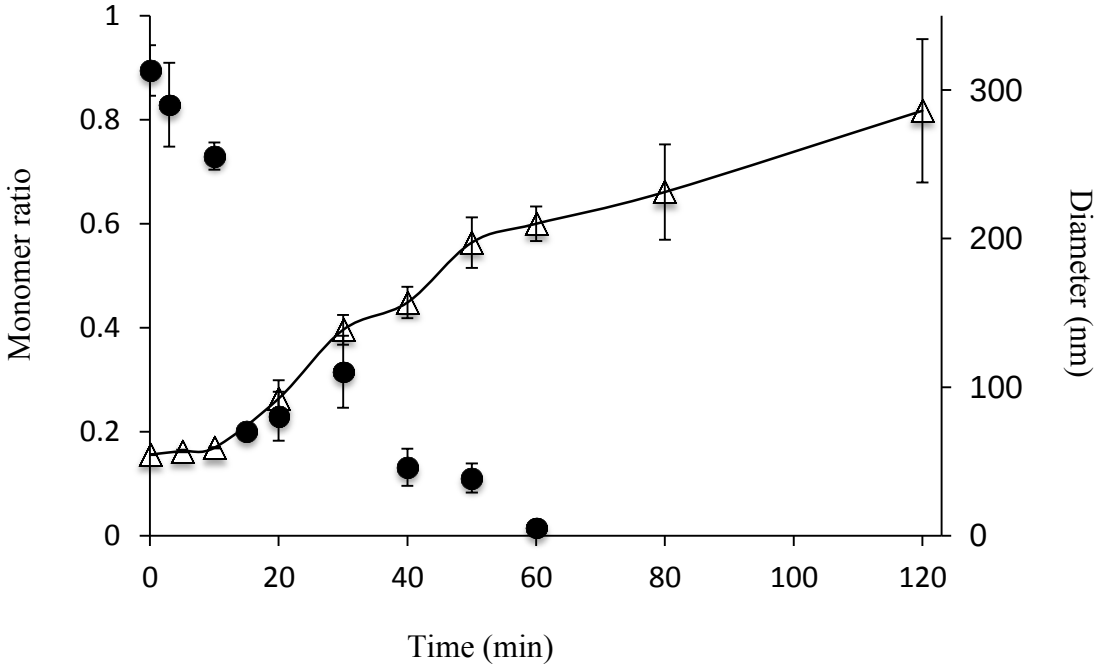

Fig 2.13 DNA induced AuNP aggregation dynamics.

Left axis, change in monomer ratio after the addition of 50 nM of target ssDNA (closed circle) obtained from the histograms of DFM images. Right axis, change in diameter measured by DLS after the addition of 50 nM of target ssDNA (open triangle).

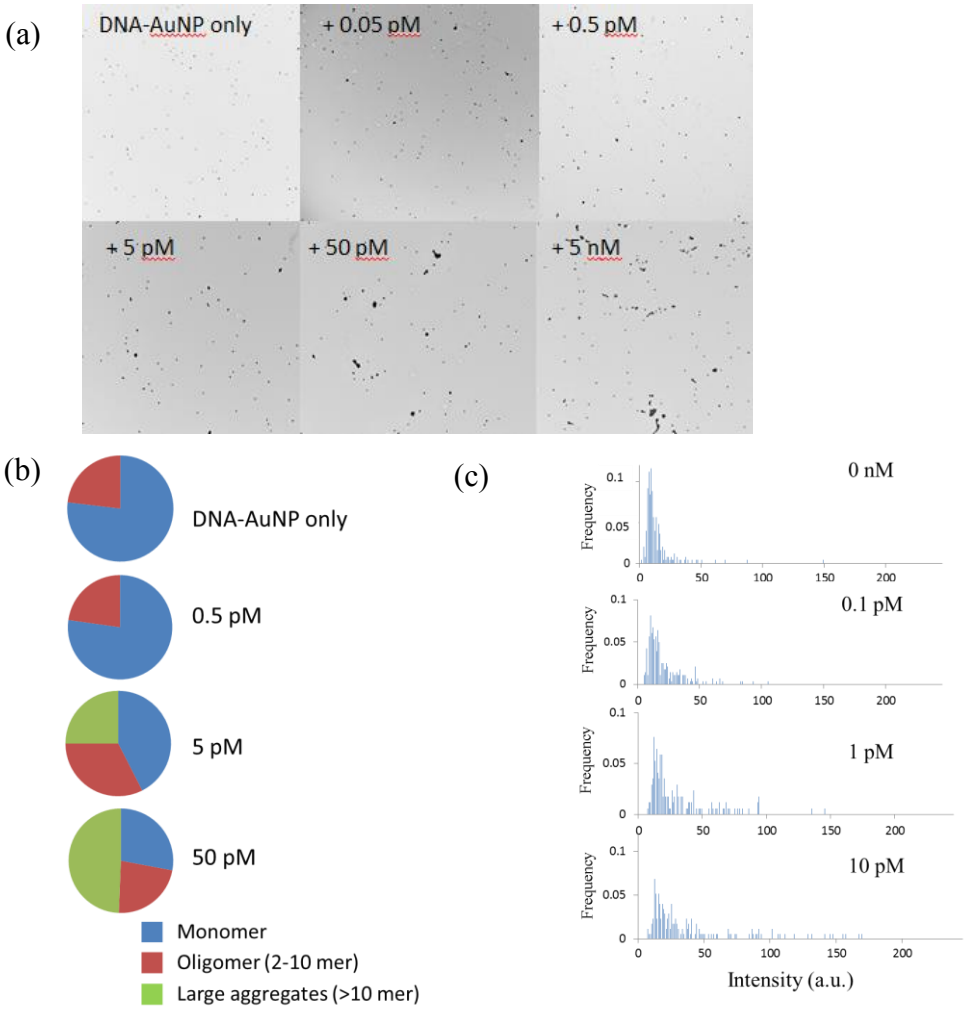

Fig 2.14 Ratio of AuNP aggregation caused by addition of increasing amount of complementary DNA

(a) TEM images of AuNPs and AuNPaggregations caused by addition of increasing amount of complementary DNA. (b) Ratio of aggregated AuNPs calculated from TEM images (a). (c) Representative histograms showing intensity peak shift caused by addition of increasing concentration of complementary DNA.

Chapter 3 Dark field microscopic detection of amyloid aggregates using AuNPs modified with antibody

3.1 SUMMARY

The Aβ protein is a 39- to 43-amino acid polypeptide that is the primary constituent of senile plaques and cerebrovascular deposits in Alzheimer's disease (AD) (Yankner, Duffy, & Kirschner, 1990). This amphiphilic peptide spontaneously forms aggregates in aqueous solutions at or below physiological pH. The formation of Aβ aggregates is considered to cause AD neuro-degeneration by affecting brain nerve cells. Therefore, detection of Aβ aggregates is important for early recognition of diseases.

Previous study reported that amyloid aggregates can be detected by the precipitation of AuNPs conjugated with Aβ antibodies (Sakono, Zako, & Maeda, 2011). Red-colored precipitates can be seen by naked-eye by addition of 5 μM Aβ aggregates into AuNP-antibody (Ab-AuNP) colloid. However, since averaged Aβ protein levels in cerebrospinal fluid (CSF) is around 0.1 nM, the previously stated detection method is not sensitive enough for practical clinical use. In an aim to achieve higher sensitivity of Aβ aggregates detection, DFM was utilized to detect the Aβ aggregates-induced AuNPs assembly. The LOD of Aβ oligomer and fibrils using this method reached as low as pM level. (Fig 3.1)

3.2 BACKGROUND AND INTRODUCTION

3.2.1 Alzheimer's disease and Aβ

Alzheimer's disease (AD) is the most common age-related neurodegenerative disorder, and one of the most devastating diagnoses that patients and their families can

receive (LaFerla, Green, & Oddo, 2007). AD case was firstly reported by Alois Alzheimer in a lecture at a congress in Germany (Möller & Graeber, 1998). Current estimates of AD incidence are more than 24 million worldwide, a number that is predicted to double every 20 years, reaching 81 million in 2040 (Blennow, de Leon, & Zetterberg).

In the single case reported by A. Alzheimer, the typical clinical characteristics with memory disturbances and the appearance of military bodies (plaques) and dense bundles of fibrils (tangles) were known as the hallmarks of the disease. As shown in Fig 3.2, the AD is characterized with senile or neuritic plaques and neurofibrillary tangles in the medial temporal lobe structures and cortical areas of the brain, together with degeneration of the neurons and synapse (Blennow et al.). In 1985, Masters and coworkers succeeded for the first time to purify and characterize the cerebral amyloid protein that forms the plaque core in AD and in aged individuals with Down syndrome. They found that the protein consists of multimeric aggregates of a polypeptide of about 40 residues named Aβ (Masters et al., 1985). This find paved the way for the cloning of the parental amyloid precursor protein (APP) gene (Blennow et al.; Kang et al., 1987).

Aβ is produced by endoproteolysis of the APP, which is achieved by the sequential cleavage of APP by groups of enzymes or enzyme complexes including α-, β-, γ- secretases (Fig 3.3) (LaFerla et al., 2007). The cleavage and processing of APP into Aβ can be divided into a non-amyloidogenic pathway and an amyloidogenic pathway. In the non-amyloidogenic pathway, APP is cleaved by the α-secretase at a position 83 amino acids from carboxy (C) terminus, and resulting 83-amino-acid C-terminal fragment (C83) is retained in the membrane and subsequently cleaved by the γ- secretase (Haass, Hung, Schlossmacher, Teplow, & Selkoe, 1993; Kojro & Fahrenholz, 2005).

The amyloidogenic pathway is initially mediated by the β-secretase at a position located 99 amino acids from the C terminus. The resulted N-terminus peptide is cleavage by the γ-secretase liberates an intact Aβ peptide. Most of the Aβ produced contained 40 residues ($A\beta_{40}$), whereas about 10% of the products contain 42 residues ($A\beta_{42}$). $A\beta_{42}$ variant is more hydrophobic and has a higher tendency to aggregate into oligomer or higher ordered fibril formations (Jarrett, Berger, & Lansbury Jr, 1993). In addition, $A\beta_{42}$ is the predominant isoform found in cerebral plaques (Younkin, 1998). In its monomeric state, Aβ does not appear to be neurotoxic. By contrast, oligomeric and protofibrillar species are considered potent blockers of long-term potentiation, a form of synaptic plasticity (Walsh et al., 2002).

3.2.2 Aβ aggregates and their toxicity

As stated ahead, Aβ is produced as monomer, but it is prone to assembly states ranging from low molecular weight dimers and trimmers to higher molecular weight protofibrils and fibrils (Fig 3.4) (Sakono & Zako, 2010). It is the ability of this peptide to form fibrils and other intermediate states that impart the unique pathophysiological characteristics that define Alzheimer's disease pathology (LaFerla et al., 2007).

Fibril formation is a complex, nucleation-dependent process. The mechanism driving this process, particularly in the elderly brain, is not yet known, but it appears to be closely related to protein misfolding (LaFerla et al., 2007). Although the precursor proteins in different diseases do not share sequence homology or related native structure, the morphology and properties of all amyloid fibrils are remarkably similar (Lührs et al., 2005). Blake and coworkers reported that size different ex vivo amyloid fibrils and two synthetic fibril preparations all gave similar high-resolution X-ray fiber diffraction

pattern, consistent with a helical array of β-sheets parallel to the fiber long axis, with the strands perpendicular to this axis. This confirms that amyloid fibrils comprise a structural superfamily and share a common protofilament substructure, irrespective of the nature of their precursor proteins (Sunde et al., 1997).

Early hypotheses for disease pathogenesis proposed that 6- 10 nm mature amyloid fibrils are the primary causative agent in pathogenesis, but it was found that the accumulation of large aggregates does not correlate well with pathogenesis, which suggested that role of oligomers or aggregation intermediates (Kayed & Glabe, 2006).

The oligomeric species of Aβ have been found to be the most pathological. K.H. Ashe and coworkers reported that soluble oligomeric forms of Aβ, including trimmers and dimers, were both necessary and sufficient to disrupt learned behavior in a manner that is rapid, potent and transient; they produced impaired cognitive function without inducing permanent neurological deficits (Cleary et al., 2005). Walsh also described how dimers were found to disrupt learning and memory, synaptic function and long term potentiation (Walsh et al., 2002). Aβ dodecamers affect cognition and memory in transgenic mouse models (Lesné et al., 2006).

3.2.3 Detection methods of Aβ aggregates

Investigating the role of amyloid aggregates in pathogenesis presents a problem for distinguishing these aggregates from soluble monomer (Kayed & Glabe, 2006). Our understanding of amyloid has advanced with the available technology. (Sipe & Cohen, 2000)

The fibrils were firstly observed with the help of stains. Rudolph Virchow introduced and popularized the term amyloid to denote a macroscopic tissue abnormality

that exhibit a positive iodine staining reaction (Cohen, 1986). Later, the inherent birefringence of amyloid deposits that stained with Congo red dye was observed by optical microscopy with polarizing optics (Sipe & Cohen, 2000).

In 1959, electron microscopic examination of ultrathin sections of amyloidotic tissues revealed the presence of fibrils (Cohen, 1986). X-ray diffraction analyses of isolated amyloid protein fibrils revealed that all proteinaceous amyloid fibrils were ordered in secondary structure, with the polypeptide backbone assuming the beta pleated sheet conformation and oriented perpendicular to the fibril axis (Sipe & Cohen, 2000; Sunde & Blake, 1998).

Thioflavin T (ThT), an extrinsic fluorescence of the benzothiazole dye, is widely used for the identification and quantification of amyloid fibrils *in vitro*, and has become the premier technique used to monitor fibrillation kinetics in real-time (Ban, Hamada, Hasegawa, Naiki, & Goto, 2003; Bolder, Sagis, Venema, & van der Linden, 2007; Hawe, Sutter, & Jiskoot, 2008; Hudson, Ecroyd, Kee, & Carver, 2009; Mahmoudi, Kalhor, Laurent, & Lynch, 2013). Free ThT shows only weak fluorescence, with excitation and emission maxima at 350 and 440 nm respectively. However, when ThT is added to amyloid fibril samples, its fluoresce is enhanced strongly with excitation and emission maxima at approximately 440 and 490 nm (Levine, 1993). Although the mechanism of interaction between ThT and amyloid fibrils remains poorly understood, the most widely accepted theory involves the interaction of ThT molecules within grooves between solvent-exposed side chains of the amyloid fibril that run parallel to the fibril axis (Hawe et al., 2008; Hudson et al., 2009; Krebs, Bromley, & Donald, 2005). However, it was reported that in the presence of exogenous polyphenolics compounds (quercetin and curcumin), the strong absorptive and fluorescent properties of quercetin and curcumin were found to significantly bias the ThT fluorescence readings in both *in situ* real-time

ThT assays and single time-point dilution ThT-type assays (Hudson et al., 2009). Thus, it is necessary to develop simple and reliable Aβ aggregates detection method with high sensitivity.

3.2.4 Application of antibody-functionalized AuNPs

Immunoassays take advantage of the specificity and sensitivity of the antibody (Ab) -antigen interaction in order to detect and quantify the amount of a specific analyte present in a sample. Antibodies can be immobilized onto AuNP surface via covalent and/or non-covalent interactions. The non-covalent interaction takes place by hydrophobic interactions, ionic interactions and dative bindings. The attraction between hydrophobic parts of antibody and metal surface contributes to the hydrophobic interaction; the positively charged amino acids in antibody interacts with the negatively charged AuNP surface via ionic interactions; formation of covalent bond between the gold particle and free sulfhydryl groups of the antibody results in dative bindings.

Taking advantages of specific optical properties of AuNPs, the antibody-AuNP conjugates (Ab-AuNP) are used in disease diagnosis. For example, Ramanaviciene and coworkers developed an indirect, robust and simple in application method for the detection of bovine leukemia virus antigen *gp51*. Magnetic AuNPs modified by antibodies in oriented or random manner were used for the binding and detection of *gp51*, with an LOD to be 0.95 μg mL^{-1} (Baniukevic et al., 2013).

Sakono and coworkers reported their development of a rapid method for estimating the Aβ-confirmation states. They prepared Ab-AuNP (200 nm) conjugates reacted with bovine serum albumin to stabilize their dispersion in PBS buffer. The prepared AuNPs were precipitated in the presence of Aβ aggregates, such as oligomers

and fibrils, while Aβ monomers did not precipitate AuNPs. The formation of AuNP precipitates by Aβ aggregates could be confirmed by the naked eye within 1 h with LOD of about 5 μM (Sakono et al., 2011).

3.3 MATERIALS AND METHODS

3.3.1 Materials

$A\beta_{42}$ peptide was purchased from Peptide Institute (Osaka, Japan). RPMI 1640 medium were purchased from Sigma (St. Louis, MO). Mouse monoclonal antibody to beta amyloid (6E10) and antibody for oligomer (4G8) were purchased from Abcam (Cambridge, UK). HRP conjugated with anti-mouse immunoglobulin G (IgG) were from R&D systems (Minneapolis, MN). Enhanced chemiluminescence (ECL) was purchased from GE Healthcare. The cell proliferation kit (MTT) was purchased from Roche (Indianapolis, IN).

3.3.2 Preparation of Aβ samples

Seed-free Aβ monomers were prepared according to a previous report (Hasegawa, Yamaguchi, Omata, Gejyo, & Naiki, 1999; Sakono et al., 2011). Briefly, synthetic Aβ was dissolved in a 0.1% ammonia water solution at 500 μM, followed by centrifuging at 100,000 rpm for 3 h at 4℃ by Optima TL Ultracentrifuge (Beckman Instruments, Fullerton, CA) to remove undissolved peptide aggregates. The supernatant was collected and stored in aliquots at -80℃. Before usage, the aliquots were thawed on ice and diluted with PBS. Fibrils were prepared by incubating the Aβ monomer stock, diluted to 25 μM in PBS for 24 h at 37℃.

The Aβ oligomer was prepared according to Glabe *et al*. (Kayed & Glabe, 2006; Kayed et al., 2003). In brief, Aβ stock solution (2 mM) were prepared by dissolving the lyophilized peptide in 100 mM NaOH followed by water bath sonication for 30 s. The oligomerization reaction was initiated by diluting the stock solution in PBS (45 μM final Aβ concentration) and incubated at room temperature for up to 2 days. Oligomer formation was confirmed by Native-PAGE/western blot.

3.3.3 Immobilization of Aβ antibodies on AuNP

The Aβ antibodies were immobilized on AuNP surface according to the previous reported protocol (Sakono et al., 2011). Briefly, a 100 μL aliquote of AuNP (BBI, UK) was centrifuged at 6,000 rpm for 10 min. The supernatant was removed and AuNP precipitates were suspended into 100 μL 10-times diluted PBS including 50 nM Aβ antibody (6E10 antibody for fibril and A11 antibody for oligomer), followed by incubation for 1 h at room temperature. After incubation, 100μL 10-times diluted PBS containing BSA was added to the microtube, followed by incubation for 30 min at room temperature. The microtube was then centrifuged at 6,000 rpm for 5 min, and the supernatant was removed. The resulting 6E10 or A11 antibody conjugates (6E10-AuNP or A11-AuNP) precipitates were re-suspended in 1×PBS and used for further study.

3.3.4 Optimization of antibody immobilization on AuNP-- role of BSA

Ab-AuNP was incubated with increasing concentration of BSA for 8 h followed by centrifuging at 6,000 rpm for 5 min. The Ab-AuNPs were then suspended in PBS buffer. The adsorption spectra were taken to check whether there is AuNP assembly.

3.3.5 Optimization of antibody immobilization on AuNP-- buffer concentration and pH

To look for the best PBS buffer concentration for AuNP assembly system, AuNPs of 40 nm were centrifuged at 6,000 rpm for 5 min and then dispersed in 1/10, 1/6, 1/4, 1/3, 1/2 diluted PBS buffer with pH 7.4 and pH 4.2 separately. After incubated for 1 h, AuNP aggregation status was determined by color change of the colloid.

3.3.6 Optimization and quantification of the immobilization of 6E10 antibody on AuNP surface

To optimize the immobilization efficiency of 6E10 antibody on AuNP surface, different PBS concentration (1/6 diluted and 1/4 diluted) and different pH (7.4 and 4.2) was used to disperse Ab-AuNPs.

Dot blot assay was performed to quantify the amount of antibodies immobilized on surface of AuNPs. Colloid of 6E10-AuNP conjugates (2 μl) was spotted onto nitrocellulose membrane (0.22 μm, Whatman, Kent, UK). Increasing concentration of 6E10 (0, 0.5, 1, 2.5, 5, 7.5, 10, 25 nM) was also spotted onto the nitrocellulose membrane for making the standard curve.

The membrane was then blocked with 5% skim milk in TBS containing 0.01% Tween 20 (0.01% TBST) for 1 h at room temperature and incubated with secondary HRP-conjugated mouse anti-IgG antibody (1:2000). Proteins were visualized using the ECL plus blotting detection system according to the manufacturer's instructions. Luminescence was detected in a LAS 4000 mini luminescent Image Analyzer (Fujifilm, Tokyo, Japan), with the Image Reader LAS 4000 software. Software Image J was used for determining the intensity of each spot, which quantifies the protein amount on membrane.

3.3.7 Quantification of the immobilization of A11 antibody on AuNP surface

Dot blot assay was performed to quantify the amount of A11 antibody immobilized on surface of AuNPs. A11-AuNP samples (2, 4, and 6 μl) were spotted onto nitrocellulose membrane. Increasing concentration of A11 antibody (0, 0.5, 1, 2.5, 5, 7.5, 10, 25 nM) was also spotted onto the nitrocellulose membrane for making the standard curve. The membrane was then blocked with 5% skim milk in TBS containing 0.01% Tween20 (0.01% TBST) for 1 h at room temperature and incubated with secondary HRP-conjugated rabbit anti-IgG antibody (1:2000). Proteins were visualized using the ECL plus blotting detection system according to the manufacturer's instructions. Luminescence was detected in a LAS 4000 mini luminescent Image Analyzer (Fujifilm, Tokyo, Japan), with the Image Reader LAS 4000 software. Image J was used for quantification.

3.3.8 Dark field microscopy analysis

Similar to the method described in Chapter 2, DFM analysis was performed to reach a higher detection sensitivity of Aβ aggregates. 6 μL of the AuNPs samples were deposited onto glass slides and covered with cover glass. DFM images were taken using BX53 microscope (Olympus, Tokyo, Japan) equipped with UDCW dark field condenser, UPlanFLN 60×objective lens and DP73 CCD camera (Olympus). Images were taken using CellSens Standard software version 1.6 (Olympus). AuNPs were identified as bright orange-colored spots in DFM images and the scattered light intensity of each spot was quantified. The brighter spots that have intensities higher than 45 a.u. were defined as aggregates, since 90% of the dispersed negative control sample to which no Aβ

aggregates was added showed an intensity lower than 45 a.u.. The ratio of aggregates at each target DNA concentration was estimated to calculate the LOD.

3.3.9 Specificity of A11 antibody on surface of AuNP

To confirm the oligomer specificity of A11 antibody after being immobilized on AuNP surface, different concentration (1 nM and 100 nM) of Aβ monomer, oligomer and fibrils were incubated with A11-AuNP colloid for 1 h. 6 μL of mixture were then spotted onto amine-coated glass, and DFM images were taken for determining the scattered light intensities distributions.

The NPs that scattered light less than 35 a.u. were defined as monomer, while NPs that scatters more light than 35 a.u. were defined as AuNP aggregates. The total ratio of aggregated AuNP was calculated for each sample. The comparison of aggregates amount illustrates the specificity of antibody.

3.3.10 Color change and UV-Vis spectrometer for observation of AuNP assembly

As primary experiments, 5 μM monomer, 5 μM fibrils, or 12.5 μM fibrils was added to AuNP colloid, followed by incubation for 1h at RT. The photo-images of tubes were taken by digital camera. The UV-Vis spectra were taken by Cary 50 UV-Vis spectrometer (Varian, Palo Alto, USA)

3.3.11 Calculation of LOD

Various concentrations (from 0 to 5 μM) of Aβ fibril and oligomers were added into the 6E10/A11-AuNP colloid in PBS buffer, and incubated for 1 h at room temperature. Ab-AuNP without addition of Aβ was used as negative control sample.

The LOD was evaluated by the 3σ criterion method, where σ denotes the standard deviation of zero-concentration background data (n=6). Detailed calculation process can be seen in 2.3.6

3.4 RESULTS AND DISCUSSION

3.4.1 Optimization of antibody immobilization on AuNP

6E10 antibody is a monoclonal antibody originated from mouse. It is reactive to amino acid residue 1-16 of Aβ. The epitope lies within amino acids 3-8 of Aβ (EFRHDS). 6E10 antibody was immobilized on AuNP surface via non-covalent interaction. In order to have higher detection sensitivity, higher antibody intensity on AuNP surface is preferred. The immobilization conditions, including roles of BSA, salt concentration of the buffer, were explored at first to optimize the antibody immobilization environment.

Fig3.5.a showed the result of 6E10-AuNP after centrifugation at 6,000 rpm for 5 min. The conjugates of AuNPs and antibodies adsorbed to microtube well easily, so that a proper protection is needed to stabilize the dispersion of AuNPs. Increasing amount of BSA was added into the A11-AuNP colloid, and rotated at room temperature for 8 h. The UV-Vis spectroscopy was measured to determine the AuNP aggregation (Fig 3.5b). Without the protection of BSA, all AuNPs aggregated after 8 h, while the Ab-AuNPs protected by BSA were relatively dispersed though shift of adsorption peak compared to dispersed AuNPs colloid can be observed. 5% BSA was chosen for protection of Ab-AuNPs in the following experiments.

To look for the best PBS buffer concentration for AuNP assembly system, AuNPs of 40 nm were centrifuged at 6,000 rpm for 5 min and then dispersed in 1/10, 1/6, 1/4,

1/3, 1/2 diluted PBS buffer with pH 7.4 and pH 4.2 separately. After incubated for 1 h, the color change was observed by naked eyes. As shown in Fig. 3.6, after being incubated for 1 h in different concentrations of PBS buffers, the color change of AuNP colloid changed when the concentration is higher than 1/3 of original PBS concentration at pH7.4 and pH 4.2, indicating the aggregation of AuNPs in colloid.

3.4.2 Quantification of the immobilization of 6E10 antibody on AuNP surface

To optimize the immobilization efficiency of 6E10 antibody on AuNP surface, different PBS concentration (1/6 diluted and 1/4 diluted) and different pH (7.4 and 4.2) was used to disperse Ab-AuNPs. The dot blot image (Fig 3.7.a, left) showed the increasing darkness of increasing concentrations of 6E10 antibodies, and the right image showed the dot blot result of Ab-AuNPs processed in PBS of various concentrations and pH. The darkness of the spots on dot blot membrane was quantified as Fig 3.7.b. It turned out that in 1/4 diluted PBS buffer at pH 7.4, 6E10 antibody attached to AuNP surface with the highest efficiency. And according to the standard curve shown as Fig 3.7.c, 19.2 nM was attached to AuNP which is 38% (19.2 nM/ 50 nM) of 6E10 antibody added for incubation. On average, there are 192 antibodies (19.2 nM/0.1 nM AuNP) on each AuNP in the colloid.

3.4.3 Detection of Aβ fibrils by color change and UV-Vis spectra

As shown in Fig.3.8, 5 μM monomer, 5 μM fibrils or 12.5 μM fibrils were added to AuNP colloid, followed by incubation for 1h at RT. No obvious color change can be observed by naked eyes (Fig 3.8a), though some precipitates appeared with addition of

12.5 μM fibrils. The absorption spectrum showed neither the visible change with the addition of fibrils (Fig 3.8b).

3.4.4 LOD of DFM method for the detection of Aβ fibrils

Similar with the method described in 2.4.4, the DFM image of 6E10-AuNP with addition of 5 μM monomer and fibril was taken by CCD camera, while the 6E10-AuNP only sample was used as background control (Fig 3.9). As shown in images, fibril added AuNP sample showed much brighter spots than samples with addition of monomer, while the monomer added sample does not show obvious difference with AuNP only colloid.

The size of AuNP aggregates can be estimated by the intensity of each spots in DFM images. Fig 3.10 shows intensity histograms of dispersed and aggregated AuNPs induced by addition of various amount of Aβ fibrils, which indicate the size and number of each AuNP aggregates. As shown in the figure, larger aggregates were observed when an increased amount of Aβ fibrils was added.

The detection limit of the Aβ fibrils concentration was estimated from the ratio of aggregates at each concentration as follows. The brighter spots that have intensities higher than 45 a.u. were defined as aggregates, since 90% of the dispersed negative control sample to which no Aβ was added showed an intensity lower than 45. As shown in Fig 3.11, the ratio of aggregates increased at higher concentrations of the Aβ fibrils.

The LOD was evaluated by the 3σ criterion method as previously reported (Arata et al., 2012), where σ denotes the standard deviation of zero-concentration background data (n=6), and was determined to be as low as 0.04 nM by fitting using a four-parameter logistic function.

3.4.5 Oligomer specific A11 antibody and immobilization of A11 antibody on AuNP surface

A11 antibody is a polyclonal antibody originated from rabbit that recognizes the amino acid sequence-independent oligomers of proteins and peptides. A11 antibody does not recognize monomers or mature fibers of proteins or peptides. For example, A11 antibody reacts with soluble $A\beta_{42}$ oligomers, but does not react with soluble low molecular weight $A\beta_{42}$ or $A\beta_{42}$ fibrils (Fig 3.12a). A11 antibody recognizes oligomeric species of several other amyloidogenic polypeptides including human insulin, prion, polyglutamine, lysozyme, α- synuclein and yeast prion (Kayed et al., 2003).

The amount of Aβ oligomer specific A11 antibody immobilized on AuNPs surface was quantified by dot blot assay. The darkness of spots on dot blot membrane (Fig 3.12b) was plotted as standard curve (not shown), and the amount of A11 antibody on the membrane can be calculated as 9.4 nM. Since 50 nM of A11 antibody was added into AuNP colloid, the attachment efficiency was about 18.8% (9.4 nM/ 50 nM). And the number of antibodies on each AuNP can be calculated as 9.4 nM/ 0.1 nM = 94.

The specificity of A11 antibody after being immobilized onto AuNP was confirmed by DFM analysis. Different concentration (1 nM and 100 nM) of Aβ monomer, oligomer and fibrils were incubated with A11-AuNP for 1 h. Six μL of mixture were then spotted onto amine-coated glass, and DFM images were taken for determining the scattered light intensities distributions. The NPs that scattered light less than 35 a.u. were defined as monomer, while NPs that scatters more light than 35 were defined as AuNP aggregates. The total ratio of aggregated AuNP was calculated for each sample. The comparison of aggregates amount illustrates the specificity of antibody. Fig 3.13a showed the intensity histogram made based on light intensity scattered from AuNPs in the colloid mixture. With the addition of both 1 nM and 100 nM oligomer, NPs

tend to scatter more light than the A11-AuNPs that were mixed with monomers and fibrils. This means AuNP aggregated due to the A11 antibody specificity to oligomers. The ratio of Aβ caused AuNP aggregation was calculated as in Fig 3.13b. Obviously, the addition of oligomer caused A11-AuNP aggregation specifically, which illustrates than A11 antibody keeps its oligomer recolonization specificity after being immobilized onto AuNP surface.

3.4.6 LOD of DFM method for the detection of Aβ oligomers

Oligomer formation was confirmed by native PAGE (See Chapter 4, Fig. 4. 9a). The LOD of DFM method for the detection of Aβ oligomers was also calculated according to the method above. Fig 3.14 shows intensity histograms of dispersed and aggregated AuNPs induced by addition of various amount of Aβ oligomers, and larger aggregates were observed when an increased amount of Aβ fibrils was added.

The detection limit of the Aβ fibrils concentration was estimated from the ratio of aggregates at each concentration (Fig. 3.15). Similar with fibril detection, the brighter spots that have intensities higher than 45 were defined as aggregates. The LOD was determined to be as low as 7 pM by fitting using a four-parameter logistic function.

3.5 CONCLUSION

In chapter 3, DFM was employed to detect the Aβ aggregates, including fibrils and oligomers, induced AuNP aggregation at the single-particle level. The detection sensitivity reached as low as pM level. This study further proved the potential application of DFM in the analytical methods based on AuNP aggregations.

FIGURES IN CHAPTER 3

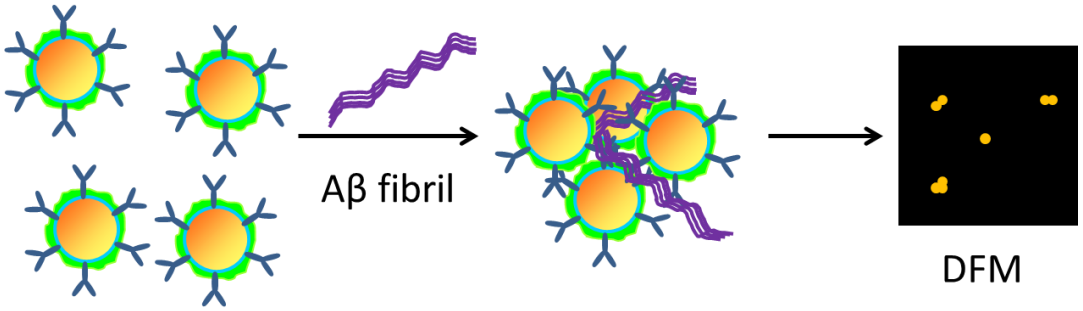

Fig 3.1 Schematic representation showing the detection of Aβ aggregates induced AuNPs aggregation using DFM

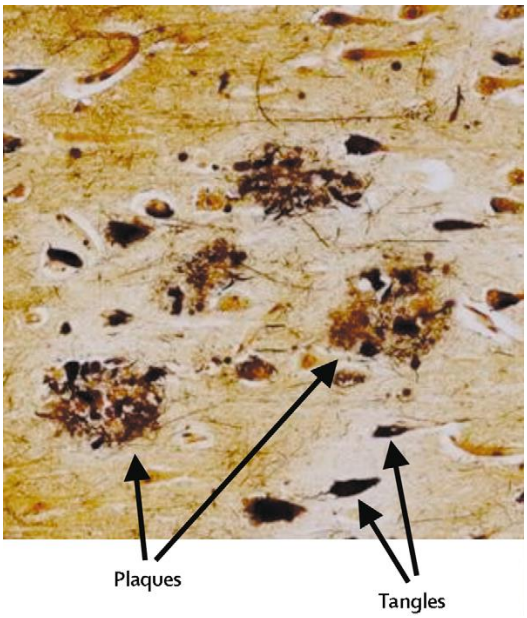

Fig 3.2 Plagues and tangles in the cerebral cortex in Alzheimer's disease.

Plaques are extracellular deposits of Aβ surrounded by dystrophic neuritis, reactive astrocytes, and microglia, whereas tangles are intracellular aggregates composed of a hyperphosphorylated form of the microtubule-associated protein tau.

Figure is taken from ref. (Blennow et al.)

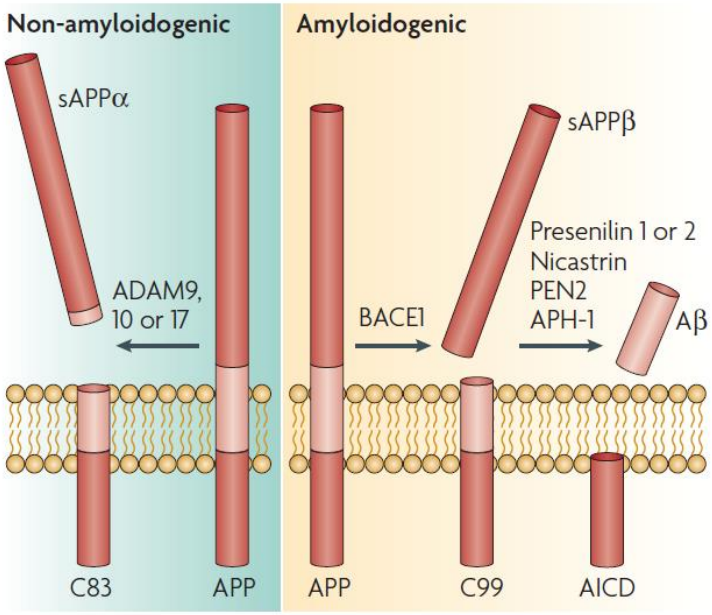

Fig 3.3 APP proteolysis

The amyloid-β (Aβ) peptide is derived via proteolysis from a larger precursor molecule called the amyloid precursor protein (APP). This type 1 transmembrane protein that consisting of 695 -770 amino acids can undergo proteolytic processing by either non-amyloidogenic pathway or amyloidogenic pathway.

Figure is taken from ref. (LaFerla et al., 2007)

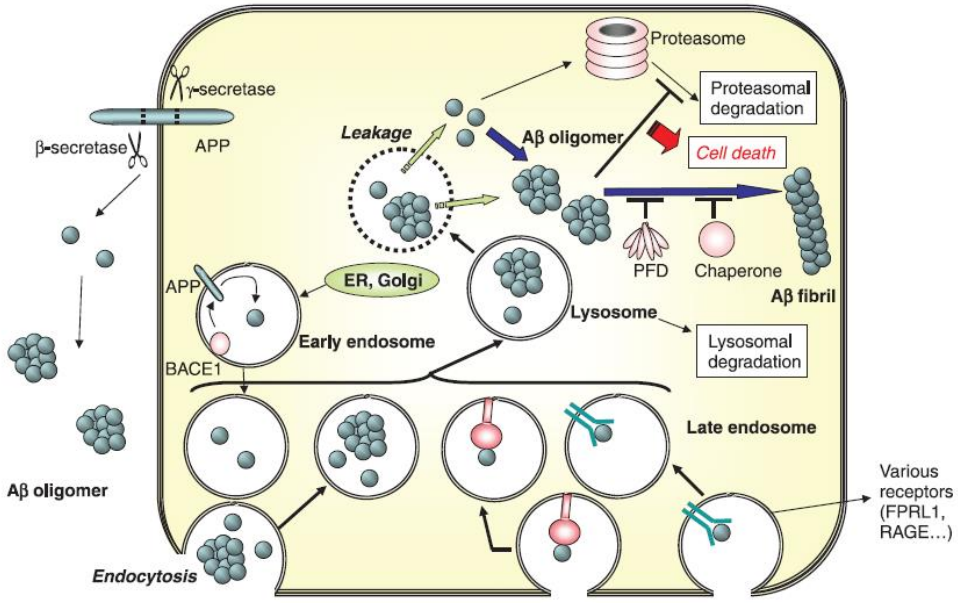

Fig 3.4 Formation and toxicity mechanisms of intracellular Aβ oligomer

Figure is taken from ref. (Sakono & Zako, 2010)

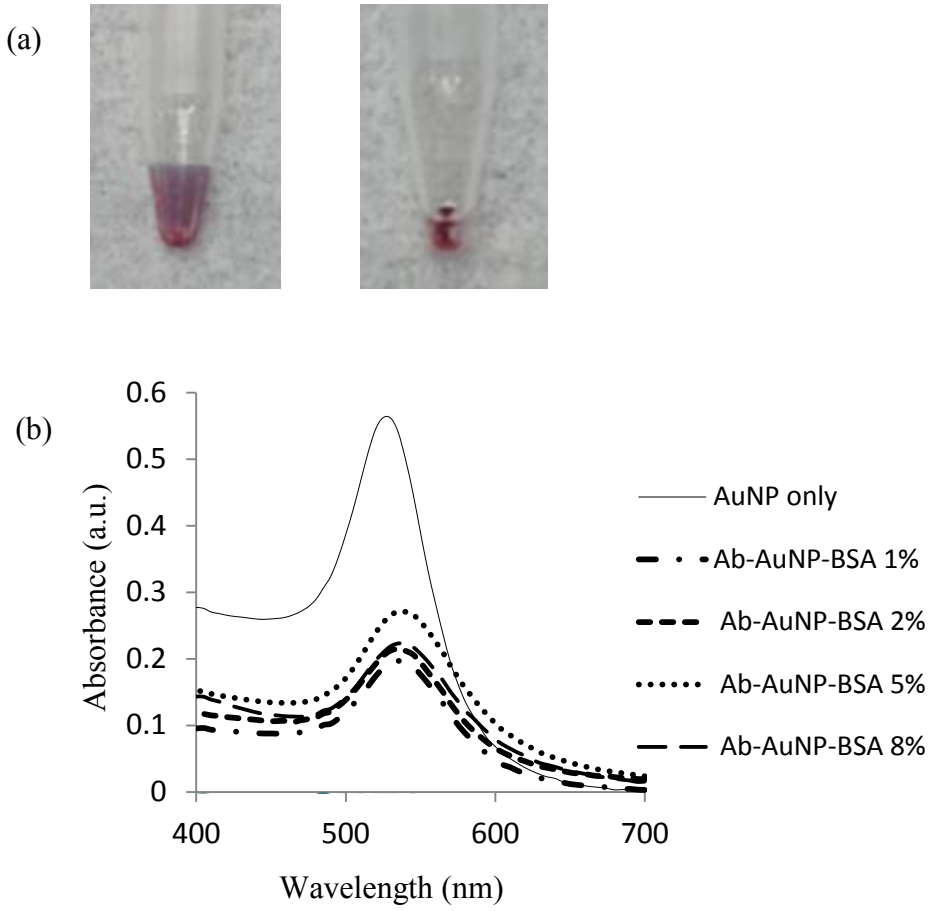

Fig 3.5 Stabilization of Ab-AuNP conjugates using BSA

a) Tube image showed that Ab-AuNP attached to the tube wall after centrifugation (left), while the addition of 5% BSA protected the Ab-AuNP conjugates from adsorption to microtube b) UV-Vis spectroscopy showed the effect of increasing concentration of BSA in stabilizing the AuNP dispersion.

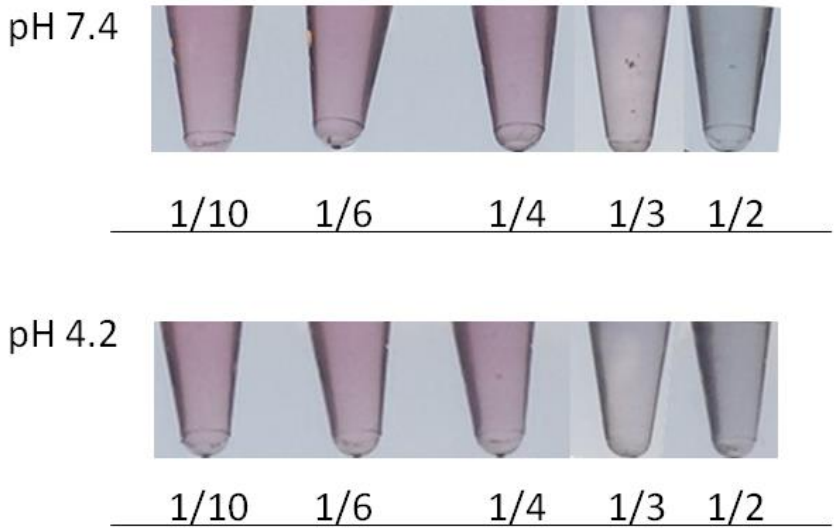

Fig 3.6 Optimization of PBS buffer pH and concentration for antibody immobilization

Bare AuNPs of the same concentration was incubated for 1 h in PBS buffer with different pH (7.4 and 4.2), and increasing PBS concentrations, where PBS was diluted into 1/10, 1/6, 1/4, 1/3 and 1/2 ratios with MQ.

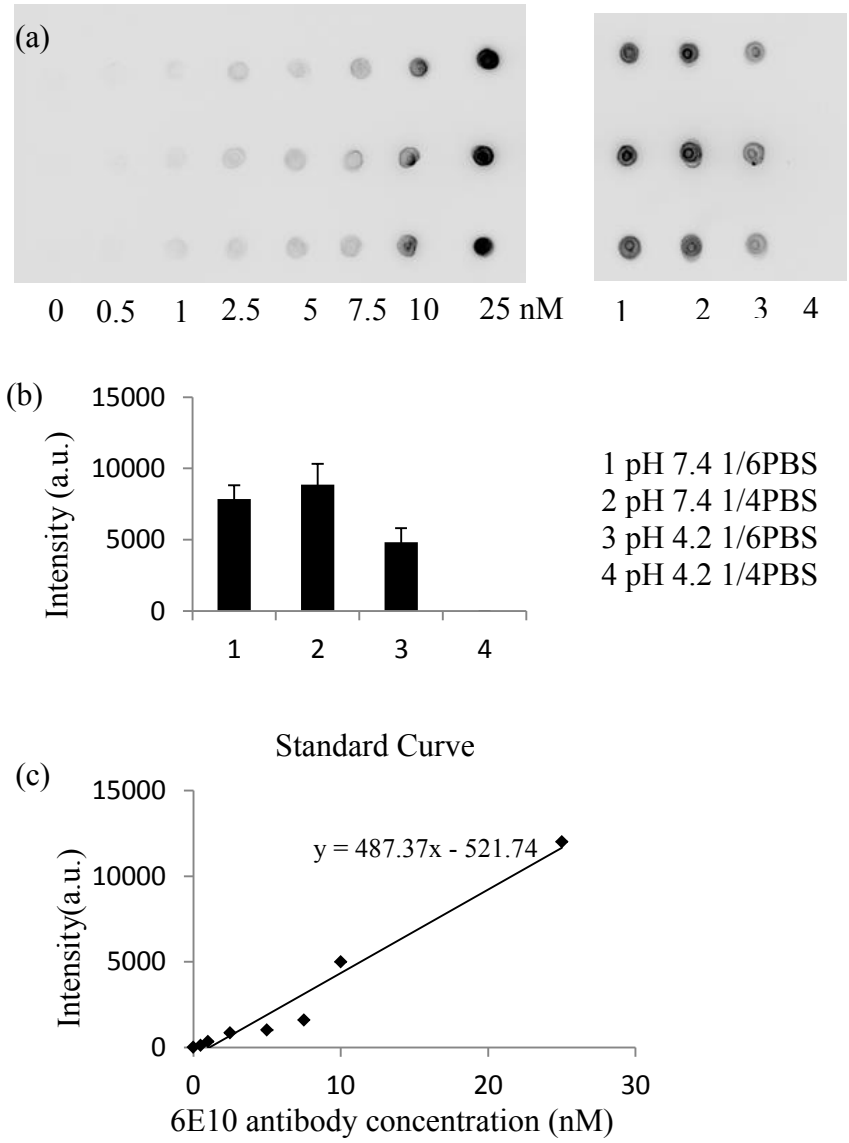

Fig 3.7 Quantification of 6E10 antibody amount immobilized on AuNP surface

(a) Left: Increasing amount of 6E10 antibody was spotted on membrane (0-25 nM); Right: 6E10-AuNP conjugates made by different condition (PBS buffer with different dilution ratio (1/4, 1/6) and different pH (4.2, 7.4)) were spotted onto the membrane. (b) Intensities of 6E10-AuNP conjugates spots (c) Standard curve drawn according to image (a, left).

(a)

(b)

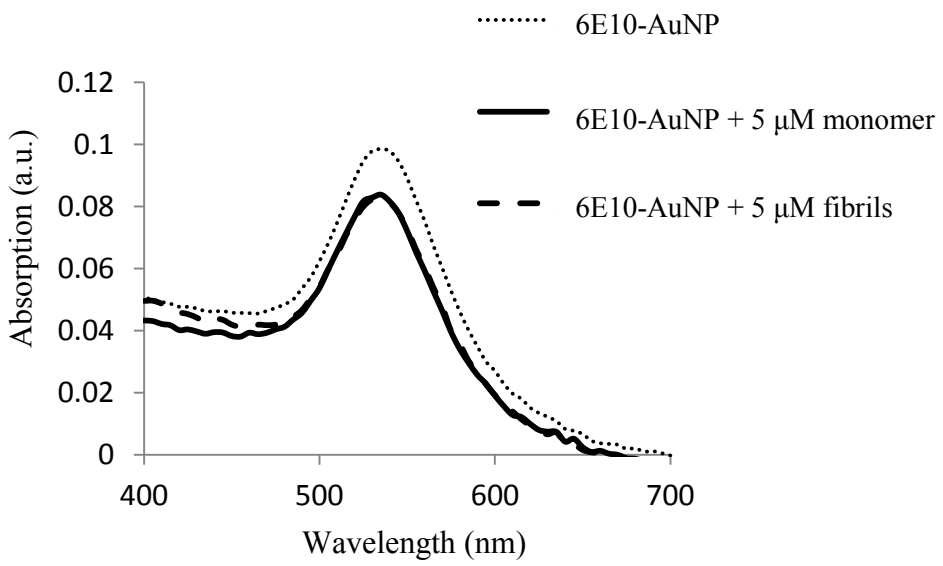

Fig 3.8 Color change and UV-Vis spectroscopy to detect the aggregation of Ab-AuNPs

(a)From left to right, 5μM monomer, 5 μM fibrils or 12.5μM fibrils were added to AuNP colloid, followed by incubation for 1 h at RT. Blue circle shows the area that precipitation appeared. (b) The UV-Vis spectra of samples in (a).

+ 5 μM monomer + 5 μM fibril AuNP only

Fig 3.9 DFM images of 6E10-AuNPs with addition of 5 μM monomer or 5 μM fibril AuNP only (right) was used as negative control. Scale bars represent 20 μm.

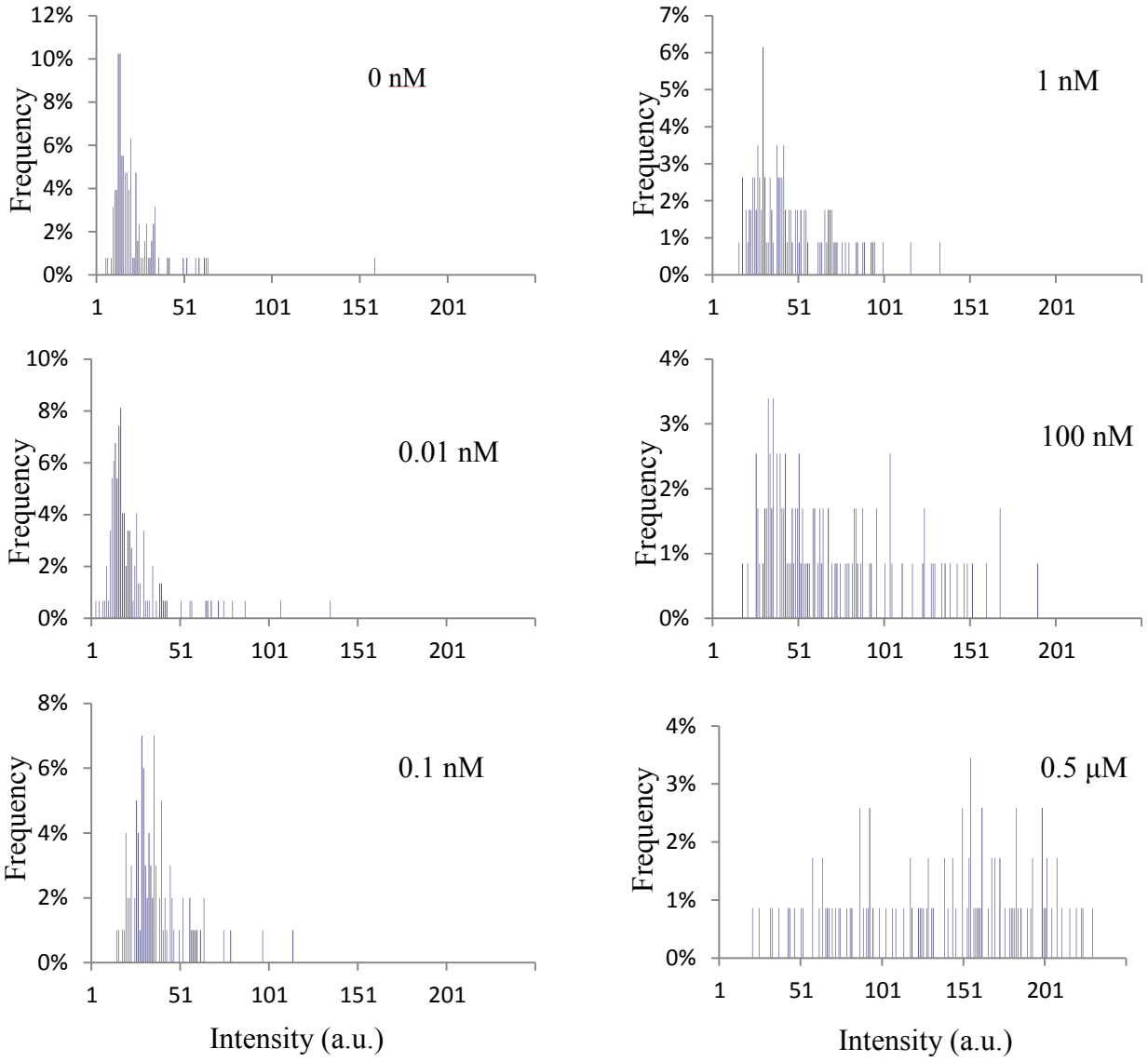

Fig 3.10 Histograms to determine Aβ fibrils detection limit

AuNPs aggregation was caused by adding different concentration of fibrils ranging from 0 to 0.5 µM (number of spots > 200). 6E10-AuNP colloid without addition of Aβ protein was used as background.

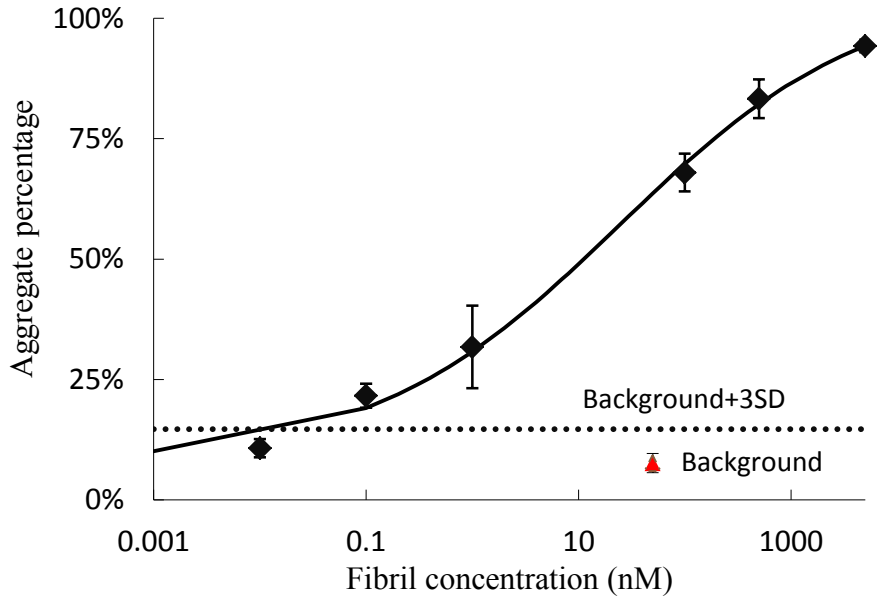

Fig 3.11 Ratio of aggregated 6E10-AuNP conjugates at various fibrils concentrations.

The 6E10-AuNP colloid without addition of any Aβ protein was used as background (triangle). The error bars represent standard deviations of three different histograms. The background + 3SD was used for calculation of the LOD

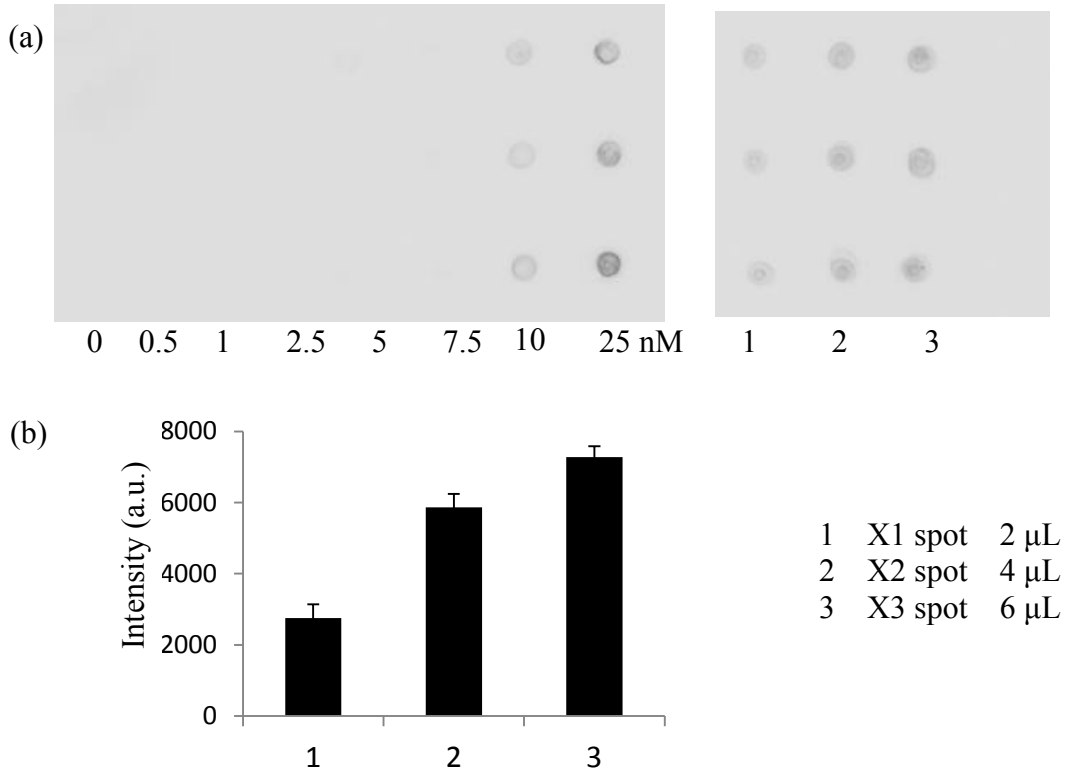

Fig 3.12 Quantification of A11 antibody amount immobilized on AuNP surface

(a) Left: Increasing amount of A11 antibody was spotted on membrane (0-25 nM); Right: different volume of A11-AuNP conjugates (2 µL, 4µL and 6µL) was spotted onto the membrane to calculate the average amount of A11 antibody on A11-AuNP conjugates.(b) Intensity of spots that with 2 µL, 4µL, and 6 µL samples on dot blot membrane.

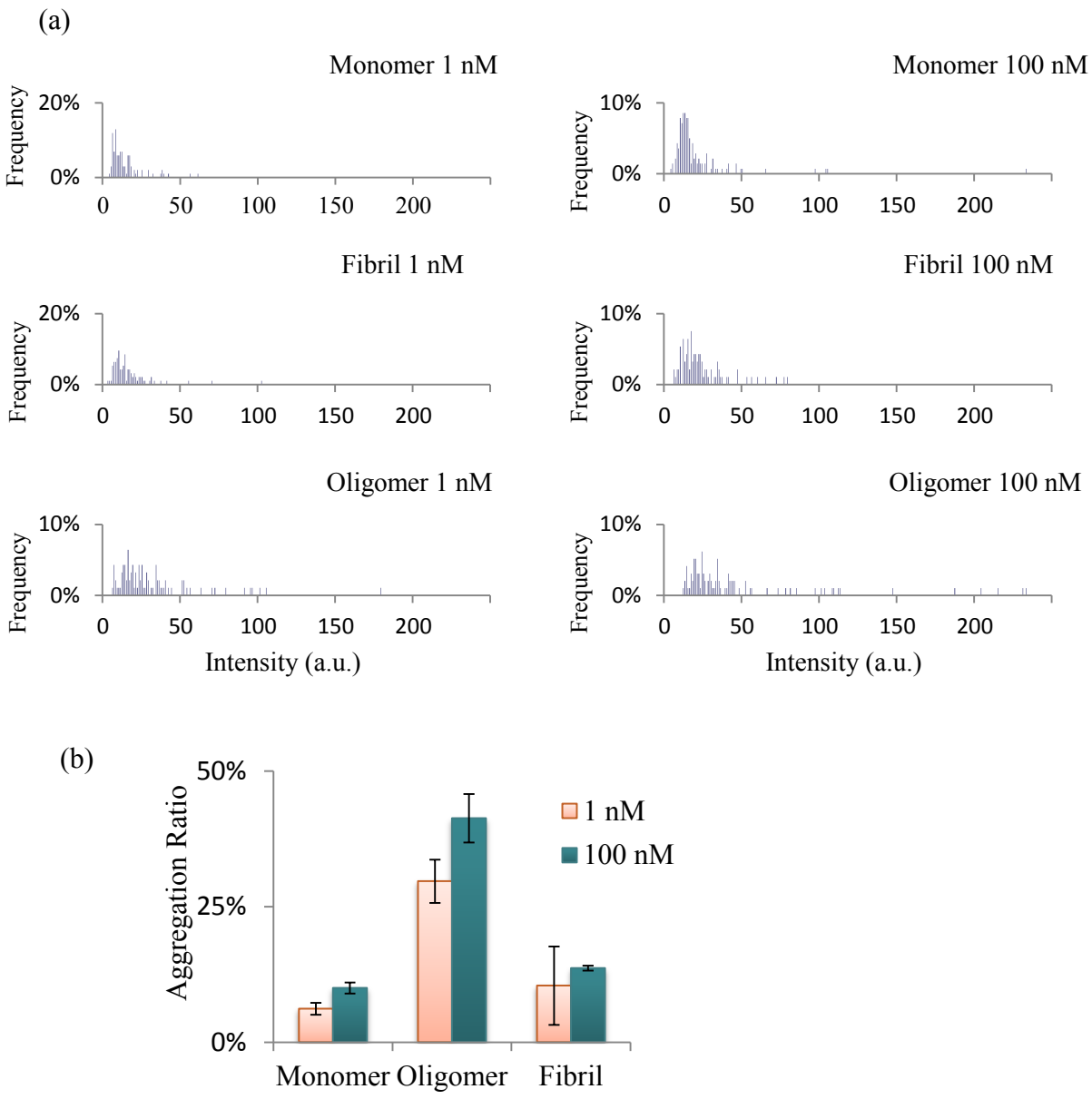

Fig. 3.13 Specificity of A11 antibody on AuNP surface

(a) Histograms of scattered light intensity from A11-AuNP that were incubated with 10 nM and 100 nM of Aβ monomer, oligomer, and fibrils separately for 1 h. (b) Ratio of aggregated AuNPs derived from (a)

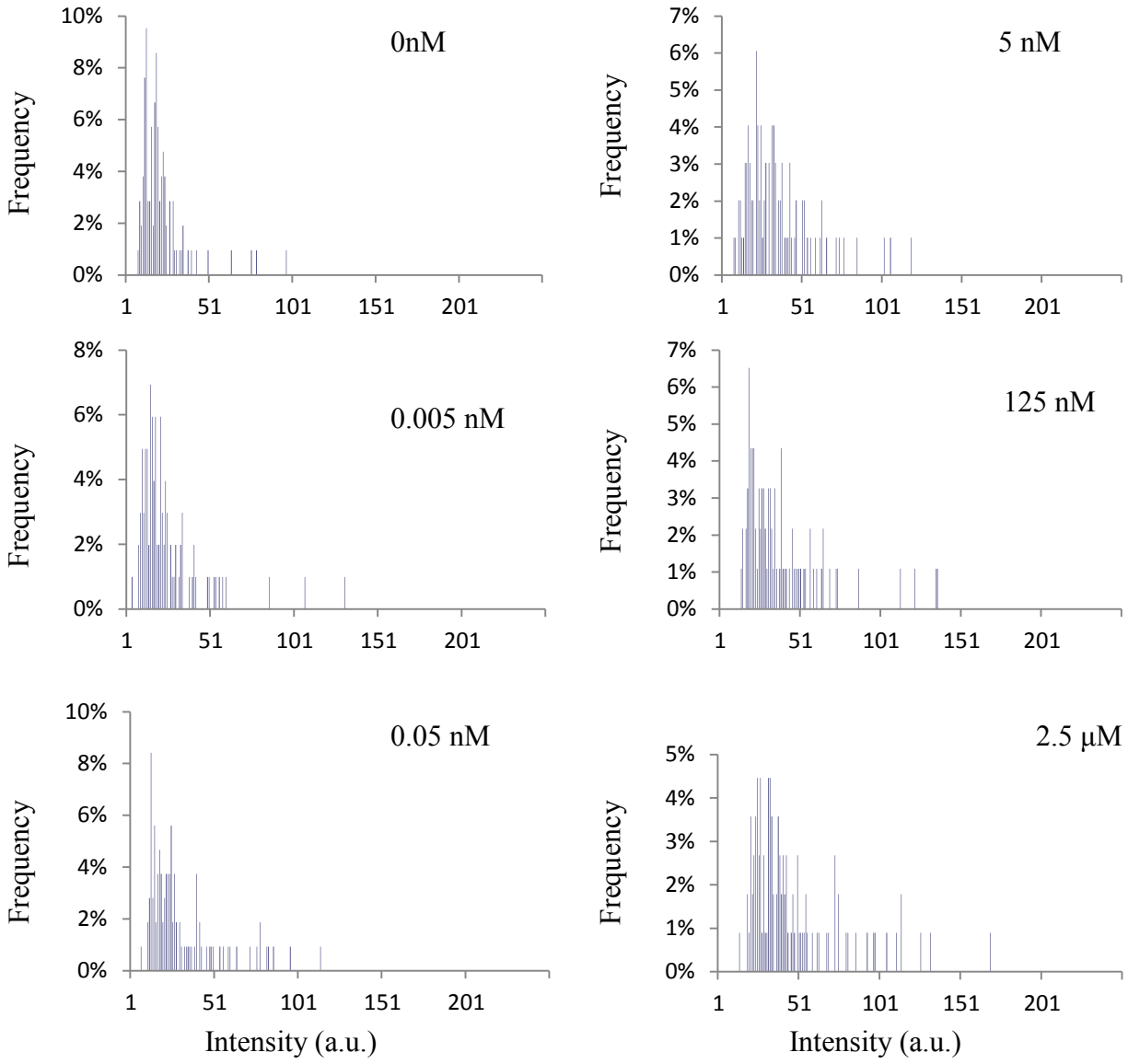

Fig 3.14 Histograms to determine Aβ oligomers detection limit

AuNPs aggregation was caused by adding different concentration of oligomers ranging from 0 to 2.5 µM (number of spots > 200). A11-AuNP colloid without addition of Aβ oligomer was used as background.

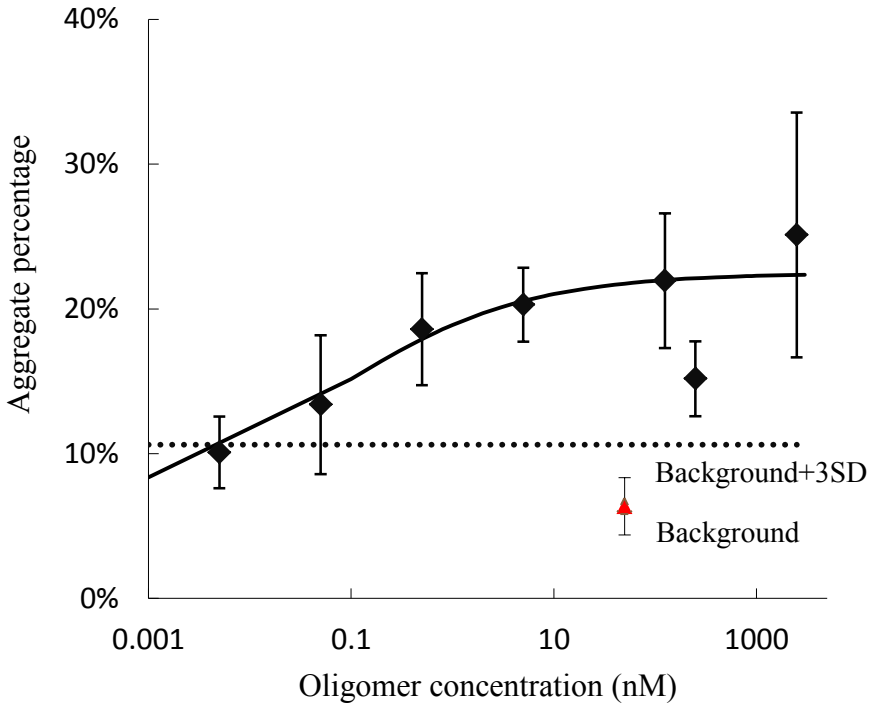

Fig 3.15 Ratio of aggregated A11-AuNP conjugates at various fibrils concentrations.

The A11-AuNP colloid without addition of Aβ protein was used as background (triangle). The error bars represent standard deviations of three different histograms. The background + 3SD was used for calculation of the LOD

Chapter 4 Magnetic nanoparticles for selective amyloid aggregates adsorption and separation

4.1 SUMMARY

As stated in the previous chapter, Aβ toxicity is closely correlated with aggregation into oligomer as well as fibrils, so that both oligomeric and fibrillar Aβ aggregates are targets for therapy design in AD research. Interaction between nano-materials and Aβ protein has attracted increasing attentions, and much work is being done to investigate the effect of NPs on the Aβ fibrillation process. However, not much attention has been paid to the use of NPs in distinguishing and separating selectively the aggregates from monomers.

For this purpose ferromagnetic NPs, MC-NP was employed to separate Aβ aggregates selectively from monomers in solution. The capture of Aβ aggregates was proved to be fast and efficient, which implies the potential of MC-NP in the application of disease diagnosis like AD (Fig 4.1).

4.2 BACKGROUND AND INTRODUCTION

4.2.1 Interaction of new particles with proteins.

Due to the presence of a high proportion of atoms at the surface, NPs have distinct properties compared with the bulk form of the same material; specifically, the surface properties at nano-scale, are dominant over the bulk properties (Mahmoudi et al., 2013). Those properties are quickly revolutionizing many industrial areas; one of the important enhancements of nano-science is in the medical aren, leading to the emergence of the field of “nano medicine” (Mahmoudi, Sant, Wang, Laurent, & Sen, 2011). One potential

application of NPs in the treatment/diagnosis of brain diseases is to harness their effects on protein fibrillation for therapeutic advantage.

It has been found that NPs have the capability to interfere with the fibrillation processes by either promoting or preventing protein aggregation, which may depend on the peptide property for structural transition (Wagner et al., 2010). Linse and co-authors have described a series of studies to understand the role of fundamental intermolecular interactions in protein folding, protein binding in protein fibrillation. This work highlighted the potential for NPs to promote assembly of proteins into amyloid fibrils in vitro by assisting the nucleation process (Linse et al., 2007). Linse's group also reported that copolymeric NiPAM:BAM nanoparticles of varying hydrophobicity prevent amyloid β protein from fibrillation by affecting mainly the nucleation steps of Aβ fibrillation (Cabaleiro-Lago et al., 2008).

In cells, chaperons are used to stabilize unfolded proteins and hinder aggregation, allowing subsequent folding in a controlled manner. Using the interaction between NPs and protein, biomimetic refolding strategies can be designed from the established mechanism of the molecular chaperone machinery. V. M. Rotello and coworkers explored the possibility of using "chaperone- like" AuNPs for the rescue of misfolded proteins during expression in biotechnology application (Mahmoudi et al., 2011). They bound denatured α-chymotrypsin (ChT) using anionic AuNPs and then released the protein by the addition of cationic surfactants as a releasing agent (Fischer, Verma, Goodman, Simard, & Rotello, 2003). K. Akiyoshi and coworkers synthesized a super molecular Cholesterol enzymatically synthesized glycogen-cyclodextrin (CHESG-CD) that showed high chaperone-like activity for thermal stabilization of enzymes and pointed out that the nanogels have great potential to act as an artificial chaperone for protein engineering (Takahashi, Sawada, & Akiyoshi, 2010).

The premier aim of our study was to look for proper nanoparticle as base for artificial chaperone development. Advantages of using NP for the artificial chaperone development include (1) various materials available. (2) Easy dispersion in biological buffer solutions (PBS, Tris, HEPES...), and (3) specific properties of NPs can be explored in studying the protein structure change. For example, magnetic NPs can be collected conveniently by magnet.

The influence of NPs to Aβ fibrillation was roughly studied by incubating various NPs (Table 4.1) with Aβ monomer. ThT signal was used to determine the amount of fibrils in the sample. As shown in Fig 4.2, fibrils were formed without incubation with NP, and with incubation in the presence of most of NPs. However, clear deduction of ThT fluorescence signal was seen with the sample incubated with MC-NP. This result attracted my attention to MC-NP in preventing Aβ fibrillation process.

TEM image (Fig. 4.3) was taken to study the interaction between MC-NP and Aβ protein. TEM images showed even in the presence of the NP, Aβ still formed into stick-like fibrils. And the MC-NPs contact with fibril branches. This gave us a hint that the reason why fibrils amount decreased might be due to the capture of fibrils onto MC-NP, instead of preventing the fibrillation process.

The pre-study gave us the hypothesis that instead of preventing the Aβ fibrillation, MC-NPs interact with and capture the fibrils in solution. To confirm and further investigate this hypothesis, the capacity experiment and adsorption kinetics experiments were designed to characterize the capture of Aβ aggregates by MC-NPs and to explore the usage of MC-NPs in the study of Aβ proteins.

4.2.2 Conventional protein separation methods

Proteins can be separated selectively according to their molecular weight, charge, solubility or specific affinities. Accordingly, various conventional methods have been developed including ultracentrifugation, dialysis, gel filtration, as well as SDS PAGE, and so on (Fig 4.4).

Electrophoresis in free solution or in macroporous gels such as 1-2% agarose separates proteins mainly according to their net electric charge, and electrophoresis in gels such as polyacrylamide separates mainly according to the molecular size of the proteins. Separation by chromatography depends on the differential partition of proteins between a stationary phase and a mobile phase. Column chromatography has proved to be an extremely efficient technique for the separation of proteins in biological extracts (Janson, 2012).

New methods for the separation of proteins should combine high selectivity and a high loading capacity (Tennikova, Bleha, Švec, Almazova, & Belenkii, 1991).

4.2.3 Bio-application of magnetic nanoparticles

Because specific nanoparticles combine the properties of molecules and solids, magnetic nanoparticles have attracted tremendous interest (Fig 4.5) (Lu et al., 2007a; A. H. Lu, E. L. Salabas, & F. Schüth, 2007b; Son, Reichel, He, Schuchman, & Lee, 2005). The protective shell of magnetic NPs can be used for further functionalization with specific components, such as catalytically active species, various drugs, specific binding sites, or other functional groups. The easy separation and controlled placement of these functionalized magnetic NPs by means of an external magnetic field enables their application as catalyst supports, in immobilized enzyme processes, and the construction

of magnetically controllable bio-electrocatalytic systems (Dyal et al., 2003; Hirsch, Katz, & Willner, 2000; Katz & Willner, 2005; Lu et al., 2007a).

4.2.4 Polymer coating of MC-NP using surface initiated atom transfer radical polymerization

While a number of suitable methods have been developed for the synthesis of magnetic nanoparticles of various different compositions, successful application of such magnetic nanoparticles in the areas like biotechnology/biomedicine is highly dependent on the stability of the particles under a range of different conditions (Lu et al., 2007a). And magnetic nanoparticle dispersions are traditionally made from superparamagnetic materials since the absence of magnetic particle-particle attraction under normal conditions (no external field) easily allows preparation of stable dispersion. Zeltner and coworkers demonstrated how the direct, covalent attachment of highly charged polymers can circumvent stabilizer detachment and loss, and permits preparation of stable dispersions of ferromagnetic particles (Fig 4.6) (Zeltner et al., 2012).

The MC-NPs have a cobalt core, in which an enhancement of the magnetic moment with decreasing size was reported (Respaud et al., 1998). Pure metals, such as Fe, Co and Ni and their metal alloys, are very sensitive to air (Lu et al., 2007a). Thus the cobalt surface was coated with a thin lay of carbon to protect the NP so that the oxygen cannot reach the surface of the magnetic particles. Compared to polymer or silica protective coatings, carbon-based coating has many advantages, such as much higher chemical and thermal stability as well as biocompatibility. The cationic polymer polyMAPTAC was chosen for its ionic nature and covalently attached to the graphene-like surface via surface initiated atom transfer radical polymerization (SI-ATRP) (Fig

4.7) (Grass, Athanassiou, & Stark, 2007; Rotzetter, Schumacher, Zako, Stark, & Maeda, 2013; Schaetz et al., 2011; Zeltner et al., 2012).

4.3 MATERIALS AND METHODS

4.3.1 Materials

$A\beta_{42}$ peptide was purchased from Peptide Institute (Osaka, Japan). RPMI 1640 medium was purchased from Sigma (St. Louis, MO). Mouse monoclonal antibody to beta amyloid (6E10) and antibody for oligomer (4G8) were purchased from Abcam (Cambridge, UK). HRP conjugated with anti-mouse immunoglobulin G (IgG) were from R&D systems (Minneapolis, MN). Enhanced chemiluminescence (ECL) was purchased from GE Healthcare. MC-NP was prepared as described *via* surface initiated atom transfer radical polymerization (Zeltner et al., 2012).

4.3.2 Preparation of Aβ monomer, oligomer and fibrils

The seed-free Aβ solutions were prepared as described previously (Sörgjerd et al., 2013; Yamamoto et al., 2007). Briefly, the Aβ peptide (1.25 mg/mL) in a 0.1% ammonia solution was ultra-centrifuged at 100,000 rpm for 3 h at 4°C to obtain a seed-free Aβ solution which was referred to as Aβ monomers in this study. Then the supernatant was collected and stored as aliquots at -80°C. For Aβ fibril formation, Aβ monomers stock (180 μM) was thawed, diluted with PBS to 25 μM, and incubated at 37°C for 48 h. After incubation, samples were diluted to appropriate concentrations for the following experiments. Aβ oligomers were prepared as previously described with minor modifications (Kayed et al., 2007). In brief, Aβ stock solution (2 mM) were prepared by dissolving the lyophilized peptide in 100 mM NaOH followed by water bath sonication

for 30 s. The oligomerization reaction was initiated by diluting the stock solution in PBS (45 μM final Aβ concentration) and incubated at room temperature for up to 2 days. Oligomer formation was confirmed by Native-PAGE/western blot.

4.3.3 Adsorption and separation of Aβ samples by MC-NP

MC-NP was dispersed in PBS and briefly ultrasonicated (Hielscher Ultrasound Technology, UP50H Ultrasonic Processor, Germany) for 1 min before use. MC-NP (50 μg/mL) was incubated with 12.5 μM of Aβ samples (monomer, fibrils and oligomer) for 1 h at room temperature, and collected by a magnet (a strong $Nd_2Fe_{14}B$ magnet (51 × 51 × 25 mm^3, B ≈ 0.5T). And the supernatant was transferred into a new sample tube for analysis. Adsorption and separation of Aβ samples was estimated by the amount of these samples in the supernatant by dot blot analysis for monomer and fibrils, and by Native-PAGE/western blot for oligomers, respectively, as described below.

To estimate adsorption capacity of MC-NP to Aβ samples, 12.5 μM of Aβ samples were incubated with MC-NP at various concentrations (1, 5, 10, 20, 30, 50 and 75 μg/mL) for 1 h at room temperature. The Aβ adsorption capacity (Q) was calculated based on the minimum amount of MC-NP needed to collect all (>95%) the Aβ in PBS solution using the following equation:

$$Q = Ci\ V/W \qquad (1)$$

where Ci (μM) is the initial concentration of Aβ, V(L) is the volume of the Aβ solution and W (g) is the dry weight of the nanoparticle adsorbent. The Aβ sample solution without nanoparticles was used as 100% negative control.

For adsorption kinetics study, MC-NP (50 μg/mL) was incubated with 12.5 μM of Aβ samples. The suspensions were swirled gently at room temperature for different times and the MC-NPs were removed using an external magnet bar.

The Aβadsorption efficiency (E) was calculated based on the difference in Aβ concentration in PBS solution before and after adsorption using the following equation:

$$E = (Ci - Ce)/Ci \times 100\% \qquad (2)$$

where Ci (μM) and Ce (μM) are the initial and equilibrium concentration of Aβ, respectively. The Aβ solution without mixing with nanoparticles was used as 100% negative control.

4.3.4 Dot blot assay for quantification of monomers and fibrils in solution

The dot blot assay was performed as previously described (Sörgjerd et al., 2013). After preparation of Aβ samples (monomers and fibrils), the samples (6 μl) was spotted onto nitrocellulose membrane. Then blocking with 5% skim milk in TBS containing 0.01% Tween20 (0.01% TBST) for 1 h at room temperature, the membrane was incubated with 6E10 antibody for monomer and fibrils, and 4G8 antibody (1:2000) for oligomer, respectively, followed by secondary HRP-conjugated mouse anti-IgG antibody (1:2000). Proteins were visualized using the ECL plus blotting detection system according to the manufacturer's instructions. Luminescence was detected in a LAS 4000 mini luminescent Image Analyzer (Fujifilm, Tokyo, Japan), with the Image Reader LAS 4000 software. Image J was used for quantification.

4.3.5 Native-PAGE and western blotting assay for oligomer analysis

The Aβ oligomer samples (5 μl) from the supernatant after magnet separation were mixed with 5 μl Native-PAGE sample buffer and then applied to Native-PAGE using a Tris-glycine 10-20% gradient precast gel (Wako, Osaka, Japan). Aβ monomer alone was also subjected as control samples. Following transfer to nitrocellulose membrane, the blot was blocked overnight at 4°C with 5% skim milk in 0.01% TBST. After washing using 0.01% TBST, the membrane was incubated with a mouse monoclonal antibody to Aβ (6E10 or 4G8, 1:2000) for 1h at room temperature. Proteins were visualized as described above.

4.3.6 Transmission electron microscopy (TEM) assay

Aβ samples mixed with MC-NP were dropped on a carbon-coated grid, and the grid was allowed to air-dry. Samarium acetate (2.5%) was used to stain the sample. Samples were observed with an excitation voltage of 80 kV using a JEM- 1230 transmission electron microscope (JEOL, Tokyo, Japan).

4.4 RESULTS AND DISCUSSION

4.4.1 Selective separation of fibrils and oligomers by MC-NP

In this study, we first estimated if MC-NP could capture and separate Aβ samples by dot blot assay. Aβ samples (12.5 μM monomer, fibrils and oligomer) were incubated with MC-NP (50 μg/mL) for 1h. After collecting the NPs by magnet, the supernatant was applied to dot blot assay or Native-PAGE/Western Blot assay. As shown in Fig 4. 8a, no fibril was left in the supernatant, indicating adsorption and separation of Aβ fibrils by

MC-NP. Interestingly, the amount of monomers did not change after mixing with MC-NP, suggesting selective binding of MC-NP to fibrils.

The characterization of Aβ oligomer adsorption was carried out by Native-PAGE followed by Western Blot using 4G8 antibody, because the prepared soluble oligomer was actually a mixture of monomer, oligomer and a small amount of fibrils. As shown in Fig. 4.9, soluble oligomers were clarified by incubation with MC-NP, while the monomer was left in the supernatant. It should be noted that fibrils, which were observed at the well of Native PAGE gel, were also removed, supporting the previous result.

These results indicate that oligomer and fibril can be extracted selectively by MC-NP. The association of Aβ aggregates (fibrils and oligomers) with MC-NP was also confirmed by TEM (Fig 4.8b and Fig 4.9b).

4.4.2 Characterization of Aβ fibril specific NP adsorption—Time course

The effects of the contact time for MC-NP on the adsorption of monomer and fibril was estimated (Fig 4.10). A rapid process of fibril by the NP was observed, which reached approximately 85% adsorption within 10 min and 100% in 60 min. In contrast, only less than 25% adsorption of monomer was observed at 60 min. These results suggest that MC-NP required relatively short time to achieve equilibrium with high adsorption efficiency, probably due to high surface area of MC-NP.

4.4.3 Characterization of Aβ fibril specific NP adsorption—dosage

Adsorption capacity of MC-NP toward Aβ fibrils was estimated by examining the dosage effect of MC-NP (0 to 300 μg/mL) in the adsorption colloid on a fixed amount of Aβ fibrils (12.5 μM) with other operational parameters kept constant. As shown in Fig 4. 11, the amount of fibrils adsorbed increased with increasing MC-NP concentration. The

fibril removal efficiency reached to 95% after adding 30 μg/mL adsorbent. When the MC-NP concentration was higher than 50 μg/mL, no fibrils were left in the supernatant after 1 h incubation, indicating that the weight ratio between maximum adsorbed fibril and MC-NP is bigger than 2:1. It is plausible that the number of available fibril binding sites increased with nanoparticle dosage. In addition, the increase in the adsorbent dose provides a large surface area with an increasing number of adsorption sites, resulting in a decrease in equilibrium concentration for a give initial concentration. In contrast, Aβ monomer showed no significant decrease from adsorption with increasing MC-NP dose; only less than 20% of the Aβ monomer was associated with MC-NP, consistent with our previous results showing that Aβ monomers do not interact significantly with MC-NP.

4.4.4 Characterization of Aβ oligomer specific NP adsorption

Recent studies revealed that Aβ oligomers are considered to cause AD. Thus it is important to remove Aβ oligomers. To further study adsorption MC-NP to Aβ oligomers, MC-NP (0 to 300 μg/mL) was mixed with a fixed amount of Aβ oligomers (12.5 μM), and the supernatant after magnet separation was applied to Native PAGE followed by western blot and probed with 4G8 antibody (Lesné et al., 2006). As shown in Fig 4.12, soluble oligomer species were removed to 20% in 10 min reaction time with a small amount of MC-NP (50 μg/mL). After 1 h incubation, 100% Aβ oligomers were completely removed by small amount of MC-NP (1 μg/mL). Consistent with the previous results, Aβ monomer was not removed. Notably, the bigger oligomers were easier to be clarified by MC-NP than smaller oligomers. This suggests that the higher order structure is preferred MC-NP, suggesting that binding of Aβ oligomers to MC-NP might be related to the size or configuration of Aβ aggregates.

4.5 CONCLUSION

In this chapter, we studied the usage of MC-NP in selective separation of Aβ aggregates (oligomers and fibrils). The adsorption was characterized by dot-blot and Western blot assay. TEM was employed as a direct assay to confirm the adsorption directly. This study implies potential application in diagnosis and treatment of various brain diseases such as Alzheimer's disease.

TABLES AND FIGURES IN CHAPTER 4

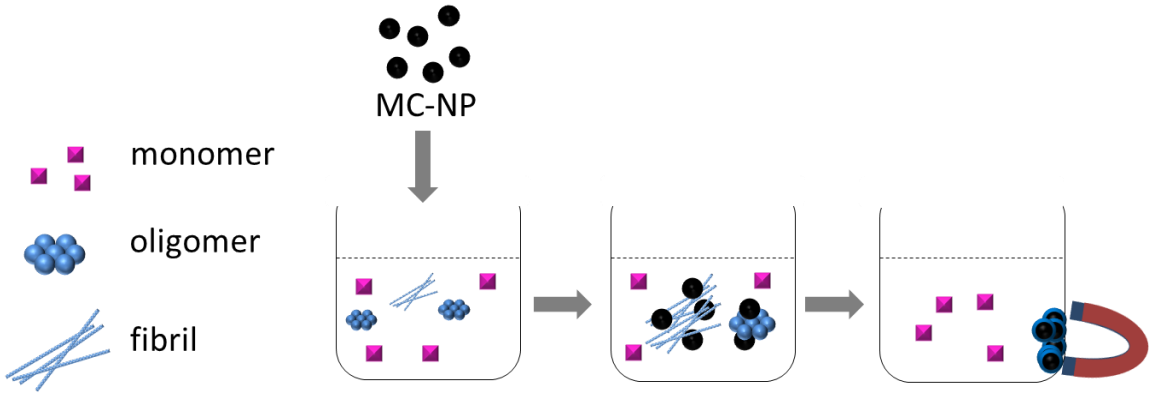

Fig 4.1 Schematic representation of selective separation of Aβ aggregates using MC-NP

Name	Origin	Size (nm)
FeO_x	Ferrofluid EMG700	10
SiO_2 21	LUDOX TMA 420859-1L	21
SiO_2 304	Micro particles GmbH SiO2-R-L130	304
HAP	Hydroxyapatite BAB-HAP-SP	5000
TiO_2	Deguss aeroxide TiO_2	25
MC-NP	C/Co @ polyMAPTAC	50
BionanoG	Bionano glass (SiO_2-CaO-Na_2O-P_2O_5) *	30
CeO_2	Single step flame spray process**	--

Table 4.1 Nanoparticles chosen to screen for the prevention of Aβ fibrillation.

* According to ref. (Hild et al., 2013)

**According to ref. (Grass, Albrecht, et al., 2007)

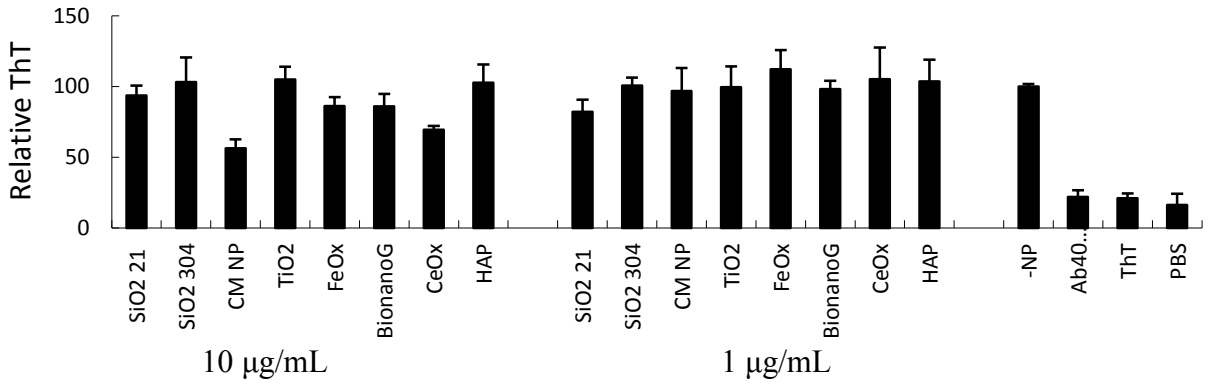

Fig 4.2 Influence of various NPs on Aβ fibrillation

ThT result of Aβ monomers incubated with a series of particles of 10 μg/ mL and 1μg/ mL respectively at 37℃ for 24 h. Monomers incubated 37℃ for 24 h without nanoparticles were used as positive control. $A\beta_{40}$ monomer, ThT only, and PBS buffer were used as negative control. ThT was added into 5 μM Aβ to final concentration of 20 μM. Fluorescence at Ex/Em: 450/485 nm was measured using TECAN M800.

(In collaboration with Functional Materials Laboratory, ETH Zürich)

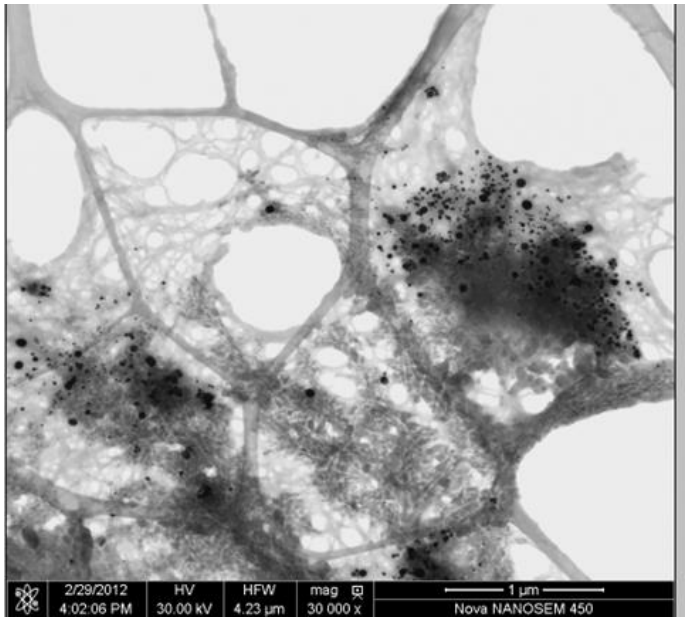

Fig 4.3 STEM images showed the appearance of fibril structures and its interaction with MC-NP.

Black dots are MC nanoparticles

(In courtesy of Dr. Christoph Schumacher at ETH Zürich)

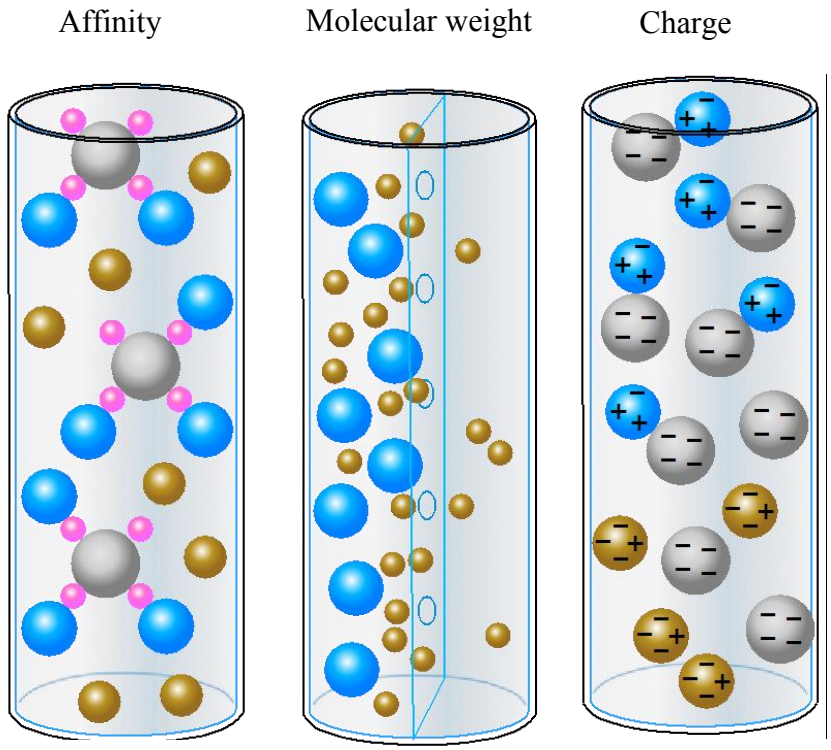

Fig 4.4 Conventional protein separation methods

Blue balls represent the protein wanted, while gold balls represent the inpurities. From left to right, the separation methods are affinity chromatography, dialysis and ion exchange chromatography.

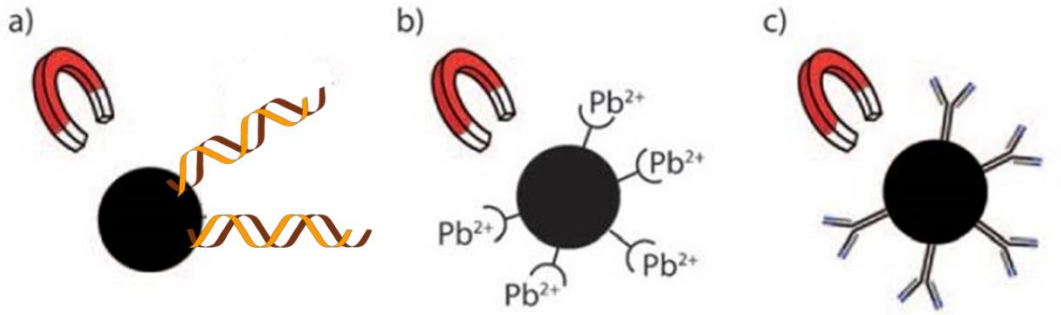

Fig 4.5 Examples of bio-applications of magnetic nanoparticles

(a) Magnetic NP used for controlled localization of gene delivery, (b) magnetic chelating agents (magnetic EDTA (ethylenediaminetetraacetate), a heavy metal ion catching reagent) , and (c) magnetically linked antibodies

Figure is adapted from ref.(Stark, 2011)

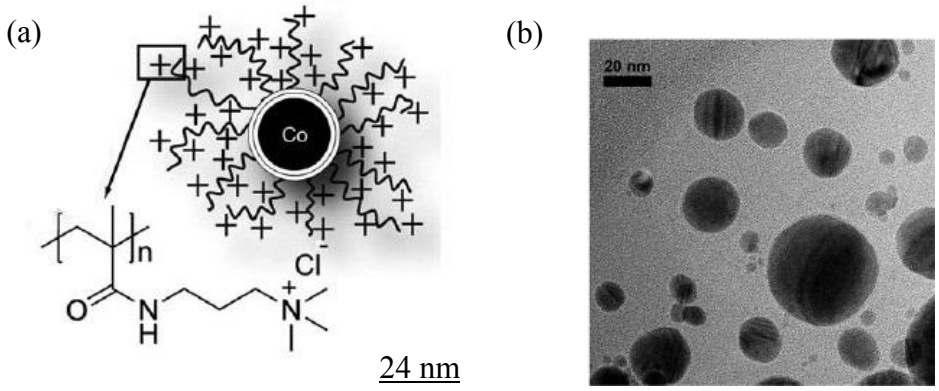

Fig 4.6 Composition of MC-NP and its TEM image

(a) C/Co NP functionalized with polymer PolyMAPTAC (b) TEM image suggested the dispersion of that functionalized NPs.

Figure is taken from ref. (Zeltner et al., 2012)

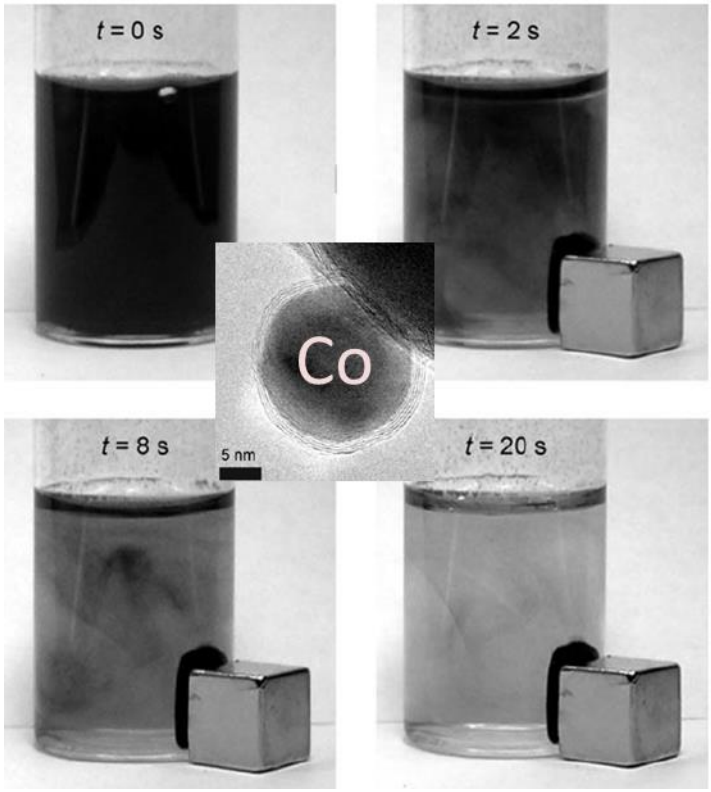

Fig 4.7 Separation of cobalt nanoparticles from a suspension (1g/L) in water by a commercial neodymium magnet

B = 1.4 T. Data published in paper

Figure is taken from ref. (Grass, Athanassiou, et al., 2007)

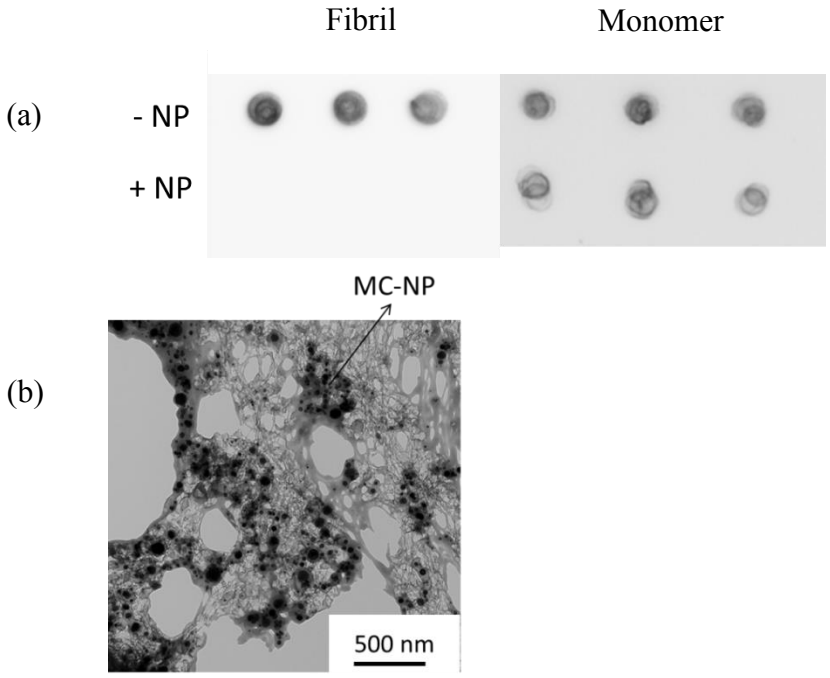

Fig 4.8 Selective adsorption of fibrils to MC-NP

(a)Dot blot assay of selective adsorption of fibrils to MC-NP (b) TEM image confirmed also the interaction between fibrils and NPs

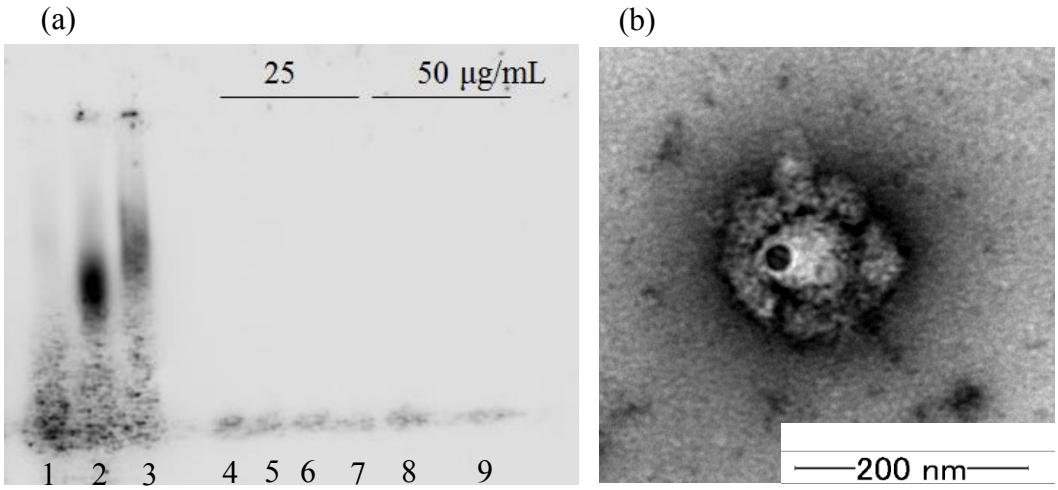

Fig 4.9 Selective adsorption of $A\beta_{42}$ oligomer to MC-NP

(a) Lane 1, $A\beta_{42}$ monomer; lane 2, $A\beta_{42}$ pre-oligomer; lane 3 Aβ 42 oligomer; lane 4-6, supernatant of $A\beta_{42}$ oligomers solution incubated with MC-NP (25 μg/mL); lane 7-9, supernatant of $A\beta_{42}$ oligomers solution incubated with 50 μg/ mL MC-NP. (b) TEM image suggested the interaction between oligomer and MC-NP.

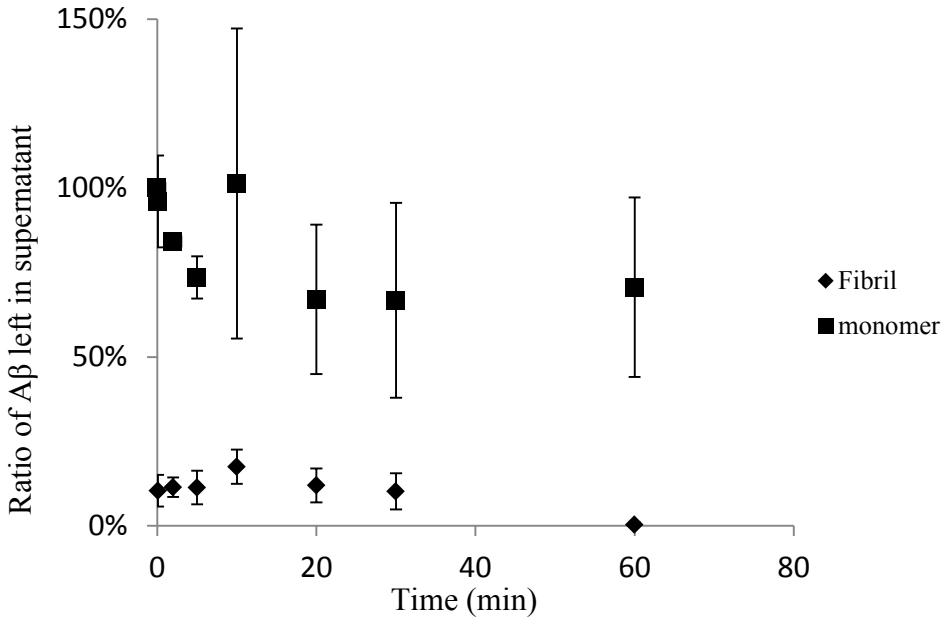

Fig 4.10 Adsorption efficiency of Aβ fibril and monomer s to MC-NP

Aβ fibril and monomer solution were incubated with MC-NP (50 μg/mL) for 1 h at RT. The percentage of Aβ left in the supernatant was quantified by dot-blot assay.

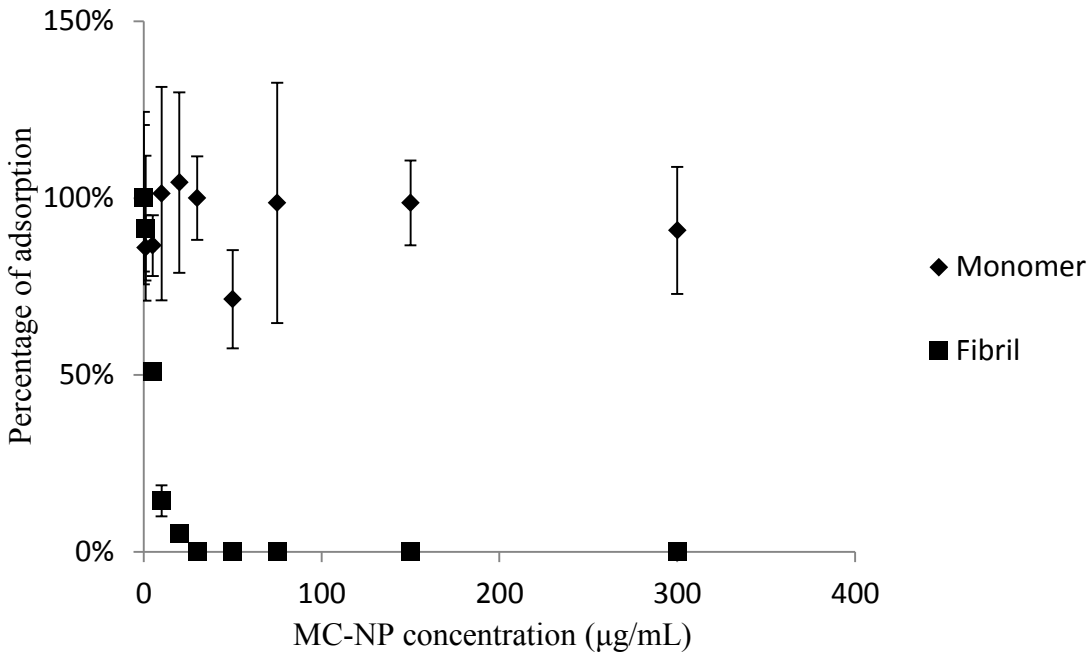

Fig 4.11 Adsorption capacity of Aβ fibrils and monomer to MC-NP

Increasing amount of MC-NPs was added in monomer and fibril solutions (12.5 μM). After incubating at room temperature for 1 h and collecting MC-NPs by magnets, the amount of monomer and fibrils left in the supernatant was quantified by dot blot assay.

(a)

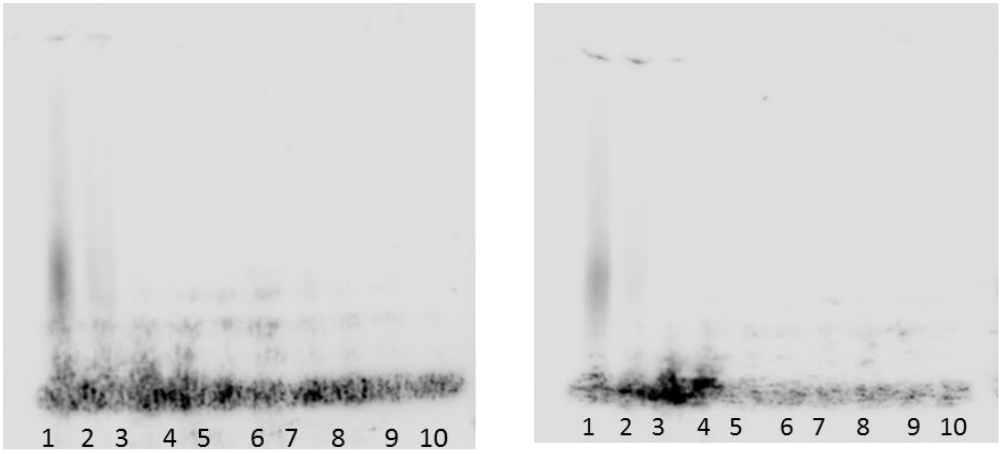

(b)

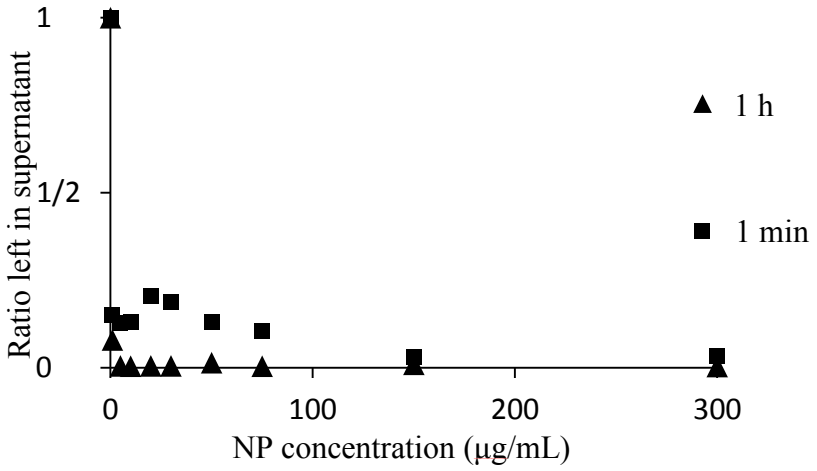

Fig 4.12 Adsorption capacity of oligomers to MC-NP at different time

(a) WB image of oligomers left in supernatant after incubation with increasing amount of MC-NP concentration(0 to 300 μg/mL) for 1 min (left) and for 1 h (right), (b): Amount of oligomers left in the supernatant according to WB image in (a).

Chapter 5 Conclusions and future prospects

In recent years, nano mateirals have emerged as important players in modern medicine, with clinical applications ranging from contrast agents in imaging to carriers for drug and gene delivery into tumors. The use of NPs in sensing and separating biomolecules greatly benefits from the development of NP synthesis and their surface engineering in the last decades. In this study, the potential of NP in biomedical applications have been explored: SNPs in DNA can be detected using AuNPs with high sensitivity. Aβ aggregates that related to AD can be early sensed using antibody immobilized AuNPs. The sensitivity might be further improved by optimizing detection conditions such as temperature, incubation time, and AuNP sizes. Successful development in these studies will aid the growth of biomedical industry as well as improving the quality of life in the population.

The use of magnetic NPs has been developed to in the range of tools to clinicians. In this study, we found that Aβ aggregates can be clarified by magnetic MC-NP from solution. However, from a more fundamental point of view, the mechanism of surface anchoring of Aβ aggregates must be investigated to describe the nature and the force of the surface binding (hydrogen, pseudo-covalent, or ionic bonds). Understanding surface interaction between the NP surface and protein will be very useful to design new surface coating that might further improve the capture efficiency of toxic proteins.

Though there are some instances where NPs enable analyses and therapies that simply cannot be performed otherwise, NPs also bring with unique environmental and societal challenges, particularly in regard to toxicity. Therefore, attention must also be paid to environmental and societal implications.

References

Agarwal, A., Huang, S., O'Donnell, M., Day, K., Day, M., Kotov, N., & Ashkenazi, S. (2007). Targeted gold nanorod contrast agent for prostate cancer detection by photoacoustic imaging. *Journal of Applied Physics, 102*(6), 064701.

Arata, H., Komatsu, H., Hosokawa, K., & Maeda, M. (2012). Rapid and Sensitive MicroRNA Detection with Laminar Flow-Assisted Dendritic Amplification on Power-Free Microfluidic Chip. *PLoS One, 7*(11), e48329.

Arifin, D. R., Long, C. M., Gilad, A. A., Alric, C., Roux, S., Tillement, O., . . . Bulte, J. W. (2011). Trimodal gadolinium-gold microcapsules containing pancreatic islet cells restore normoglycemia in diabetic mice and can be tracked by using US, CT, and positive-contrast MR imaging. *Radiology, 260*(3), 790-798.

Bárcena, C., Sra, A. K., & Gao, J. (2009). Applications of magnetic nanoparticles in biomedicine *Nanoscale magnetic materials and applications* (pp. 591-626): Springer.

Ban, T., Hamada, D., Hasegawa, K., Naiki, H., & Goto, Y. (2003). Direct observation of amyloid fibril growth monitored by thioflavin T fluorescence. *Journal of Biological Chemistry, 278*(19), 16462-16465.

Baniukevic, J., Hakki Boyaci, I., Goktug Bozkurt, A., Tamer, U., Ramanavicius, A., & Ramanaviciene, A. (2013). Magnetic gold nanoparticles in SERS-based sandwich immunoassay for antigen detection by well oriented antibodies. *Biosensors and Bioelectronics, 43*, 281-288.

Berne, B. J., & Pecora, R. (2000). *Dynamic light scattering: with applications to chemistry, biology, and physics*: Courier Dover Publications.

Blennow, K., de Leon, M. J., & Zetterberg, H. Alzheimer's disease. *The Lancet, 368*(9533), 387-403.

Bohren, C. F., & Huffman, D. R. (1983). Absorption and scattering by a sphere. *Absorption and Scattering of Light by Small Particles*, 82-129.

Bohren, C. F., & Huffman, D. R. (2008). *Absorption and scattering of light by small particles*: John Wiley & Sons.

Boisselier, E., & Astruc, D. (2009). Gold nanoparticles in nanomedicine: preparations, imaging, diagnostics, therapies and toxicity. *Chemical Society Reviews, 38*(6), 1759-1782.

Bolder, S. G., Sagis, L. M., Venema, P., & van der Linden, E. (2007). Thioflavin T and birefringence assays to determine the conversion of proteins into fibrils. *Langmuir, 23*(8), 4144-4147.

Cabaleiro-Lago, C., Quinlan-Pluck, F., Lynch, I., Lindman, S., Minogue, A. M., Thulin, E., . . . Linse, S. (2008). Inhibition of amyloid β protein fibrillation by polymeric nanoparticles. *Journal of the American Chemical Society, 130*(46), 15437-15443.

Cai, D., Mataraza, J. M., Qin, Z.-H., Huang, Z., Huang, J., Chiles, T. C., . . . Ren, Z. (2005). Highly efficient molecular delivery into mammalian cells using carbon nanotube spearing. *Nature Methods, 2*(6), 449-454.

Cai, Q.-Y., Kim, S. H., Choi, K. S., Kim, S. Y., Byun, S. J., Kim, K. W., . . . Yoon, K.-H. (2007). Colloidal gold nanoparticles as a blood-pool contrast agent for X-ray computed tomography in mice. *Investigative radiology, 42*(12), 797-806.

Cleary, J. P., Walsh, D. M., Hofmeister, J. J., Shankar, G. M., Kuskowski, M. A., Selkoe, D. J., & Ashe, K. H. (2005). Natural oligomers of the amyloid-β protein specifically disrupt cognitive function. *Nature Neuroscience, 8*(1), 79-84.

Cohen, A. S. (1986). General introduction and a brief history of amyloidosis *Amyloidosis* (pp. 3-19): Springer.

Cormode, D. P., Skajaa, T., van Schooneveld, M. M., Koole, R., Jarzyna, P., Lobatto, M. E., . . . Mulder, W. J. M. (2008). Nanocrystal Core High-Density Lipoproteins: A Multimodality Contrast Agent Platform. *Nano Letters, 8*(11), 3715-3723.

Daniel, M.-C., & Astruc, D. (2004). Gold nanoparticles: assembly, supramolecular chemistry, quantum-size-related properties, and applications toward biology, catalysis, and nanotechnology. *Chemical Reviews, 104*(1), 293-346.

Daniel, M. C., & Astruc, D. (2004). Gold nanoparticles: assembly, supramolecular chemistry, quantum-size-related properties, and applications toward biology, catalysis, and nanotechnology. *Chemical Reviews, 104*(1), 293-346.

Diamandis, P., & Christopoulous, T. (1996). Immunoassay. *San Diego USA; Academic Press*.

Dobson, J. (2006). Gene therapy progress and prospects: magnetic nanoparticle-based gene delivery. *Gene Therapy, 13*(4), 283-287.

Dreaden, E. C., Alkilany, A. M., Huang, X., Murphy, C. J., & El-Sayed, M. A. (2012). The golden age: gold nanoparticles for biomedicine. *Chemical Society Reviews, 41*(7), 2740-2779.

Dyal, A., Loos, K., Noto, M., Chang, S. W., Spagnoli, C., Shafi, K. V., . . . Gross, R. A. (2003). Activity of Candida rugosa lipase immobilized on γ-Fe2O3 magnetic nanoparticles. *Journal of the American Chemical Society, 125*(7), 1684-1685.

El-Omar, E. M., Carrington, M., Chow, W.-H., McColl, K. E., Bream, J. H., Young, H. A., . . . Rothman, N. (2000). Interleukin-1 polymorphisms associated with increased risk of gastric cancer. *Nature, 404*(6776), 398-402.

Elghanian, R., Storhoff, J. J., Mucic, R. C., Letsinger, R. L., & Mirkin, C. A. (1997). Selective colorimetric detection of polynucleotides based on the distance-dependent optical properties of gold nanoparticles. *Science, 277*(5329), 1078-1081.

Fischer, N. O., Verma, A., Goodman, C. M., Simard, J. M., & Rotello, V. M. (2003). Reversible "irreversible" inhibition of chymotrypsin using nanoparticle receptors. *Journal of the American Chemical Society, 125*(44), 13387-13391.

Fujita, M., Katafuchi, Y., Ito, K., Kanayama, N., Takarada, T., & Maeda, M. (2012). Structural study on gold nanoparticle functionalized with DNA and its non-cross-linking aggregation. *Journal of Colloid and Interface Science, 368*(1), 629-635.

Giljohann, D. A., Seferos, D. S., Daniel, W. L., Massich, M. D., Patel, P. C., & Mirkin, C. A. (2010). Gold nanoparticles for biology and medicine. *Angewandte Chemie International Edition, 49*(19), 3280-3294.

Gleich, B., & Weizenecker, J. (2005). Tomographic imaging using the nonlinear response of magnetic particles. *Nature, 435*(7046), 1214-1217.

Grass, R. N., Albrecht, T. F., Krumeich, F., & Stark, W. J. (2007). Large-scale preparation of ceria/bismuth metal-matrix nano-composites with a hardness comparable to steel. *Journal of Materials Chemistry, 17*(15), 1485-1490.

Grass, R. N., Athanassiou, E. K., & Stark, W. J. (2007). Covalently functionalized cobalt nanoparticles as a platform for magnetic separations in organic synthesis. *Angewandte Chemie International Edition, 46*(26), 4909-4912.

Guo, R., Zhang, L., Qian, H., Li, R., Jiang, X., & Liu, B. (2010). Multifunctional nanocarriers for cell imaging, drug delivery, and near-IR photothermal therapy. *Langmuir, 26*(8), 5428-5434.

Haass, C., Hung, A. Y., Schlossmacher, M., Teplow, D. B., & Selkoe, D. J. (1993). beta-Amyloid peptide and a 3-kDa fragment are derived by distinct cellular mechanisms. *Journal of Biological Chemistry, 268*(5), 3021-3024.

Hacia, J. G. (1999). Resequencing and mutational analysis using oligonucleotide microarrays. *Nature Genetics, 21*, 42-47.

Hao, F., Nehl, C. L., Hafner, J. H., & Nordlander, P. (2007). Plasmon resonances of a gold nanostar. *Nano Letters, 7*(3), 729-732.

Hasegawa, K., Yamaguchi, I., Omata, S., Gejyo, F., & Naiki, H. (1999). Interaction between Aβ (1-42) and Aβ (1-40) in Alzheimer's β-amyloid fibril formation in vitro. *Biochemistry, 38*(47), 15514-15521.

Hawe, A., Sutter, M., & Jiskoot, W. (2008). Extrinsic fluorescent dyes as tools for protein characterization. *Pharmaceutical Research, 25*(7), 1487-1499.

Hemker, D. J., & Frank, C. W. (1990). Dynamic light-scattering studies of the fractal aggregation of poly (methacrylic acid) and poly (ethylene glycol). *Macromolecules, 23*(20), 4404-4410.

Herrmann, I. K., Urner, M., Koehler, F. M., Hasler, M., Roth‐Z'Graggen, B., Grass, R. N., . . . Stark, W. J. (2010). Blood purification using functionalized core/shell nanomagnets. *small, 6*(13), 1388-1392.

Hild, N., Tawakoli, P. N., Halter, J. G., Sauer, B., Buchalla, W., Stark, W. J., & Mohn, D. (2013). pH-dependent antibacterial effects on oral microorganisms through pure PLGA implants and composites with nanosized bioactive glass. *Acta Biomaterialia, 9*(11), 9118-9125.

Hirsch, R., Katz, E., & Willner, I. (2000). Magneto-switchable bioelectrocatalysis. *Journal of the American Chemical Society, 122*(48), 12053-12054.

Hu, M., Novo, C., Funston, A., Wang, H., Staleva, H., Zou, S., . . . Hartland, G. V. (2008). Dark-field microscopy studies of single metal nanoparticles: understanding the factors that influence the linewidth of the localized surface plasmon resonance. *Journal of Materials Chemistry, 18*(17), 1949-1960.

Huang, X., El-Sayed, I. H., Qian, W., & El-Sayed, M. A. (2006). Cancer cell imaging and photothermal therapy in the near-infrared region by using gold nanorods. *Journal of the American Chemical Society, 128*(6), 2115-2120.

Hudson, S. A., Ecroyd, H., Kee, T. W., & Carver, J. A. (2009). The thioflavin T fluorescence assay for amyloid fibril detection can be biased by the presence of exogenous compounds. *FEBS Journal, 276*(20), 5960-5972.

Jain, P. K., Lee, K. S., El-Sayed, I. H., & El-Sayed, M. A. (2006). Calculated absorption and scattering properties of gold nanoparticles of different size, shape, and composition: applications in biological imaging and biomedicine. *the Journal of Physical Chemistry B, 110*(14), 7238-7248.

Jans, H., Liu, X., Austin, L., Maes, G., & Huo, Q. (2009). Dynamic Light Scattering as a Powerful Tool for Gold Nanoparticle Bioconjugation and Biomolecular Binding Studies. *Analytical Chemistry, 81*(22), 9425-9432.

Janson, J.-C. (2012). *Protein purification: principles, high resolution methods, and applications* (Vol. 151): John Wiley & Sons.

Jarrett, J. T., Berger, E. P., & Lansbury Jr, P. T. (1993). The carboxy terminus of the. beta. amyloid protein is critical for the seeding of amyloid formation: Implications for the pathogenesis of Alzheimer's disease. *Biochemistry, 32*(18), 4693-4697.

Jones, A. C., Austin, J., Hansen, N., Hoogendoorn, B., Oefner, P. J., Cheadle, J. P., & O'Donovan, M. C. (1999). Optimal temperature selection for mutation detection by denaturing HPLC and comparison to single-stranded conformation polymorphism and heteroduplex analysis. *Clinical Chemistry, 45*(8), 1133-1140.

Kanayama, & Maeda, M. (2014). Unique interfacial phenomena at DNA-based soft-interfaces. *Journal of Japanese Society for Biomaterials, 32*(2), 6.

Kanayama, Takarada, T., Fujita, M., & Maeda, M. (2013). DNA Terminal Breathing Regulated by Metal Ions for Colloidal Logic Gates. *Chemistry-A European Journal, 19*(33), 10794-10798.

Kanayama, Takarada, T., & Maeda, M. (2011). Rapid naked-eye detection of mercury ions based on non-crosslinking aggregation of double-stranded DNA-carrying gold nanoparticles. *Chemical Communications, 47*, 2077-2079.

Kang, J., Lemaire, H.-G., Unterbeck, A., Salbaum, J. M., Masters, C. L., Grzeschik, K.-H., . . . Müller-Hill, B. (1987). The precursor of Alzheimer's disease amyloid A4 protein resembles a cell-surface receptor. *Nature, 325*, 733-736.

Katz, E., & Willner, I. (2005). Switching of directions of bioelectrocatalytic currents and photocurrents at electrode surfaces by using hydrophobic magnetic nanoparticles. *Angewandte Chemie, 117*(30), 4869-4872.

Kayed, R., & Glabe, C. G. (2006). Conformation‐Dependent Anti‐Amyloid Oligomer Antibodies. *Methods in Enzymology, 413*, 326-344.

Kayed, R., Head, E., Sarsoza, F., Saing, T., Cotman, C. W., Necula, M., . . . Thompson, J. L. (2007). Fibril specific, conformation dependent antibodies recognize a generic epitope common to amyloid fibrils and fibrillar oligomers that is absent in prefibrillar oligomers. *Mol Neurodegener, 2*(18), 18.

Kayed, R., Head, E., Thompson, J. L., McIntire, T. M., Milton, S. C., Cotman, C. W., & Glabe, C. G. (2003). Common structure of soluble amyloid oligomers implies common mechanism of pathogenesis. *Science, 300*(5618), 486-489.

Khan, S. J., Pierce, F., Sorensen, C., & Chakrabarti, A. (2009). Self-Assembly of Ligated Gold Nanoparticles: Phenomenological Modeling and Computer Simulations†. *Langmuir, 25*(24), 13861-13868.

Khlebtsov, B., Zharov, V., Melnikov, A., Tuchin, V., & Khlebtsov, N. (2006). Optical amplification of photothermal therapy with gold nanoparticles and nanoclusters. *Nanotechnology, 17*(20), 5167.

Khlebtsov, N., Dykman, L., Krasnov, Y. M., & Mel'nikov, A. (2000). Light absorption by the clusters of colloidal gold and silver particles formed during slow and fast aggregation. *Colloid Journal, 62*(6), 765-779.

Khopade, A. J., & Caruso, F. (2002). Investigation of the factors influencing the formation of dendrimer/polyanion multilayer films. *Langmuir, 18*(20), 7669-7676.

Kim, Y.-P., Daniel, W. L., Xia, Z., Xie, H., Mirkin, C. A., & Rao, J. (2010). Bioluminescent nanosensors for protease detection based upon gold nanoparticle–luciferase conjugates. *Chemical Communications, 46*(1), 76-78.

Kirui, D. K., Krishnan, S., Strickland, A. D., & Batt, C. A. (2011). PAA‐derived gold nanorods for cellular targeting and photothermal therapy. *Macromolecular Bioscience, 11*(6), 779-788.

Koehler, F. M., Rossier, M., Waelle, M., Athanassiou, E. K., Limbach, L. K., Grass, R. N., . . . Stark, W. J. (2009). Magnetic EDTA: coupling heavy metal chelators to metal nanomagnets for rapid removal of cadmium, lead and copper from contaminated water. *Chemical Communications*(32), 4862-4864.

Kojro, E., & Fahrenholz, F. (2005). The non-amyloidogenic pathway: structure and function of α-secretases *Alzheimer's Disease* (pp. 105-127): Springer.

Krebs, M., Bromley, E., & Donald, A. (2005). The binding of thioflavin-T to amyloid fibrils: localisation and implications. *Journal of structural biology, 149*(1), 30-37.

Kwok, P.-Y. (2003). *Single Nucleotide Polymorphisms*: Springer.

Lührs, T., Ritter, C., Adrian, M., Riek-Loher, D., Bohrmann, B., Döbeli, H., . . . Riek, R. (2005). 3D structure of Alzheimer's amyloid-β (1–42) fibrils. *Proceedings of the National Academy of Sciences of the United States of America, 102*(48), 17342-17347.

LaFerla, F. M., Green, K. N., & Oddo, S. (2007). Intracellular amyloid-β in Alzheimer's disease. *Nature Reviews Neuroscience, 8*(7), 499-509.

Lee, J.-S., Ulmann, P. A., Han, M. S., & Mirkin, C. A. (2008). A DNA-gold nanoparticle-based colorimetric competition assay for the detection of cysteine. *Nano Letters, 8*(2), 529-533.

Lee, J. S., Han, M. S., & Mirkin, C. A. (2007). Colorimetric Detection of Mercuric Ion (Hg2+) in Aqueous Media using DNA‐Functionalized Gold Nanoparticles. *Angewandte Chemie, 119*(22), 4171-4174.

Lesné, S., Koh, M. T., Kotilinek, L., Kayed, R., Glabe, C. G., Yang, A., . . . Ashe, K. H. (2006). A specific amyloid-β protein assembly in the brain impairs memory. *Nature, 440*(7082), 352-357.

Levine, H. (1993). Thioflavine T interaction with synthetic Alzheimer's disease β - amyloid peptides: Detection of amyloid aggregation in solution. *Protein Science, 2*(3), 404-410.

Linse, S., Cabaleiro-Lago, C., Xue, W.-F., Lynch, I., Lindman, S., Thulin, E., . . . Dawson, K. A. (2007). Nucleation of protein fibrillation by nanoparticles. *Proceedings of the National Academy of Sciences, 104*(21), 8691-8696.

Liu, D., Wang, Z., & Jiang, X. (2011). Gold nanoparticles for the colorimetric and fluorescent detection of ions and small organic molecules. *Nanoscale, 3*(4), 1421-1433.

Liu, S., & Tang, Z. (2009). Nanoparticle assemblies for biological and chemical sensing. *Journal of Materials Chemistry, 20*(1), 24-35.

Loo, C., Lowery, A., Halas, N., West, J., & Drezek, R. (2005). Immunotargeted nanoshells for integrated cancer imaging and therapy. *Nano Letters, 5*(4), 709-711.

Lu, A. H., Salabas, E. e. L., & Schüth, F. (2007a). Magnetic nanoparticles: synthesis, protection, functionalization, and application. *Angewandte Chemie International Edition, 46*(8), 1222-1244.

Lu, A. H., Salabas, E. L., & Schüth, F. (2007b). Magnetische Nanopartikel: Synthese, Stabilisierung, Funktionalisierung und Anwendung. *Angewandte Chemie, 119*(8), 1242-1266.

Lytton-Jean, A. K., Han, M. S., & Mirkin, C. A. (2007). Microarray detection of duplex and triplex DNA binders with DNA-modified gold nanoparticles. *Analytical Chemistry, 79*(15), 6037-6041.

Möller, H.-J., & Graeber, M. (1998). The case described by Alois Alzheimer in 1911. *European archives of psychiatry and clinical neuroscience, 248*(3), 111-122.

Ma, Z., Tian, L., Wang, T., & Wang, C. (2010). Optical DNA detection based on gold nanorods aggregation. *Analytica Chimica Acta, 673*(2), 179-184.

Mah, C., Fraites, T. J., Zolotukhin, I., Song, S., Flotte, T. R., Dobson, J., . . . Byrne, B. J. (2002). Improved method of recombinant AAV2 delivery for systemic targeted gene therapy. *Molecular Therapy, 6*(1), 106-112.

Mahmoudi, M., Kalhor, H. R., Laurent, S., & Lynch, I. (2013). Protein fibrillation and nanoparticle interactions: opportunities and challenges. *Nanoscale, 5*(7), 2570-2588.

Mahmoudi, M., Sant, S., Wang, B., Laurent, S., & Sen, T. (2011). Superparamagnetic iron oxide nanoparticles (SPIONs): development, surface modification and applications in chemotherapy. *Advanced Drug Delivery Reviews, 63*(1), 24-46.

Masters, C. L., Simms, G., Weinman, N. A., Multhaup, G., McDonald, B. L., & Beyreuther, K. (1985). Amyloid plaque core protein in Alzheimer disease and Down syndrome. *Proceedings of the National Academy of Sciences, 82*(12), 4245-4249.

Mieszawska, A. J., Mulder, W. J., Fayad, Z. A., & Cormode, D. P. (2013). Multifunctional gold nanoparticles for diagnosis and therapy of disease. *Molecular Pharmaceutics, 10*(3), 831-847.

Mirkin, C. A., Letsinger, R. L., Mucic, R. C., & Storhoff, J. J. (1996). A DNA-based method for rationally assembling nanoparticles into macroscopic materials. *Nature, 382*, 607-609.

Mody, V. V., Cox, A., Shah, S., Singh, A., Bevins, W., & Parihar, H. (2014). Magnetic nanoparticle drug delivery systems for targeting tumor. *Applied Nanoscience, 4*(4), 385-392.

Murthy, S. K. (2007). Nanoparticles in modern medicine: state of the art and future challenges. *International journal of nanomedicine, 2*(2), 129.

Nam, S. Y., Ricles, L. M., Suggs, L. J., & Emelianov, S. Y. (2012). In vivo ultrasound and photoacoustic monitoring of mesenchymal stem cells labeled with gold nanotracers. *PLoS One, 7*(5), e37267.

Nehl, C. L., Grady, N. K., Goodrich, G. P., Tam, F., Halas, N. J., & Hafner, J. H. (2004). Scattering spectra of single gold nanoshells. *Nano Letters, 4*(12), 2355-2359.

Pankhurst, Q., Thanh, N., Jones, S., & Dobson, J. (2009). Progress in applications of magnetic nanoparticles in biomedicine. *Journal of Physics D: Applied Physics, 42*(22), 224001.

Pankhurst, Q. A., Connolly, J., Jones, S., & Dobson, J. (2003). Applications of magnetic nanoparticles in biomedicine. *Journal of Physics D: Applied Physics, 36*(13), R167.

Park, S. Y., Lee, J. S., Georganopoulou, D., Mirkin, C. A., & Schatz, G. C. (2006). Structures of DNA-linked nanoparticle aggregates. *the Journal of Physical Chemistry B, 110*(25), 12673-12681.

Pastinen, T., Kurg, A., Metspalu, A., Peltonen, L., & Syvänen, A.-C. (1997). Minisequencing: a specific tool for DNA analysis and diagnostics on oligonucleotide arrays. *Genome Research, 7*(6), 606-614.

Pylaev, T., Khanadeev, V., Khlebtsov, B., Dykman, L., Bogatyrev, V., & Khlebtsov, N. G. (2011). Colorimetric and dynamic light scattering detection of DNA sequences by using positively charged gold nanospheres: a comparative study with gold nanorods. *Nanotechnology, 22*(28), 285501.

Ramos, J., Huang, H.-C., & Rege, K. (2013). Delivery of Plasmid DNA to Mammalian Cells Using Polymer–Gold Nanorod Assemblies *Cellular and Subcellular Nanotechnology* (pp. 81-91): Springer.

Reimer, L., & Kohl, H. (2008). *Transmission electron microscopy: physics of image formation* (Vol. 36): Springer.

Respaud, M., Broto, J., Rakoto, H., Fert, A., Thomas, L., Barbara, B., . . . Mosset, A. (1998). Surface effects on the magnetic properties of ultrafine cobalt particles. *Physical Review B, 57*(5), 2925.

Rosi, N. L., & Mirkin, C. A. (2005). Nanostructures in biodiagnostics. *Chemical Reviews, 105*(4), 1547-1562.

Rotzetter, A. C. C., Schumacher, C. M., Zako, T., Stark, W. J., & Maeda, M. (2013). Rapid Surface–Biostructure Interaction Analysis using strong Metal-based Nanomagnets. *Langmuir, 26*(46), 14117-14123.

Sörgjerd, K. M., Zako, T., Sakono, M., Stirling, P. C., Leroux, M. R., Saito, T., . . . Maeda, M. (2013). Human prefoldin inhibits Aβ fibrillation and contributes to formation of non-toxic Aβ aggregates. *Biochemistry, 52*(20), 3532-3542.

Sachidanandam, R., Weissman, D., Schmidt, S. C., Kakol, J. M., Stein, L. D., Marth, G., . . . Willey, D. L. (2001). A map of human genome sequence variation containing 1.42 million single nucleotide polymorphisms. *Nature, 409*(6822), 928-933.

Saha, K., Agasti, S. S., Kim, C., Li, X., & Rotello, V. M. (2012). Gold nanoparticles in chemical and biological sensing. *Chemical Reviews, 112*(5), 2739-2779.

Sakono, & Zako, T. (2010). Amyloid oligomers: formation and toxicity of Aβ oligomers. *FEBS Journal, 277*(6), 1348-1358.

Sakono, Zako, T., & Maeda, M. (2011). Naked-eye detection of amyloid aggregates using gold nanoparticles modified with amyloid beta antibody. *Analytical Sciences, 28*(1), 73-73.

Sakono, M., Zako, T., Drakulic, S., Valpuesta, J. M., Yohda, M., & Maeda, M. (2010). Size-selective recognition of gold nanoparticles by a molecular chaperone. *Chemical Physics Letters, 501*(1), 108-112.

Sapsford, K. E., Algar, W. R., Berti, L., Gemmill, K. B., Casey, B. J., Oh, E., . . . Medintz, I. L. (2013). Functionalizing nanoparticles with biological molecules: developing chemistries that facilitate nanotechnology. *Chemical Reviews, 113*(3), 1904-2074.

Sato, K., Hosokawa, K., & Maeda, M. (2003). Rapid aggregation of gold nanoparticles induced by non-cross-linking DNA hybridization. *Journal of the American Chemical Society, 125*(27), 8102-8103.

Sato, K., Hosokawa, K., & Maeda, M. (2005). Non-cross-linking gold nanoparticle aggregation as a detection method for single-base substitutions. *Nucleic Acids Research, 33*(1), e4-e4.

Sato, K., Onoguchi, M., Sato, Y., Hosokawa, K., & Maeda, M. (2006). Non-cross-linking gold nanoparticle aggregation for sensitive detection of single-nucleotide polymorphisms: optimization of the particle diameter. *Analytical Biochemistry, 350*(1), 162-164.

Schaetz, A., Zeltner, M., Michl, T. D., Rossier, M., Fuhrer, R., & Stark, W. J. (2011). Magnetic silyl scaffold enables efficient recycling of protecting groups. *Chemistry-A European Journal, 17*(38), 10566-10573.

Schena, M., Shalon, D., Davis, R. W., & Brown, P. O. (1995). Quantitative monitoring of gene expression patterns with a complementary DNA microarray. *Science, 270*(5235), 467-470.

Schneider, G., & Decher, G. (2004). From functional core/shell nanoparticles prepared via layer-by-layer deposition to empty nanospheres. *Nano Letters, 4*(10), 1833-1839.

Schoeler, B., Poptoshev, E., & Caruso, F. (2003). Growth of multilayer films of fixed and variable charge density polyelectrolytes: effect of mutual charge and secondary interactions. *Macromolecules, 36*(14), 5258-5264.

Sipe, J. D., & Cohen, A. S. (2000). Review: history of the amyloid fibril. *Journal of structural biology, 130*(2), 88-98.

Son, S. J., Reichel, J., He, B., Schuchman, M., & Lee, S. B. (2005). Magnetic nanotubes for magnetic-field-assisted bioseparation, biointeraction, and drug delivery. *Journal of the American Chemical Society, 127*(20), 7316-7317.

Spiegelman, J. I., Mindrinos, M. N., & Oefner, P. J. (2000). High-accuracy DNA sequence variation screening by DHPLC. *BioTechniques, 29*(5), 1084-1093.

Stark, W. J. (2011). Nanoparticles in biological systems. *Angewandte Chemie International Edition, 50*(6), 1242-1258.

Storhoff, J. J., Lazarides, A. A., Mucic, R. C., Mirkin, C. A., Letsinger, R. L., & Schatz, G. C. (2000). What controls the optical properties of DNA-linked gold nanoparticle assemblies? *Journal of the American Chemical Society, 122*(19), 4640-4650.

Storm, G., Belliot, S. O., Daemen, T., & Lasic, D. D. (1995). Surface modification of nanoparticles to oppose uptake by the mononuclear phagocyte system. *Advanced Drug Delivery Reviews, 17*(1), 31-48.

Sunde, M., & Blake, C. C. (1998). From the globular to the fibrous state: protein structure and structural conversion in amyloid formation. *Quarterly Reviews of Biophysics, 31*(01), 1-39.

Sunde, M., Serpell, L. C., Bartlam, M., Fraser, P. E., Pepys, M. B., & Blake, C. C. (1997). Common core structure of amyloid fibrils by synchrotron X-ray diffraction. *Journal of Molecular Biology, 273*(3), 729-739.

Syvänen, A.-C., Aalto-Setälä, K., Harju, L., Kontula, K., & Söderlund, H. (1990). A primer-guided nucleotide incorporation assay in the genotyping of apolipoprotein E. *Genomics, 8*(4), 684-692.

Takahashi, H., Sawada, S.-i., & Akiyoshi, K. (2010). Amphiphilic polysaccharide nanoballs: a new building block for nanogel biomedical engineering and artificial chaperones. *ACS nano, 5*(1), 337-345.

Tennikova, T., Bleha, M., Švec, F., Almazova, T., & Belenkii, B. (1991). High-performance membrane chromatography of proteins, a novel method of protein separation. *Journal of Chromatography A, 555*(1), 97-107.

Tyagi, S., & Kramer, F. R. (1996). Molecular beacons: probes that fluoresce upon hybridization. *Nature Biotechnology, 14*(3), 303-308.

Wagner, S. C., Roskamp, M., Pallerla, M., Araghi, R. R., Schlecht, S., & Koksch, B. (2010). Nanoparticle‐Induced Folding and Fibril Formation of Coiled‐Coil‐Based Model Peptides. *small, 6*(12), 1321-1328.

Walsh, D. M., Klyubin, I., Fadeeva, J. V., Cullen, W. K., Anwyl, R., Wolfe, M. S., . . . Selkoe, D. J. (2002). Naturally secreted oligomers of amyloid β protein potently inhibit hippocampal long-term potentiation in vivo. *Nature, 416*(6880), 535-539.

Wang, J., Wang, L., Liu, X., Liang, Z., Song, S., Li, W., . . . Fan, C. (2007). A Gold Nanoparticle‐Based Aptamer Target Binding Readout for ATP Assay. *Advanced Materials, 19*(22), 3943-3946.

Xia, Y., Xiong, Y., Lim, B., & Skrabalak, S. E. (2009). Shape‐Controlled Synthesis of Metal Nanocrystals: Simple Chemistry Meets Complex Physics? *Angewandte Chemie International Edition, 48*(1), 60-103.

Xiao, W., & Oefner, P. J. (2001). Denaturing high‐performance liquid chromatography: A review. *Human Mutation, 17*(6), 439-474.

Yamamoto, N., Matsubara, E., Maeda, S., Minagawa, H., Takashima, A., Maruyama, W., . . . Yanagisawa, K. (2007). A Ganglioside-induced Toxic Soluble Aβ Assembly ITS ENHANCED FORMATION FROM AβBEARING THE ARCTIC MUTATION. *Journal of Biological Chemistry, 282*(4), 2646-2655.

Yankner, B. A., Duffy, L. K., & Kirschner, D. A. (1990). Neurotrophic and neurotoxic effects of amyloid beta protein: reversal by tachykinin neuropeptides. *Science, 250*(4978), 279-282.

Yguerabide, J., & Yguerabide, E. E. (1998). Light-scattering submicroscopic particles as highly fluorescent analogs and their use as tracer labels in clinical and biological applications: I. Theory. *Analytical Biochemistry, 262*(2), 137-156.

Younkin, S. G. (1998). The role of Aβ42 in Alzheimer's disease. *Journal of Physiology-Paris, 92*(3), 289-292.

Zeltner, M., Grass, R. N., Schaetz, A., Bubenhofer, S. B., Luechinger, N. A., & Stark, W. J. (2012). Stable dispersions of ferromagnetic carbon-coated metal nanoparticles: preparation via surface initiated atom transfer radical polymerization. *Journal of Materials Chemistry, 22*(24), 12064-12071.

Zhao, Q., Qian, J., An, Q., & Du, B. (2009). Speedy fabrication of free-standing layer-by-layer multilayer films by using polyelectrolyte complex particles as building blocks. *Journal of Materials Chemistry, 19*(44), 8448-8455.

Zheng, G., Daniel, W. L., & Mirkin, C. A. (2008). A new approach to amplified telomerase detection with polyvalent oligonucleotide nanoparticle conjugates. *Journal of the American Chemical Society, 130*(30), 9644-9645.

Zsigmondy, R. A. (1925). Novel prize lecture. *Nobel Prize in Chemistry*, 132.

Zubay, G., & Doty, P. (1958). Nucleic acid interactions with metal ions and amino acids. *Biochimica et Biophysica Acta, 29*(1), 47-58.

Acknowledgements

I would not have been possible to write this doctoral dissertation without the help and support of the kind people around me, to only some of whom it is possible to give particular mention here.

This dissertation would not have been possible without the help, support and patience of my supervisor, Prof. Mizuo Maeda, not to mention his advice and unsurpassed knowledge on nano-bio interfaces.

I express my sincerest gratitude to Professor Yuji Sasaki, Professor Takashi Funatsu, Professor Kohzo Ito, and Professor Junichi Takeya for reading, evaluating and outstanding comments on this dissertation.

The great guidance, scholarly inputs, constant encouragement, support and friendship of my second supervisor, Dr. Tamotsu Zako, has been invaluable on both an academic and a personal level, for which I am and will always be extremely grateful.

I am most grateful to Prof. Wendelin Stark at ETH Zürich for kindly providing us with their nanoparticles for experiments, especially the MC-NPs which exhibit outstanding properties in capturing toxic Aβ aggregates.

I would like to thank Dr. Masahiro Fujita for teaching me the immobilization of DNA on AuNPs; Dr. Kazuo Hosokawa and Dr. Ryo Ishihara for teaching me the calculation method of LOD for chapter 2 and 3; Dr. Naoki Kanayama for enlightening discussions. I would like to thank all my colleagues and friends in the Maeda Bioengineering Laboratory (RIKEN), past and present, for their assistance and support over the years.

I am fortunately surrounded by so many outstanding researchers. I thank Dr. Karin Sorgjerd for being my friend and teaching me biochemistry experiments like

western blot, *et al*; Tomonori Yoshida and Eitaro Kondo for helping start up cell experiments; Dr. Aline Rotzetter and Dr. Christoph Schumacher (Functional Materials Laboratory, ETH Zürich) for valuable discussions during their stay in our laboratory; Dr. Guoqing Wang for offering me help in performing the TEM experiments, *et al*; Dr. Yoshitsugu Akiyama for detailed advice in TEM experiments; Dr. Ryoko Watanabe-Tamaki (Metamaterials Laboratory, RIKEN) for teaching me the fabrication of AuNP dimers and trimmers; and Ms. Tomoka Kikitsu (Materials Characterization Support Unit, RIKEN) for taking TEM images.

I would like to acknowledge the financial, academic and technical support of International Associate Program (IPA) at RIKEN and its supportive staff, Ms. Shinko Saito. I also thank the Department of Advanced Materials, the University of Tokyo for their support and assistance during my 3 years' stay.

I thank my friends Ms. Chunji Li, Ms. Xiaoyue Zhou, Ms. Chengcheng Huang, Dr. Li Wang and so on in RIKEN, the University of Tokyo, ENS Cachan, and elsewhere in the world for their support and encouragements throughout my study.

Above all, I would like to thank my husband Shuangkai Mei for his personal support and great patience at all times. My parents and parents in law have given me their unequivocal support throughout, as always, for which my mere expression of thanks likewise does not suffice.

Tong BU

2014.08.08

Publications

Chapter 2:

- ✧ Bu, T., *et al*. (2013). "Detection of DNA induced gold nanoparticle aggregation with dark field imaging." *Chemical Communications* 49(68): 7531-7533.

Chapter 3:

- ✧ Bu, T., *et al* "DFM detection of amyloid aggregates using gold nanoparticles modified with anti-amyloid antibody". In preparation

Chapter 4:

- ✧ Bu, T., *et al* "Magnetic PolyMAPTAC nanoparticles for selective amyloid beta aggregates adsorption." In preparation